A Multifaceted Approach to Enhancement of Microwave Breast Images: Exploitation of Magnetic Contrast, Use of a Tissue-Dependent Mapping Technique, and Implementation of Adaptive Algorithmic Stopping Criteria

by

Cameron Kaye

A Thesis submitted to the Faculty of Graduate Studies of

The University of Manitoba

in partial fulfilment of the requirements of the degree of

DOCTOR OF PHILOSOPHY

Department of Electrical and Computer Engineering
University of Manitoba
Winnipeg, Manitoba, Canada

Dedicated to my mother,

Katherine Kaye

(1948 – 2013)

Abstract

Although microwave imaging (MWI) remains a promising future diagnostic tool in breast cancer detection and monitoring, its progress towards widespread clinical application would greatly benefit from an improvement to its relatively low spatial and contrast resolution in delineating healthy and abnormal tissues, especially in comparison to established modalities such as mammography and magnetic resonance imaging (MRI). To this end, research has been undertaken in this work exploring multiple methods of improving the quality of MWI reconstructions.

The tools being employed herein for MWI include an extension of the finite-element contrast source inversion (FEM-CSI) algorithm for both high-order and magnetic materials using a time-harmonic, discontinuous Galerkin formulation of Maxwell's equations (DGM-CSI). Based on an earlier dielectric and magnetic, low-order, integral equation CSI formulation, this code supports unstructured discretization of dielectric, magnetic, and perfectly conducting media, and served as the base algorithm subjected to several alterations encompassing this multifaceted study.

Firstly, DGM-CSI has been employed to produce 2D images of the dielectric properties of synthetic breast models at multiple frequencies using a modified frequency-hopping technique that successively introduces alterations to the intermediate reconstructions of the complex-valued permittivity obtained at each of the individual frequencies. Reconstructions from low-frequency data are used as initial guesses for higher-frequency inversions to stabilize the otherwise non-physical solutions obtained

with high-frequency data alone as per the frequency-hopping convention, but a significant improvement in overall image quality is observed when the imaginary part of the reconstructed low-frequency image is modified to reflect the identical tissue geometry as obtained in the reconstruction of the real part. The imaginary part of the image is intelligently mapped from the real part based on probable tissue types before being passed back to the algorithm as the initial guess between successive frequencies, and held constant during the subsequent reconstructions, which allow only the real part to converge. A comparison of breast imaging results obtained using traditional frequency hopping versus the new technique is provided, and this tissue-dependent mapping tool shows promise for future implementation in 3D imaging as well.

Secondly, this same DGM-CSI algorithm has been modified to employ a "frequency cycling" reconstruction technique, where images obtained from the highest frequency data in a given frequency-hopping sequence are cycled back down to the lowest frequency data as new initial guesses set to restart the entire multi-frequency inversion. This simple cycling technique is shown to produce more accurate images than would be produced through the same number of total iterations spent on a single conventional frequency-hopping run, especially when combined with tissue-dependent mapping.

Thirdly, this improved DGM-CSI algorithm, now equipped with both tissue-dependent mapping and frequency cycling techniques, has been further modified to include a set of automated stopping criteria that determine a suitable time to shift imaging frequencies and to globally terminate reconstructions. While previous criteria have employed simple convergence rules or arbitrary fixed numbers of iterations to halt inversions, a new set of stopping conditions is introduced based on a statistical analysis of a window of past iterations of data error using a non-parametric

goodness-of-fit test: the two-sample Kolmogorov-Smirnov (K-S) test. These novel stopping criteria are shown to improve the efficiency of DGM-CSI while yielding images of equivalent or superior quality to assigning a typically overestimated number of iterations per reconstruction.

Finally, a fundamental change to the conventional approach of data collection in microwave breast imaging is explored with the introduction of magnetic contrast enhancement, intended to overcome the problem of low dielectric contrast resolution between healthy fibroglandular and cancerous tissues. The DGM-CSI algorithm is able to produce quantitative 2D and (through a separate implementation) 3D images of both the dielectric permittivity and magnetic permeability of targets, represented herein as synthetic contrast-enhanced breast models and simple experimental targets containing low dielectric and magnetic materials. The numerical models contain breast tumours embedded with accumulations of magnetic nanoparticles (MNPs), with simulated magnetic properties appropriate for physiologically achievable concentrations. Simplified physical targets containing actual samples of MNPs in the form of "ferrofluid" colloidal suspensions at various concentrations are used for experimental data collection. A two-stage imaging methodology has been developed to recover both the relative permittivity and permeability of these dielectric and magnetic targets. A reconstruction of a breast model's permittivity profile is obtained first and used as an inhomogeneous background (a supported feature of DGM-CSI) for a second-stage reconstruction of the magnetic permeability only, which is demonstrated through inversions of 2D and 3D synthetic data.

The signal acquisition tests that experimentally validated this magnetic contrast-enhanced imaging methodology were carried out and demonstrate how data exclusively attributed to changes in magnetic permeability can be collected by physically

isolating the magnetic response of targets using a static polarizing magnetic field (PMF). This was achieved experimentally by integrating an aluminum faceted quasi-resonant chamber designed for 3D MWI of the breast into the bore of a large custom-designed electromagnet capable of sustaining a stable PMF on the order of 0.2 Tesla across the imaging domain. The chamber was equipped with simple wire monopoles, and the low-contrast oil-based targets of differing sizes and ferrofluid concentrations were interrogated using a four-antenna array in different positions, with the PMF applied and withdrawn appropriately to effectively change the magnetic permeability of the ferrofluid within the chamber and create differential scattered field data.

Similar to ferromagnetic resonance (FMR) spectroscopy, in which detection of FMR phenomena is best achieved at probing frequencies coinciding with the structural resonant frequency of a metallic cavity, within the faceted chamber it was found that certain frequencies of interest yield a high level of sensitivity to the weak magnetic signal physically isolated from the MNPs. As such, described in this work, the particular use of an external PMF across a metallic resonant enclosure (as opposed to an open boundary) to modulate the target MNPs' ferromagnetic resonance properties is referred to herein as "ferromagnetic resonance imaging" (FRI). The final component of this thesis outlines the successful efforts in characterizing a particular narrow band of suitable ferromagnetic imaging frequencies within this asymmetric quasi-resonant faceted chamber.

Contributions

The research contributions presented in this Ph.D. thesis consist primarily of two published peer-reviewed journal papers, another peer-reviewed journal paper recently accepted for publication, and two closely-related peer-reviewed conference publications (one paper and one abstract). The introductory chapter and the conclusion consist of newly written or unpublished content. The second appendix is also newly written, but is based on an oral presentation associated with a conference abstract, the results of which were compiled and presented by Kevin Brown, the second author of the abstract. In all of these published works, the first author is the candidate and the last author is the candidate's supervisor. The second author for all but the recently accepted journal paper and the mentioned conference abstract is Ian Jeffrey, the professor who developed and implemented the inversion algorithm used in the 2D and 3D imaging results presented in this work. The second author for the paper currently under review, Colin Gilmore, is the professor who designed and supervised the construction of the custom electromagnet required for ferromagnetic resonance imaging.

Two of the candidate's research papers featured in this manuscript have been published in peer-reviewed journals: IEEE* Transactions on Antennas and Propaga-

*IEEE Copyright Notice: In reference to IEEE copyrighted material which is used with permission in this thesis, the IEEE does not endorse any of University of Manitoba's products or services. Internal or personal use of this material is permitted. If interested in reprinting/republishing IEEE copyrighted material for advertising or promotional purposes or for creating new collective works for resale or redistribution, please go to http://www.ieee.org/publications_standards/publications/rights/rights_link.html to learn how to obtain a License from RightsLink.

tion and the MDPI Journal of Imaging. The third has been recently accepted for publication but currently not yet published by IEEE Transactions on Biomedical Engineering. A list of publications limited to those submitted by the candidate during Ph.D. studies are listed on the next page, including those in which the candidate is not the first author.

Of the listed publications, the following articles have been included directly or their content amalgamated into this thesis in the form of a Chapter or an Appendix: [J1], [J2], [SJ1], [C1] and [C4].

- **Articles Published in Refereed Journals**

[J1] **Cameron Kaye**, Ian Jeffrey and Joe LoVetri, "Improvement of Multi-Frequency Microwave Breast Imaging through Frequency Cycling and Tissue-Dependent Mapping," *IEEE Transactions on Antennas and Propagation*, vol. 67, no. 11, pp. 7087–7096, November 2019.

[J2] **Cameron Kaye**, Ian Jeffrey and Joe LoVetri, "Novel Stopping Criteria for Optimization-Based Microwave Breast Imaging Algorithms," *Journal of Imaging* Special Issue *Microwave Imaging and Electromagnetic Inverse Scattering Problems*, vol. 5, no. 5, May 2019.

- **Articles Submitted to Refereed Journals**

[SJ1] **Cameron Kaye**, Colin Gilmore and Joe LoVetri, "Enhanced Detection of Magnetic Nanoparticles using a Novel Microwave Ferromagnetic Resonance Imaging System," accepted for publication in *IEEE Transactions on Biomedical Engineering*, August 2020.

- **Conference Papers and Abstracts**

[C1] **Cameron Kaye**, Kevin Brown, Mohammad Asefi, Nicholas Geddert, Ian Jeffrey and Joe LoVetri, "Experimental 3D Microwave Imaging of Magnetic Targets using Discontinuous Galerkin Contrast Source Inversion and a Two-Stage Reconstruction Technique," *2nd URSI Atlantic Radio Science Meeting*, Gran Canaria, Spain, May 2018.

[C2] Joe LoVetri, **Cameron Kaye**, Anastasia Baran and Ian Jeffrey, "Data Hopping and Convergence Criteria for Microwave Imaging," *2017 IEEE International Symposium on Antennas and Propagation and USNC-URSI National Radio Science Meeting*, San Diego, California, USA, July 2017.

[C3] **Cameron Kaye**, Ian Jeffrey and Joe LoVetri, "Enhancement of multi-frequency microwave breast images using a tissue-dependent mapping technique with discontinuous Galerkin contrast source inversion," *4th Advanced Electromagnetics Symposium (AES)*, Malaga, Spain, July 2016. (Invited)

[C4] **Cameron Kaye**, Ian Jeffrey and Joe LoVetri, "Two-stage reconstruction of complex dielectric permittivity and magnetic permeability for biomedical microwave imaging employing magnetic contrast agents," *4th Advanced Electromagnetics Symposium (AES)*, Malaga, Spain, July 2016.

[C5] **Cameron Kaye**, Ian Jeffrey and Joe LoVetri, "Magnetic Contrast-Enhanced Microwave Biomedical Imaging using Discontinuous Galerkin Contrast Source Inversion," *IEEE International Symposium on Antennas and Propagation and USNC/URSI National Radio Science Meeting*, Vancouver, Canada, July 2015.

[C6] Majid Ostadrahimi, Anastasia Baran, Mohammad Asefi, **Cameron Kaye**, Kyle Nemez, Joe LoVetri, *et al.*, "On the Development of a Clinical Full-

Vectorial 3D Microwave Breast Imaging System," *IEEE International Symposium on Antennas and Propagation and USNC/URSI National Radio Science Meeting*, Vancouver, Canada, July 2015.

[C7] **Cameron Kaye**, Joe LoVetri, Amer Zakaria, and Anastasia Baran, "A Study of Contrast-Enhanced Functional Microwave Imaging," *IEEE International Symposium on Antennas and Propagation and USNC/URSI National Radio Science Meeting*, Memphis, USA, July 2014.

[C8] **Cameron Kaye**, Joe LoVetri, Amer Zakaria, and Anastasia Baran, "Exploration of Novel Contrast Agents for Functional Imaging Using Microwave Tomography," *IEEE International Symposium on Antennas and Propagation and USNC/URSI National Radio Science Meeting*, Orlando, USA, July 2013.

[C9] Anastasia Baran, **Cameron Kaye**, Amer Zakaria, and Joe LoVetri, "Investigation of Tumour Detection Using Contrast Agents and FEM-CSI in Biomedical Microwave Tomography," *IEEE International Symposium on Antennas and Propagation and USNC/URSI National Radio Science Meeting*, Orlando, USA, July 2013.

[C10] **Cameron Kaye**, Joe LoVetri, Amer Zakaria, and Majid Ostadrahimi, "Feasibility study of Microwave Tomography for In-Vivo Characterization of Tissue as a Diagnostic Technique for Human Disease," *IEEE International Symposium on Antennas and Propagation and USNC/URSI National Radio Science Meeting*, Chicago, USA, July 2012.

Acknowledgments

First and foremost, I would like to thank my advisor and research mentor, Prof. Joe LoVetri, for his long-standing guidance and unwavering support during my extended M.D./Ph.D. studies, without whom the outstanding work being accomplished at the Electromagnetic Imaging Laboratory (EIL) at the University of Manitoba would not be possible. My colleagues and co-authors, Prof. Ian Jeffrey and Prof. Colin Gilmore, have also provided invaluable contributions to this field and insights that have guided the direction of my research. The software developed by Prof. Jeffrey has been particularly vital to my Ph.D. studies, and it features heavily in all the 2D and 3D microwave imaging results presented in this thesis. I would also like to thank my friends and current or past members of the EIL, including but not limited to Mohammad Asefi, Stasi Baran, and Pedram Mojabi. Special thanks to Kevin Brown, as well, for allowing the use of figures and diagrams based on his work, presented in the second appendix of this thesis.

I would like to express my appreciation for the time taken to review and critique my submitted work by my examining committee members: Prof. Doug Thomson, Prof. Colin Gilmore and Prof. Stephen Pistorius from the University of Manitoba, and my External Examiner, Prof. Lorenzo Crocco, with the National Research Council of Italy's Institute for the Electromagnetic Sensing of the Environment (CNR-IREA) in Naples, Italy. I would like to acknowledge the generous financial support granted by

the Natural Science and Research Council of Canada (NSERC) through the Vanier Canada Graduate Scholarship (VCGS) program.

I would also like to acknowledge my family, specifically my father John Kaye, himself a Ph.D. engineer, who has been a source of valuable experience and a calming influence for me during my continuing studies. Thanks go out to my sister Liz, as well, whose career has taken her back and forth across the globe for over a decade, for her ongoing kindness and emotional support, both from overseas and here at home. Lastly, my mother Kathie, who made the University of Manitoba seem like a second home to me during her decades of employment in Admissions, unfortunately left us too soon to see me reach the end of my long academic road, but I am forever grateful for the time that she was here to offer love, encouragement and inspiration for part of the journey.

Table of Contents

List of Tables

List of Figures

1

Introduction

1.1 Current State of Microwave Imaging

Imaging of biological tissues at microwave frequencies (typically encompassing the 500 MHz to 8 GHz range) has been explored for many years, with only intermittent progress being made in the late 20th century until the advent of more powerful computing systems spurred renewed interest in the field over the past twenty years. Since the initial pioneering microwave imaging experiments by Larsen and Jacobi at the Walter Reed Army Institute of Research were published over forty years ago [5], great strides have been made in the development of algorithms capable of quickly and efficiently solving the underlying inverse problem, and in the design of hardware used to acquire and extract the necessary experimental scattered field data. Manipulation of this electromagnetic scattering information through iterative optimization algorithms is the means by which an image of the bulk-electrical parameters within the target region is formed. These parameters are the relative permittivity (dielectric constant) and the conductivity of the object, often represented by the complex-valued permittivity variable $\hat{\varepsilon}_r$, and it is these frequency-dependent properties that allow qualitative and quantitative differentiation of biological tissue types, including potential malignancies. Conventionally it has been assumed that the bulk-magnetic

properties of the target (the magnetic permeability) are constant and equivalent to the permeability of free space, represented by a complex-valued relative permeability $\hat{\mu}_r$ equal to 1. A discussion of the inverse problem associated with microwave imaging, addressing issues of non-linearity and ill-posedness, is provided in Section 3.2. The underlying mathematical framework needed to solve the inverse scattering problem, in the context of the modified Contrast Source Inversion algorithm used herein, is introduced in Section 3.3.1.

Microwave imaging is a non-destructive imaging modality which can be used for various applications, including biomedical imaging, industrial non-destructive testing, and remote sensing [6–17]. Breast imaging in the context of cancer detection, however, has been the primary focus and consequentially the most developed application of the technology in the biomedical field. Of all the anatomical regions of the human body and areas of potential diagnostic utility, the characterization of breast tumours has been the easiest target (the proverbial low-hanging fruit) of the microwave imaging field. The breast offers a readily accessible, compact and relatively homogeneous mass of tissue, easily allowing the practical construction of hardware systems that perform microwave measurements of the breast. The breast has also proven easy to model computationally; simple, two-dimensional approximations of breast tissues have served to gauge algorithmic progress in microwave imaging reconstructions for over fifteen years, and more recently, three-dimensional models have featured prominently at the forefront of the field as the capabilities and complexity of imaging algorithms have improved. Moreover, the prevalence and public awareness of breast cancer as a real threat to women's health across the world is well established, and any research into improved methods of screening and diagnosis of the disease is well warranted. It comes as no surprise that microwave imaging, with its use of low-power

non-ionizing radiation, the potential portability and low cost of its implementation, and its lack of uncomfortable procedural breast compression, has been lauded as a safe and practical adjunct to mammography as a breast cancer mass screening tool, or for breast cancer treatment monitoring [18].

However, even after years of research, a number of difficult challenges still remain for the emerging technology, broadly referred to as microwave tomography (MWT), microwave imaging spectroscopy (MIS) or more generally microwave imaging (MWI), to see widespread clinical implementation. Among the most well-known hurdles MWI has yet to overcome is its poor spatial resolution (that is, its ability to distinguish separate structures in close proximity), which remains insufficient at this point in time to be competitive with established anatomical imaging modalities of the breast, including digital x-ray mammography, computed tomography (CT) and magnetic resonance imaging (MRI). MWI's spatial resolution is, in principle, directly related to the excitation frequency of the radiating antennas employed for imaging, but increased problem non-linearity and reduced signal penetration depth in biological systems limit the application of higher operating frequencies. Progress has nonetheless been made in improving resolution in numerical simulations, with studies demonstrating reconstructions of simple targets corresponding to less than a sixth of a wavelength, thus achieving "super-resolution" that exceeds the Rayleigh criteria of half a wavelength [19,20]. However, in the author's opinion, these theoretical advancements have yet to translate into meaningful high-resolution imaging results for more complex targets such as the breast. An argument could also be made that the dynamic range and signal-to-noise ratio of the imaging systems themselves are the true resolution-limiting factors, and that ongoing improvements in the sensitivity of signal acquisition hardware will eventually improve image resolution. Nonetheless, the fact remains that at

its current state of development, MWI has yet to deliver reconstructions of anatomic detail with a minimum resolvable spatial distance finer than about three millimeters and cannot reliably detect isolated breast lesions smaller than five millimeters in diameter, which is unfortunately inadequate to meet the requirements of early detection in current breast cancer screening programs.

Another somewhat discouraging revelation regarding tissue characteristics came about in 2007, with the publication by Mariya Lazebnik *et al.* of a large-scale collaborative study from the University of Wisconsin and University of Calgary examining the ultra-wideband dielectric properties of freshly excised human breast tissues. The study revealed that the dielectric contrast between malignant breast carcinoma and normal fibroconnective/fibroglandular tissue may be intrinsically low (no more than 10%) [21]. Although there has been speculation that *in vivo* measurements of tumour tissue would yield a stronger discrimination between these tissues, the finding nonetheless outlined another potential drawback of MWI: independent of its poor spatial resolution, the modality's contrast resolution (its ability to distinguish between differences in signal intensities corresponding to different tissue types) for breast cancer may be fundamentally limited, as well. As most invasive breast carcinomas arise within previously healthy fibroglandular tissue, it would be of great diagnostic benefit for a strong contrast in permittivity or conductivity to exist between these tissue types. That being said, it is worth noting that even existing x-ray mammographic techniques suffer from similar contrast resolution limitations for cancer detection, potentially missing up to 20 % of underlying breast cancers in women with radiographically dense breasts [22, 23]. Although a contrast of 10% for malignant tissue may seem to present a challenge for detecting such lesions, particularly in such breasts with a large proportion of fibroglandular tissue, it is not insurmount-

able. While contrast thresholds for lesion detection in x-ray-based modalities are not directly comparable with those for MWI, amplitude differences on the order of 10% in radiodensity have proven adequate to detect suspicious subcentimeter masses in mammographic images [24, 25].

1.2 Contrast-enhanced Microwave Imaging

While this may seem to put MWI's contrast discrimination capabilities on par with x-ray-based mammography, when assessed in combination with the aforementioned spatial resolution limit, its potential as a screening tool is perhaps limited to applications in remote areas with poor accessibility to basic healthcare, where strong arguments for its portability and low cost come into play. However, a shift in the research focus and target application for MWI may be necessary in order for the technology to be clinically relevant for modern tertiary care centres. This realization has paved the way for novel research into selective contrast-enhanced MWI, which uses exogenous agents to artificially accentuate the dielectric (and magnetic) differences between these healthy and abnormal tissue types. A number of pioneering studies were carried out in the early 2010s, with publications employing microbubbles [26], single-walled carbon nanotubes [27], and magnetic nanoparticles [28], providing some promising results. As alluded to earlier, although the introduction of such contrast agents, with the necessity of an invasive procedure for systemic distribution, would bring the intended biomedical application of MWI outside of the realm of mass breast screening, there are yet other niches in breast cancer assessment that could be filled by microwave imaging, including neo-adjuvant treatment monitoring and pre-surgical assessment of disease extent [18]. Furthermore, the use of contrast agents would mark a change in emphasis from structural imaging to functional imaging, where spatial

resolution is based on physiologic or metabolic data as opposed to pure anatomy. This would bring microwave imaging into the domain of nuclear medicine, alongside modalities such as positron emission tomography (PET) and single-photon emission computed tomography (SPECT), where not only would MWI be able to compete with existing spatial resolutions (which are on the order of a few millimeters), but could potentially offer a radiation-free alternative to these imaging procedures.

The recent interest into contrast-enhanced microwave imaging has driven researchers to find unique methods of detection and exploitation of potentially contrast-enhancing compounds' properties at microwave frequencies, leading a few groups to revisit a fundamental assumption that had remained largely unchanged since MWI was established: namely, the choice to essentially ignore changes in the magnetic permeability of the target imaging region. The tissues of the human body are inherently non-magnetic and the precise values of the imaging region's bulk-magnetic properties are unnecessary to obtain a solution of the inversion equation that leads to a quantitative dielectric contrast profile; keeping the permeability constant (at the value of free space) was therefore perfectly logical, and removed a variable that would increase the complexity of the inverse problem. However, with the introduction of magnetic contrast agents, such as magnetic nanoparticles (MNPs), the possibility of artificially inducing a magnetic anomaly localized only into a tissue or lesion of interest allows an alternative means of cancer detection through reconstruction of a magnetic contrast from the corresponding scattered field. These magnetic anomalies can be isolated through the application of an external magnetic field to the target region, and imaged using the same underlying algorithmic techniques of traditional MWI, appropriately modified to solve for contrast in permeability (or magnetic susceptibility) [28].

Although a few isolated studies of nanoparticle-based contrast agents have been undertaken by some prominent researchers in the field [29–31], a research group at the University of Naples Federico II in collaboration with the National Research Council of Italy's Institute for the Electromagnetic Sensing of the Environment (CNR-IREA) in Naples, Italy has laid a large part of the theoretical groundwork for MNP contrast-enhanced breast MWI [28, 32, 33]. Through a number of numerical simulations and recent small-scale experiments that exploit the properties of these compounds, they have demonstrated the viability of employing biocompatible MNPs that are already approved for clinical use in MRI, such as superparamagnetic iron oxide (SPIO) particles, for microwave breast imaging applications. Typically synthesized as a water ferrofluid (*i.e.*, a colloidal suspension of single-domain magnetite nanoparticles with a diameter of ten nanometers or less in a water-based solvent), these nanoparticle cores can be designed to specifically bind to cancer cell receptors once their water-dispersible shells have been appropriately functionalized with bioactive materials (enzymes, antibodies, proteins, *etc.*) [34–36]. Delivered through systemic administration, the MNPs would then accumulate in malignant breast lesions and induce a weak magnetic contrast, provided a sufficient volumetric concentration of magnetic material reaches the tumour through available targeting routes [35]. However, this small magnetic signal is subject to a "masking" effect from the typically strong dielectric electromagnetic scattering responses that occur within lossy, highly conductive biological tissues and consequentially can be very difficult to measure. The group in Naples demonstrated a novel technique to isolate this signal through the introduction of a polarizing magnetic field (PMF) on the order of 100 to 200 kA/m (corresponding to about 125-250 mT in free space) applied to the entire imaging region. The ferromagnetic material within the tumour becomes magnetically saturated, essentially "quenching" its mag-

netic susceptibility and removing its contribution to the microwave response. The differential measurement provided by collecting scattering parameters (*e.g.* S_{11} and S_{21}) with the PMF both on and off presents a means of separating the weak magnetic data (relative permeability) from the strong electric response (relative permittivity) at the measurement stage, because the electromagnetic scattering from the permittivity remains the same [28]. This scattering signal from the MNP-laden tumour would be detectable independent of the surrounding non-magnetic healthy fibroglandular tissue and localized, as aforementioned, through a similar inversion process [33].

However, the only other study attempting to tackle contrast-enhanced MWI using synthetic data employed a truncated singular value decomposition (TSVD) scheme that made overly-simplified assumptions of homogeneity for the underlying breast phantom's tissue in order to perform inversions of magnetic polarizability, which became quantitatively inaccurate when noise was added to the data [33]. While this approach represents a good starting point, it may ultimately prove challenging to successfully apply to complex, heterogeneous breast phantoms in an experimental setting, and provides no information about breast anatomical structure or the tissues' complex-valued permittivity, which is and should remain an important component of MWI's potential contribution to diagnostic imaging. Thus, as explained in the next section, and as will be demonstrated throughout this thesis, considerable effort has been devoted primarily to the improvement of the quantitative reconstruction of breast complex-valued permittivity. Since our unique DGM-CSI algorithm has the ability to perform two-stage quantitative reconstructions of both relative dielectric permittivity and magnetic permeability with support for inhomogeneous backgrounds, it will become clear why the tools developed here to create more accurate inversions of the breast's dielectric properties will ultimately prove beneficial to

magnetic contrast-enhanced MWI, as well [37, 38].

1.3 Multifaceted Approach to Microwave Image Enhancement

In this thesis, several approaches to the enhancement of microwave breast images, specifically dealing with methods of improving the aforementioned weaknesses in the spatial and contrast resolution of MWI, are discussed and implemented. In Chapter 2, a previously described Discontinuous Galerkin method formulation of Maxwell's equations (DGM-CSI) deployed within a well-established frequency-hopping framework is modified such that imaging results at intermediate frequencies are subjected to post-processing techniques intended to stabilize the often poorly reconstructed imaginary part of the complex-valued permittivity. Reproduced from a paper published in *IEEE Transactions on Antennas and Propagation*, this chapter outlines the steps undertaken to strategically map the real parts of low-frequency 2D reconstructions of synthetic breast phantoms to their imaginary parts (based on probable breast tissue type) before being fed back into the algorithm as the initial guess for the next frequency in the frequency-hopping sequence [39, 40]. A second novel improvement is introduced in this chapter in the form of "frequency cycling", where images obtained from the highest available frequency data (the conventional stopping point of frequency-hopping techniques) are cycled back down to the lowest frequency data as new initial guesses to restart the sequence once more [40].

As a logical extension to these tissue-dependent mapping and frequency cycling techniques, Chapter 3 introduces a novel set of stopping criteria for the modified DGM-CSI algorithm which determine suitable times to shift imaging frequencies

within the frequency-cycling sequence, and when global termination of the reconstruction cycle would be appropriate. These decisions are automated, based on a statistical analysis of a window of past iterations' data error using a non-parametric goodness-of-fit test: the two-sample Kolmogorov-Smirnov (K-S) test. This chapter is based on the author's journal paper published in the *Journal of Imaging*'s special issue on "Microwave Imaging and Electromagnetic Inverse Scattering Problems", and demonstrates that the efficiency of DGM-CSI can be improved for 2D reconstructions of several different scenarios involving different breast models, boundary conditions, and noise levels, without sacrificing the quality of resultant images [41].

As opposed to these post-processing techniques, which aim to augment the spatial resolution of microwave image reconstruction, the research reported in Chapter 4 seeks to address the apparent limitations in dielectric contrast resolution between healthy fibroglandular and cancerous tissues at the level of data acquisition, through the use of magnetic contrast enhancement. Based on a paper submitted to *IEEE Transactions on Biomedical Engineering*, this chapter introduces substantial progress that has been made developing a fundamentally different approach to acquiring microwave imaging data using magnetic nanoparticles (MNPs) [42]. The results of preliminary signal acquisition tests are shown, using simplified physical targets containing oil-based colloidal suspensions of MNPs ("ferrofluids") placed within an aluminum quasi-resonant imaging chamber, which itself is integrated into a large custom-made electromagnet. This electromagnet provides a static polarizing magnetic field (PMF) across the imaging domain that allows the creation of differential data through its application and withdrawal, which physical isolates the ferromagnetic resonance response of the MNP-laden targets (their magnetic susceptibility) from their stronger dielectric response, detected specifically at sensitive resonant frequency bands within the metallic

imaging enclosure. As this imaging technique operates using similar physical principles to ferromagnetic resonance spectroscopy (FMR), in this chapter it is coined "ferromagnetic resonance imaging" (FRI), though only signal acquisition tests using a four-antenna array of wire monopoles have thus far been accomplished and sufficient data for imaging purposes has not yet been obtained.

While the main chapters of this thesis are presented in a sandwich-style format of the author's published and submitted peer-reviewed journal papers, this document also contains two appendices based on other work accomplished during the author's Ph.D. studies. Appendix A is a reproduction of a conference paper presented at the 2016 *Advanced Electromagnetics Symposium (AES)*, and Appendix B is based on an abstract presented at the 2018 *URSI Atlantic Radio Science Conference* (URSI AT-RASC). The algorithms developed for these papers largely represent the work of the respective co-authors, but they are included because they briefly introduce a two-stage imaging methodology that has been implemented to recover both the relative permittivity and permeability of dielectric and magnetic targets [37, 38]. A reconstruction of a breast model's permittivity profile is obtained first and used as an inhomogeneous background (a supported feature of DGM-CSI) for a second-stage reconstruction of the magnetic permeability only, which is demonstrated through inversions of 2D and 3D synthetic data. This methodology will ultimately be employed for the FRI data obtained through the means outlined in Chapter 4.

2

Article 1*: Improvement of Multi-Frequency Microwave Breast Imaging through Frequency Cycling and Tissue-Dependent Mapping

2.1 Abstract

Two modifications of the Contrast Source Inversion algorithm (CSI) have been employed to improve resulting 2D microwave images of the dielectric properties of synthetic breast models produced using a well-established frequency-hopping technique. First, while reconstructions from low-frequency data are often used as initial guesses for otherwise unstable higher-frequency inversions, an improvement in overall image quality can be observed when the imaginary part of the reconstructed low-frequency image is altered to reflect the identical tissue geometry as its real part when used as an initial guess during subsequent reconstructions. Secondly, in such

*Reprinted with permission from Cameron Kaye, Ian Jeffrey and Joe LoVetri, "Improvement of Multi-Frequency Microwave Breast Imaging through Frequency Cycling and Tissue-Dependent Mapping," *IEEE Transactions on Antennas and Propagation*, vol. 67, no. 11, pp. 7087–7096, November 2019.

frequency-hopping scenarios, rather than terminating reconstructions following inversions of the highest frequency data, "frequency cycling" (*i.e.* returning to the lowest frequency in the sequence) can be used to further improve reconstructions without loss of resolution or anatomical detail.

2.2 Introduction

Although microwave imaging (MWI) remains a promising future diagnostic tool in breast cancer detection and monitoring, its progress towards widespread clinical application would greatly benefit from an improvement to its relatively low spatial resolution, especially in comparison to established modalities such as mammography and magnetic resonance imaging (MRI). The current gold standard for breast cancer screening, x-ray film or digital mammography, does have well-documented drawbacks: it may miss up to 20% of underlying breast cancers and has a high false-positive rate, particularly in women with Category D or "extremely dense" breasts, as classified by the American College of Radiology's Breast Imaging Reporting and Data System (BI-RADS) [22, 23]. While newer technologies such as digital breast tomosynthesis (DBT) have shown promise in overcoming these drawbacks, there are unique features of MWI, such as its low cost, portability, and use of non-ionizing radiation, that provide strong arguments for its utility in niche areas of health care, such as neo-adjuvant chemotherapy monitoring or use in remote or economically-disadvantaged regions [43].

However, if MWI is to be genuinely considered as a viable single-modality breast cancer screening tool, highly reliable detection of small tumours (less than 2.0 cm in diameter), which make up 68% of those detected by screening mammography [44], must be demonstrated. While radar-acquired prior information [45], acoustic prior

information [46], contrast enhancement [47] and further algorithmic sophistication [48] have certainly increased the quality of MWI reconstructions over recent years, the high soft-tissue attenuation of gigahertz-range frequencies, the errors inherent to inversion model mismatch, and the ill-posed nature of the underlying inverse scattering problem itself remain important limiting factors to the measure of distinguishable anatomic detail thus far achieved in published microwave breast images.

One of the more promising attempts to overcome these challenges involves multi-frequency imaging, either using simultaneous inversion or through "frequency hopping" to first converge to solutions based on low-frequency data and feeding these solutions as "initial guesses" into separate, more complex high-frequency problems. Simultaneous multi-frequency inversion suffers drawbacks related to its application to dispersive materials, which can complicate its use in biological imaging, but these issues are not insurmountable [49, 50].

For instance, a promising form of simultaneous multi-frequency inversion employing compressive sensing unmixing algorithms has been developed which does not directly recover the complex permittivity of individual pixels or voxels but instead parameterizes breast targets into mixtures of high water content, low water content, and cancerous tissues (*i.e.* frequency-independent quantities) [51]. This method was demonstrated for hybrid DBT/MWI systems which require ionizing radiation exposure, however, as baseline tissue proportions for the MWI reconstruction process were first segmented directly from DBT images. Frequency hopping remains a simpler solution for single-modality microwave imaging systems, providing a single forward operator for each frequency, and has been used reliably for decades in the MWI field [52, 53].

There have also been more recent novel studies combining both these approaches,

in which a good initial guess is initially pursued by inverting single-frequency data then followed by simultaneous processing of multi-frequency data. Excellent imaging results have been obtained using such "hybrid" techniques, for example, through implementation of the two-step iterative shrinkage/thresholding (TwIST) method with new regularization strategies based on the L_1 norm and the Pareto curve [54], and through wavelet-based regularization [55]. Both of these studies capture the frequency dependence of human tissues' dielectric properties in multifrequency inversions through explicit reconstruction of single-pole Debye models, and have only been implemented as extensions to the distorted Born iterative method (DBIM).

While similar in concept, the technique described herein alternatively explores modifications of the Contrast Source Inversion (CSI) algorithm, and preserves the simplicity of "frequency-hopping" reconstructions of monochromatic data by keeping dispersion models uncoupled from the inversion process, using single-pole Cole-Cole equations only as a method to adjust initial guesses between single-frequency reconstructions, based on simple single-variable prediction of breast tissue categories.

There are two common ways to initialize single-frequency CSI reconstructions: either through a back-propagated initial estimate for the contrast sources, or to use an estimate of the contrast function and an appropriate forward solve to generate the contrast sources. As the number of mathematical unknowns scales up considerably with mesh size for higher-frequency problems in both 2D and 3D scenarios, nonlinear multiple scattering effects become more pronounced, and as aforementioned, initial guesses derived from smaller, less complicated low-frequency solutions serve as much better starting points than back-propagated initial estimates from homogeneous backgrounds. As one would expect, studies have indeed shown that improved initial guesses for iterative algorithms like DBIM lead to improved imaging performance [56].

Similarly, for algorithms such as CSI, a good initial guess is correspondingly often necessary to produce physically meaningful images at higher frequencies. One could logically infer that further improvement to the initial guess through intermediate reconstructions of progressively higher frequency data allows the algorithm to converge closer to the exact physical solution, or true global minimum, and thus confer improved spatial resolution to the final images. This basic principle of improving microwave images through the use of more physically accurate initial guesses served as motivation to develop the reconstruction approach described herein.

In this work, the reconstructions from a frequency-hopping formulation of CSI are enhanced through the use of an image property mapping technique based on dielectric models of human tissue developed from *ex vivo* measurements [1]. Improvement is achieved through modification of the initial guesses between frequencies, a method described in an earlier preliminary study but significantly expanded upon herein [39]. A "frequency cycling" practice is also introduced that returns the reconstruction to lower frequency inversions without sacrificing high-frequency detail. The results are subjected to quantitative analysis using common image error metrics to provide an objective measurement of these improvements.

2.3 Methods

2.3.1 DGM-CSI algorithm

All 2D breast images presented here have been reconstructed with an implementation of CSI that uses a high-order frequency-domain formulation of Maxwell's curl equations, employing the discontinuous Galerkin method (DGM) as a forward solver. In the resulting DGM-CSI algorithm, unknown field and contrast quantities are rep-

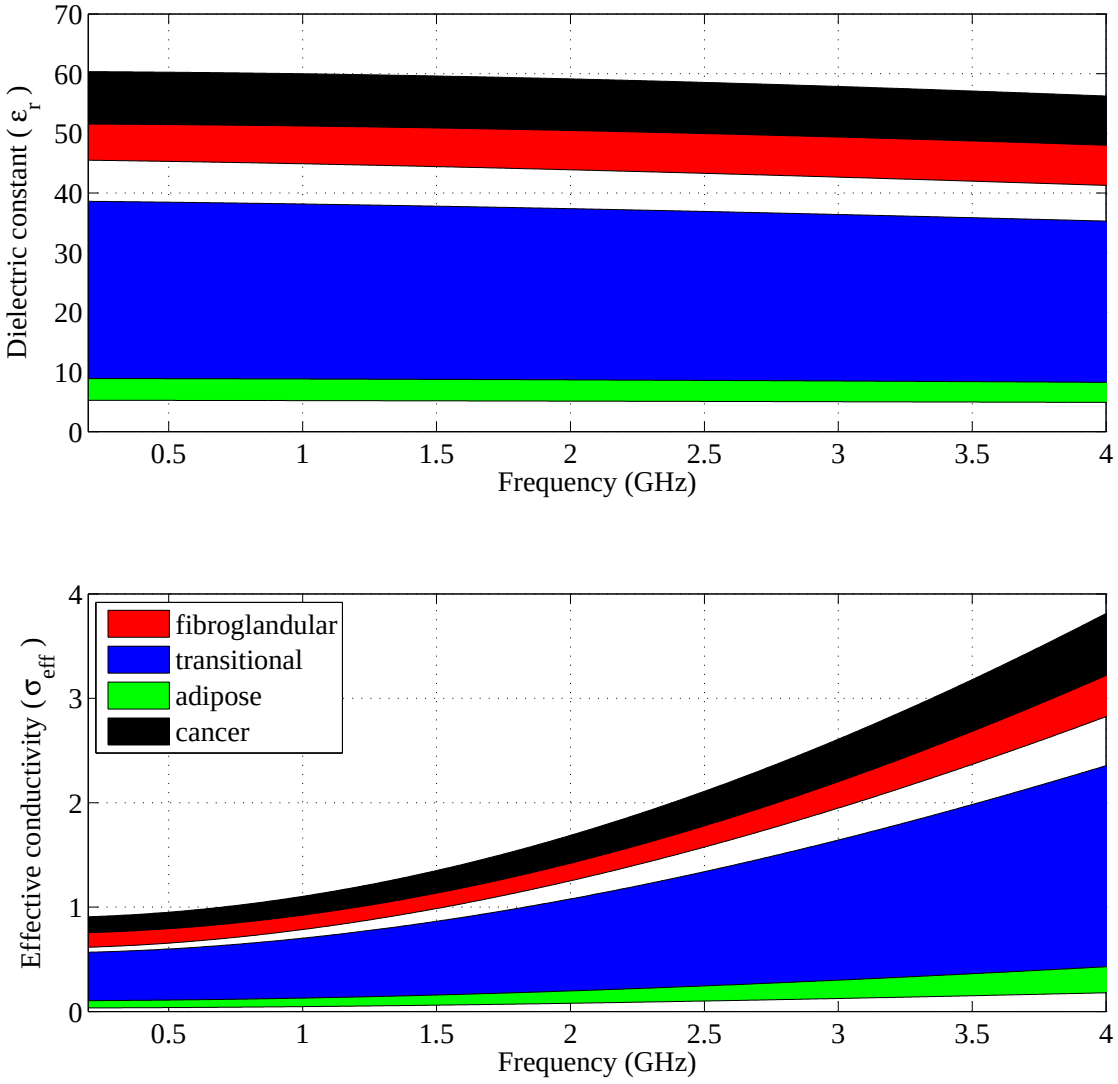

Figure 2.1: Electromagnetic properties of human breast tissues across the frequency range of 1.0 GHz to 4.0 GHz: dielectric constant (ε_r, top) and effective conductivity (σ_{eff}, bottom). Cole-Cole models are based on fitted parameters from measurements of breast cancer surgery samples as outlined in [1].

resented by nodal coefficients in high-order polynomial expansions. While the modifications to the algorithmic imaging framework introduced here are independent of the choice of CSI implementation, further details specific to DGM-CSI can be found in [57–59].

2.3.2 Tissue-dependent mapping of the complex permittivity

The relative permittivity ($\hat{\varepsilon}_r$) of biological tissue is a frequency-dependent complex quantity, and its two components are associated with different properties of a given tissue type. The real part represents the tissue's dielectric constant, whereas the imaginary part is related to its conductivity (or dielectric loss). Although both these quantitative values can be useful in the identification of tissues in MWI images, it has been the authors' general observation in published results that the fidelity of the reconstructed real part of the complex permittivity is superior to that of the imaginary component, a drawback also readily apparent in the high-frequency DGM-CSI images to be shown here.

As a result, imaging studies have often emphasized the quality of the distributions of dielectric constant while glossing over less impressive reconstructions of the imaginary component, or omitting them entirely. The underlying cause behind this apparent disparity in reconstruction quality is thought to be related to the process of balancing real and imaginary contributions to the algorithm's cost functional, and has been discussed at length elsewhere [60]. One technique previously developed to address this balancing issue, balanced multiplicative regularization (MR), has been moderately successful in quantitative ultrasonic imaging [61]. However, in microwave imaging applications employing CSI, this technique has had the unfortunate side effect of "flattening" reconstructions, with a resulting loss of detail [62, 63].

This work does not seek to explain or resolve the mechanism by which this degradation of the imaginary part occurs, but simply exploit two observations of breast phantoms and their tissue properties that are used in MWI studies to aid the imaging algorithm's inversion of the imaginary component during frequency-hopping reconstructions. The first observation is that the *geometry* of tissues' permittivity profiles should be structurally similar in the real and imaginary part. That is, the shape, distribution and borders of skin, fat, fibroglandular and potentially cancerous tissue in a breast image should appear the same in both components of the complex permittivity despite their differing quantitative values.

The second closely-related observation is that both components of the complex permittivity are correlated based on the expected tissue type in the human breast. For example, areas of high dielectric constant generally correspond to areas of high conductivity, and vice versa, which can be illustrated by modelling the dielectric properties of these tissues. Thanks to a number of studies that have directly measured the permittivity values of human tissue samples *ex vivo*, the expected dielectric quantities of all types of breast tissues are well known, and robust fitted Cole-Cole models have been developed to accurately simulate them for gigahertz-band frequencies [1]. These Cole-Cole models are commonly used as physics-based compact representations of wideband frequency-dependent dielectric properties [64], and take the following form:

$$\begin{aligned} \hat{\varepsilon}_r(\omega) &= \varepsilon'_r(\omega) - j\varepsilon''_r(\omega) \\ &= \varepsilon_\infty + \frac{\varepsilon_s - \varepsilon_\infty}{1 + (j\omega\tau)^{1-\alpha}} + \frac{\sigma_i}{j\omega\varepsilon_0} \end{aligned} \tag{2.1}$$

where ω is the angular frequency, $\hat{\varepsilon}_r$ is the frequency-dependent complex relative dielectric permittivity composed of the dielectric constant ε'_r and the dielectric loss ε''_r, the latter of which can be converted to effective conductivity, $\sigma_{\text{eff}}(\omega) = \omega\varepsilon_0\varepsilon''(\omega)$. The

fitted parameters include ε_s and ε_∞ as the static and "infinite frequency" dielectric constants, the time constant τ, exponent parameter α, and ionic conductivity σ_i of the lossy material. If one assumes $\alpha = 0$, Equation 2.1 reduces to a Debye model.

If one plots the dielectric properties for breast tissues using Equation 2.1, the values of dielectric constant and conductivity at low gigahertz-band frequencies form reasonably discrete ranges, covering a spectrum related to their adipose tissue content, as shown in Figure 2.1. This correlation has been pointed out before and used to tailor constraints on inversions of dielectric parameters in previous studies, specifically in simultaneous multi-frequency inversion schemes that reconstruct frequency-dependent Debye models themselves (inverting ε_∞ , $\delta\varepsilon = \varepsilon_s - \varepsilon_\infty$, and σ_i), rather than individual complex permittivity values [65, 66].

For instance, in [65], the authors restrict the bounds on $\delta\varepsilon$ and σ_i during each iteration of DBIM based on comparisons to predefined ratio ranges of these values with ε_∞ for adipose and fibroglandular tissues. Another interesting recent approach by Ambrosanio *et al.*, employing a DBIM-based adaptive multi-threshold iterative shrinkage thresholding algorithm (AMTISTA) solver, involves excluding pixels that have exceeded predetermined minimum and maximum bounds from being updated altogether, creating new "masked" contrast functions as these components of the image are windowed out of the inversion problem [66].

As aforementioned, however, the imaging algorithm demonstrated in this work is CSI-based and does not employ simultaneous multi-frequency inversion of Debye model parameters, instead reconstructing individual complex permittivity values for each frequency in a step-wise "frequency hopping" fashion. The simple approach to constraining and refining the solution detailed here involves a post-processing step after each individual inversion to identify the type of tissue likely represented in each

pixel of the image.

To take advantage of the structural relationship between the real and imaginary components of breast tissues' complex permittivity, microwave images of these tissues can be classified according to their well-reconstructed dielectric constant, and the expected value of their imaginary component determined for the next frequency in a reconstruction sequence. These values can then be mapped onto breast images to overwrite the original imaginary component that has presumably been poorly recovered and generate a "better" initial guess for the inversion at the next frequency.

Returning to Figure 2.1, one will note that the real parts of the permittivity of breast tissues do not drastically change across frequencies of interest for imaging (1.0–4.0 GHz). Consequently, reconstructed values of the dielectric constant at a lower frequency (1.0 GHz, for instance) are reasonable approximations to those of higher frequencies (2.0 GHz), and can remain unaltered in the initial guess for the next frequency in the inversion sequence.

Using parameters empirically fitted to match the dielectric properties of excised breast tissues [1], if one has only prior knowledge of the reconstructed real part of the permittivity (ε_r'), Equation 2.1 can be used to provide the desired association between these dielectric constants and the expected values of dielectric loss (ε_r''). Specific ranges of values can then be established for each type of tissue expected to appear in a given image.

An example of the various domains of dielectric constants for breast tissues at 1.0 GHz, along with their corresponding range of imaginary components for a frequency of 2.0 GHz, is shown in Table 2.1. The boundaries of the domains are established originally from the 25th and 75th percentile fitted single-pole Cole-Cole models of the tissue (using parameters from measurements of breast cancer surgical

specimens in [1]) and are expanded or truncated appropriately when gaps or overlap occur, such that any given value of dielectric constant is guaranteed to be classified as one tissue type only.

Dielectric constants from breast images that fall within a given domain are subject to a simple linear interpolation between the particular tissue's boundary values and its 50th percentile fitted Cole-Cole model to determine its imaginary component, the total dielectric loss ε_r''. As previously mentioned, since the profile of the real part of $\hat{\varepsilon}_r$ is fortunately quite flat across the range of interest for imaging (Figure 2.1), for the purposes of interpolation of the imaginary part, the reconstructed dielectric constant for one frequency is assumed to be interchangeable for the next frequency in a given frequency-hopping succession.

2.3.3 Implementation considerations

There are a few additional scope limitations for the integration of the tissue-dependent mapping technique into CSI that are noteworthy. It has been previously observed that if the imaginary part of a tissue-mapped initial guess is "anchored" in place for a successive frequency inversion (*i.e.* unmodified throughout the iterative optimization), the real part of the final image improves [39]. Allowing the imaging algorithm to continue to reconstruct both the real and imaginary parts during intermediate solutions is an option, but the observed deterioration of the imaginary part at higher frequencies continues to occur, and thus produces less impressive results than "anchoring" the imaginary component.

Another option relates to the use of this mapping technique in single-frequency imaging, or within one frequency of a multi-frequency succession (*i.e.* two or more consecutive frequencies in the sequence are the same). In single-frequency imaging,

Table 2.1: Example of tissue mapping from 1.0 GHz to 2.0 GHz

Tissue type (Breast)	Domain of dielectric constant (ε'_r at 1.0 GHz)	Range of dielectric loss (ε''_r at 2.0 GHz)
Adipose	5.19 – 7.93	0.71 – 1.45
Transitional	7.94 – 44.88	1.46 – 11.24
Fibroglandular	44.89 – 51.21	11.25 – 12.76
Carcinoma	51.22 – 59.98	12.77 – 15.17

this would amount to continuously restarting the imaging process at the same frequency after performing the tissue mapping technique on the previous solution (ostensibly providing the algorithm with better and better initial guesses). Experimentation with this approach was, in fact, the authors' first application of tissue-dependent mapping, and the promising results obtained from those trials served as motivation for this study's primary focus of stabilizing inversions at progressively higher frequencies.

A final consideration has been raised with regards to the use of inhomogeneous backgrounds, an imaging technique that has been developed at the University of Manitoba and used successfully for several years [67]. There may be a substantial benefit to taking intermediate results subjected to tissue-dependent mapping and using them as the imaging background for subsequent frequency-hopping reconstruction sequences, but such an application is beyond the scope of this study. A first-pass investigation of the use of this mapping technique only for initial guesses is warranted before more complicated applications are considered.

2.3.4 Frequency cycling

To the authors' knowledge, there has never been a MWI study demonstrating a frequency-hopping imaging technique that cycles the image obtained from the highest

frequency data back down to the lowest frequency dataset to restart the sequence. This practice has perhaps been avoided due to a reasonable but untested assumption that there is nothing further to gain by inserting a high-resolution initial guess into data that is in theory only capable of producing low-resolution images, and that the attempt would in fact result in a degradation of image quality. It was discovered, however, that when such a "frequency cycling" process was put into practice, the resulting repetition of low-frequency reconstructions preserved the finer detail acquired from higher frequency data while refining and softening overshoot artifacts and noise reconstruction that often plague these same high-frequency inversions. The ultimate result is a more accurate detailed image using frequency cycling than would be produced through the same number of iterations spent on high-frequency data inversion alone, especially when combined with the previously described tissue mapping technique. Frequency cycling was therefore adopted as a new component of the reconstruction approach outlined herein to demonstrate its benefit, though a determination of the optimal number of cycles to halt reconstructions has been left for future study.

2.3.5 Full description of multi-frequency imaging procedure

Taking into account tissue-dependent mapping and frequency cycling techniques that modify the conventional approach to frequency-hopping reconstruction, a new imaging procedure was devised as follows, employing the DGM-CSI formulation and based on the description outlined in [39]:

1. The real and imaginary parts of the complex permittivity are reconstructed using the lowest frequency data available (*e.g.* 1.0 GHz).

2. A point-by-point search through the reconstructed real part of each nodal basis coefficient in the DGM-CSI mesh is performed to classify the type of breast tissue based on the range of expected values of dielectric constant at that frequency (such as those shown in Table 2.1).

3. An initial guess for the next imaging frequency (*e.g.* 2.0 GHz) is then generated using the unmodified real part of the reconstructed ε_r at the mesh nodal points, and a new imaginary part created from a simple linear interpolation of the expected range of dielectric loss values, based on the appropriate Cole-Cole models of tissues classified in Step 2. This process ensures that the structural similarities between the real and imaginary parts of the solution are maintained.

4. This new initial guess for the complex permittivity is used to run the inversion algorithm at the next frequency (*e.g.* 2.0 GHz). Only the real part is updated to converge to a new solution; the imaginary part is kept constant.

5. If more than two frequencies are used in the frequency hop, steps 2–4 are repeated as necessary until the reconstruction of the final frequency of the succession is complete (*e.g.* 3.0 GHz). This succession may include returning the inversion algorithm to the lowest frequency data ("frequency cycling").

The implementation of this procedure is subject to several distinct choices in addition to the scope limitations already mentioned in Section 2.3.3. Of note, in this work:

- To simplify comparisons between imaging scenarios, a stopping condition based on a fixed number of iterations is selected for each reconstruction.

- Only frequency successions consisting of complete frequency cycles are demonstrated (*e.g.* always terminating after an inversion of the highest frequency data).
- Following the very first reconstruction, the procedure presented here never reconstructs the imaginary part of the complex permittivity.
- As mentioned, this imaging procedure is fully applicable to any CSI formulation.

2.3.6 Synthetic breast models

Initial testing of the described tissue-dependent mapping technique and frequency cycling was carried out on synthetic transverse magnetic (TM) data collected from a two-dimensional MRI-derived BI-RADS Category D ("extremely dense") healthy breast model supplied by the University of Wisconsin's public database (ID: 070604PA2) with complex permittivity values calculated from fitted single-pole Cole-Cole models [1] (Figure 2.2).

To demonstrate the robustness of the technique across different breast models and explore imaging of a realistic disease process, a more thorough analysis was undertaken on a BI-RADS Category C ("heterogeneously dense") 2D breast model supplied by the University of Calgary, derived from a coronal MRI slice of a cancer patient with a breast tumour visible at the "3 o'clock" position; the model is depicted at three different frequencies in Figure 3.4, once again illustrating the similarities between breast tissues' dielectric permittivity at the low-gigahertz band. The values of the complex permittivity in this case were calculated for every frequency using a fitted single-pole Debye model then subjected to random perturbations of $\pm$ 10% [68]. This process ensured that the 2D synthetic breast tissues were seeded with dielectric

values generated using different physics-based models than those used in the tissue-dependent mapping process.

Data was collected for both 2D synthetic breasts in a low-loss background of $\epsilon_r = 23 - 1.13i$ with 24 transmitters and 24 receivers evenly distributed at a radius of 10 cm, employing a finite-element method (FEM) forward solver with a finely-discretized mesh independent from that used for the DGM-CSI inversion. These meshes employed triangular elements of an average edge length of roughly 1 mm for the FEM forward solver depending on the breast phantom and excitation frequency, and approximately 5 mm for the DGM-CSI inversion mesh (with the full discretization of the inverse problem being subjected to a 4th-order nodal coefficient expansion in DGM-CSI), using ideal 2D line sources as transmitter models. The synthetic data was collected for open / absorbing boundary conditions at 1.0 GHz, 2.0 GHz, and 3.0 GHz.

In order to further validate the imaging technique to problems involving resonant enclosures and lower frequency bandwidths, synthetic data was also generated for the University of Calgary Category C model using a perfect electrical conducting (PEC) boundary with a radius of 15 cm at 1.0 GHz, 1.25 GHz, and 1.5 GHz (original models not shown). This latter set of simulations better reflects the environment and capabilities of a recent University of Manitoba imaging system prototype that employs a metallic chamber [4]. The use of such a design not only shields the imaging chamber from the external instrumentation, cabling, and electromagnetic noise, but has several other advantages which have been investigated both theoretically and experimentally in recent years [69, 70]. Among these advantages include the ability to use a lossless or low-loss matching medium to deliver more energy into the target, resulting in a higher SNR [69].

In all cases, the E_z scattered electric field data was corrupted by uniformly-distributed noise at 5% of the maximum field magnitude. The only prior information used during inversions was the outer boundary of the skin, which served as the problem's imaging domain. The skin thickness and inner skin boundary both remained unknown.

2.3.7 Error calculation

In order to provide an objective method of evaluating the DGM-CSI algorithm's performance for differing imaging scenarios, the reconstruction results of the Category C models were compared to the original synthetic models using simple error metrics involving the differences of complex permittivity in each pixel. Since the models and reconstructions each employed different underlying meshes, their complex permittivity values were interpolated onto a common 250×250-pixel square grid ($N = 62500$) encompassing the area covered from $(x_1, y_1) = (-0.07, -0.07)[m]$ to $(x_2, y_2) = (0.07, 0.07)[m]$. Two primitives commonly used to evaluate performance in image processing are the relative error of the L_1 and L_2 norms of the difference between two images (the actual complex permittivity $\hat{\varepsilon}_r^{\text{act}}$ and the reconstructed complex permittivity $\hat{\varepsilon}_r^{\text{rec}}$) over each pixel k. These metrics are referred to here as relative error norms REN_1 and REN_2 for convenience and are calculated and expressed as per-

centages, where

$$\begin{aligned} \mathrm{REN}_1(\hat{\varepsilon}_r^{\,\mathrm{act}}, \hat{\varepsilon}_r^{\,\mathrm{rec}}) &= \frac{\|\hat{\varepsilon}_r^{\,\mathrm{act}} - \hat{\varepsilon}_r^{\,\mathrm{rec}}\|_1}{\|\hat{\varepsilon}_r^{\,\mathrm{act}}\|_1} \times 100\% \\ &= \frac{\sum_{k=1}^{N} |\hat{\varepsilon}_r^{\,\mathrm{act}}(k) - \hat{\varepsilon}_r^{\,\mathrm{rec}}(k)|}{\sum_{k=1}^{N} |\hat{\varepsilon}_r^{\,\mathrm{act}}(k)|} \times 100\%, \end{aligned} \tag{2.2}$$

$$\begin{aligned} \mathrm{REN}_2(\hat{\varepsilon}_r^{\,\mathrm{act}}, \hat{\varepsilon}_r^{\,\mathrm{rec}}) &= \frac{\|\hat{\varepsilon}_r^{\,\mathrm{act}} - \hat{\varepsilon}_r^{\,\mathrm{rec}}\|_2}{\|\hat{\varepsilon}_r^{\,\mathrm{act}}\|_2} \times 100\% \\ &= \sqrt{\frac{\sum_{k=1}^{N} [\hat{\varepsilon}_r^{\,\mathrm{act}}(k) - \hat{\varepsilon}_r^{\,\mathrm{rec}}(k)]^2}{\sum_{k=1}^{N} [\hat{\varepsilon}_r^{\,\mathrm{act}}(k)]^2}} \times 100\%. \end{aligned} \tag{2.3}$$

Since the square grid covers an area outside of the imaging domain of the problem which consists of unaltered background permittivity in both the original model and reconstruction, the raw numerical value of the norms will be slightly artificially reduced. There is little value in interpreting individual error magnitudes, however; the REN serves primarily as a means of comparison to demonstrate improvement between imaging scenarios and show trends of solution convergence by iteration.

2.4 Results and Discussion

2.4.1 Tissue-dependent mapping and frequency hopping

The imaging results of a frequency-hopping simulation beginning with a DGM-CSI inversion of the 1.0 GHz data, and continuing through the 2.0 GHz and 3.0 GHz

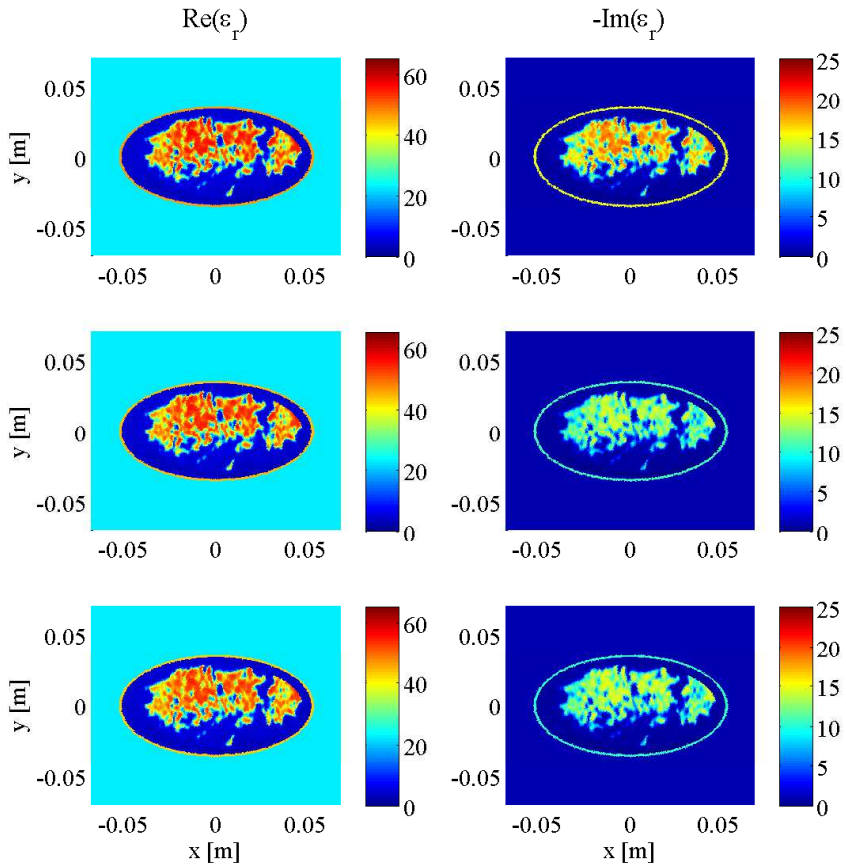

Figure 2.2: Complex dielectric properties of University of Wisconsin synthetic breast model at 1.0 GHz (top), 2.0 GHz (middle) and 3.0 GHz (bottom).

data sequentially, without any modification of the intermediate results and using a fixed number of 500 iterations per frequency, are shown in Figure 2.4 for the Category D model and Figure 2.6 for the Category C model. Reconstructions employing the imaginary-component mapping technique described in Section 3.3.2 for the intermediate solutions are also shown, in Figures 2.5 and 2.7, for Category C and D models respectively. Note that since the 1.0 GHz reconstructions are (and should be) identical in these cases, they have been omitted; only the 2.0 GHz and 3.0 GHz reconstructions are thus shown in Figures 2.5 and 2.7.

Although DGM-CSI, much like other iterative algorithms, performs reasonably

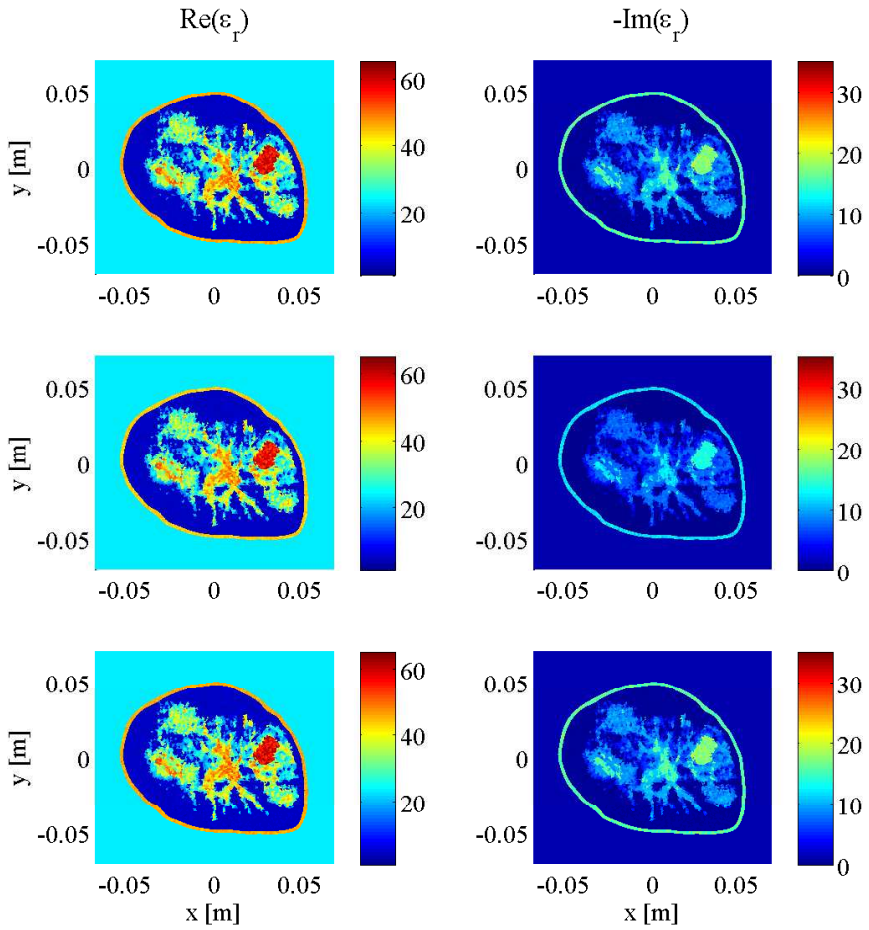

Figure 2.3: Complex dielectric properties of University of Calgary 2D synthetic breast model at 1.0 GHz (top), 2.0 GHz (middle) and 3.0 GHz (bottom).

well in recovering the real component of breast models it reconstructs, it has difficulty producing an accurate distribution of the imaginary part, most notably at higher frequencies. This deficiency is illustrated in the 2.0 GHz and 3.0 GHz open-boundary inversions of the Category D breast model in Figure 2.4 and of the Category C breast model in Figure 2.6. It is clear that the mapping technique and "anchoring" of the imaginary component at each subsequent frequency stage in Figure 2.7 offers a substantial benefit to the quality of the real part of the reconstructions following the same number of iterations. Areas of finer anatomic detail in the original model, for

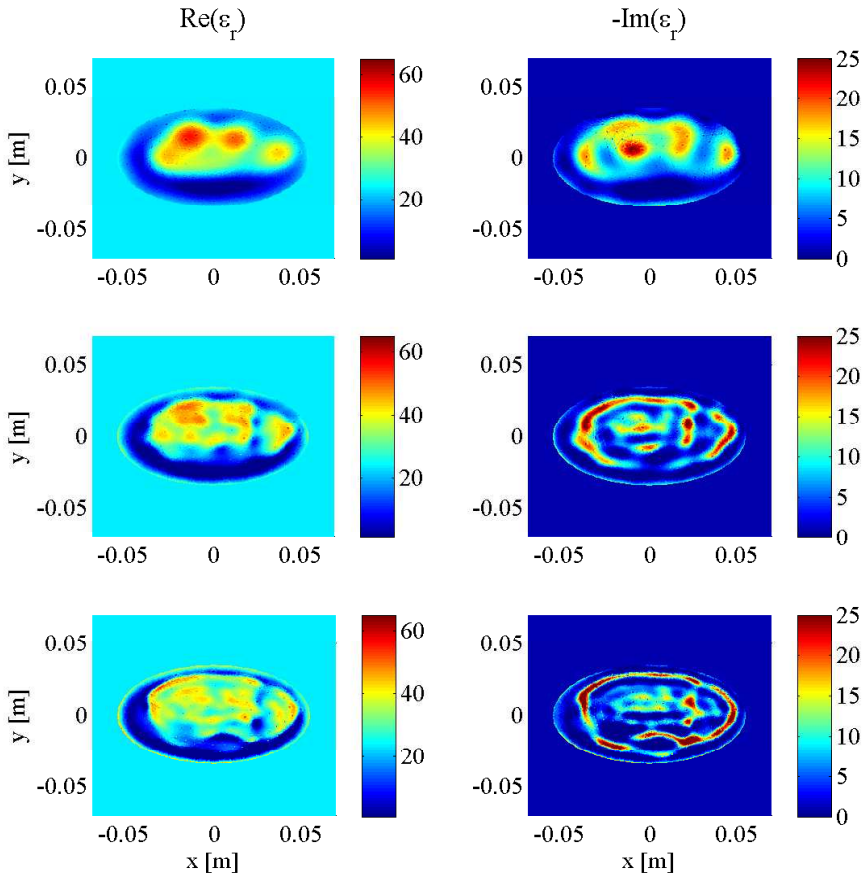

Figure 2.4: DGM-CSI frequency-hopping reconstructions of complex dielectric properties of University of Wisconsin synthetic breast model at 1.0 GHz (top), 2.0 GHz (middle) and 3.0 GHz (bottom), without modifying intermediate solutions.

instance, emerge from the 3.0 GHz data inversion in the real part of Figure 2.7 that are not present in Figure 2.6.

2.4.2 Tissue-dependent mapping and frequency cycling

Use of frequency cycling is demonstrated in Figure 2.8 without any modification of initial guesses and in Figure 2.9 employing the tissue-dependent mapping technique for the Category C model only; the 3.0 GHz solution from Figure 2.6 and Figure 2.7 respectively are fed back into the DGM-CSI algorithm as an initial guess for the

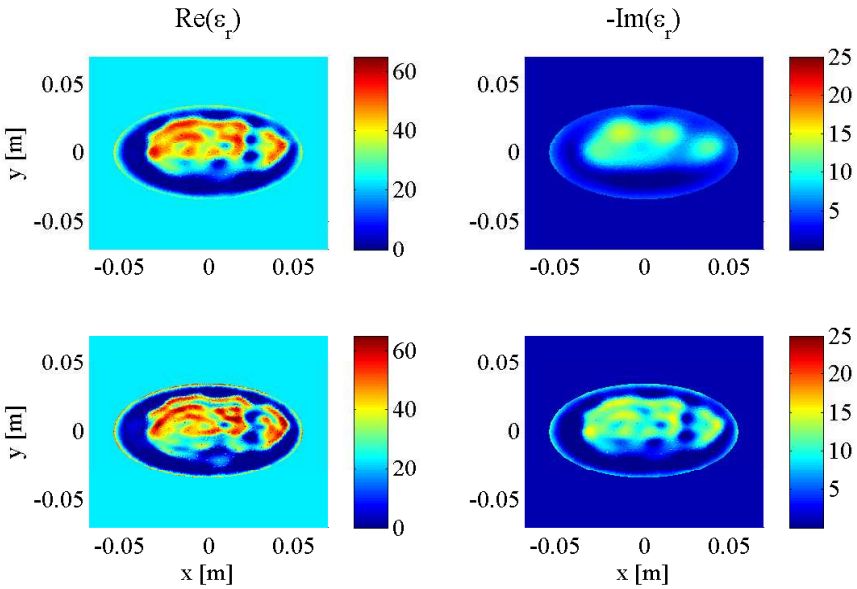

Figure 2.5: DGM-CSI frequency-hopping reconstructions of complex dielectric properties of University of Wisconsin synthetic breast model at 2.0 GHz (top), and 3.0 GHz (bottom) using tissue-dependent mapping technique.

1.0 GHz data, and the frequency hop proceeds sequentially once more through the 2.0 GHz and 3.0 GHz data in fixed 500-iteration reconstructions. The REN values for all six stages of reconstruction depicted in Fig. 2.6–2.9 are plotted in Fig. 2.10 for the Category C model, showing consistently lower error values when tissue-dependent mapping is used. Included for comparison are the REN values of an imaging scenario again employing tissue-dependent mapping as the initial guess for each frequency but allowing the imaginary part to be modified by DGM-CSI at all times (reconstructions not shown). This additional case illustrates the benefit of anchoring the imaginary part in place, as discussed in the imaging procedure implementation considerations of Section 2.3.3.

Further modest increases in image quality are noted when the highest-frequency reconstructions are cycled back into the lowest-frequency inversions, whether or not tissue-dependent mapping is used (Figure 2.8, 2.9), though the deterioration of the

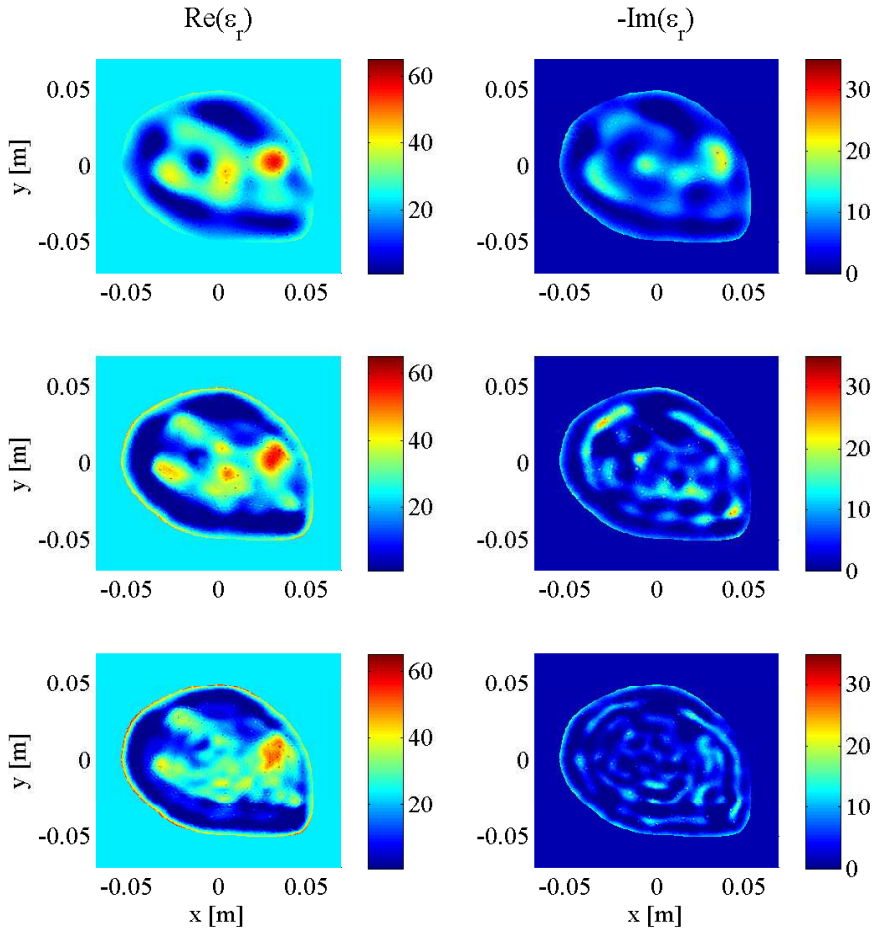

Figure 2.6: DGM-CSI frequency-hopping reconstructions of complex dielectric properties of synthetic breast model at 1.0 GHz (top), 2.0 GHz (middle) and 3.0 GHz (bottom), without modifying intermediate solutions.

imaginary part does not resolve without it. This demonstrates (as aforementioned) that high-resolution initial guesses are not necessarily subject to degradation when used with reconstructions of low-frequency data, and that the stability of such data can serve to enhance images containing finer details extracted from noisier high-frequency reconstructions. The lower REN values of the dashed and dotted trendlines of Figure 2.10 compared to the solid plot representing unmodified initial guesses reflect the fact that an improvement in image quality with tissue-dependent mapping and

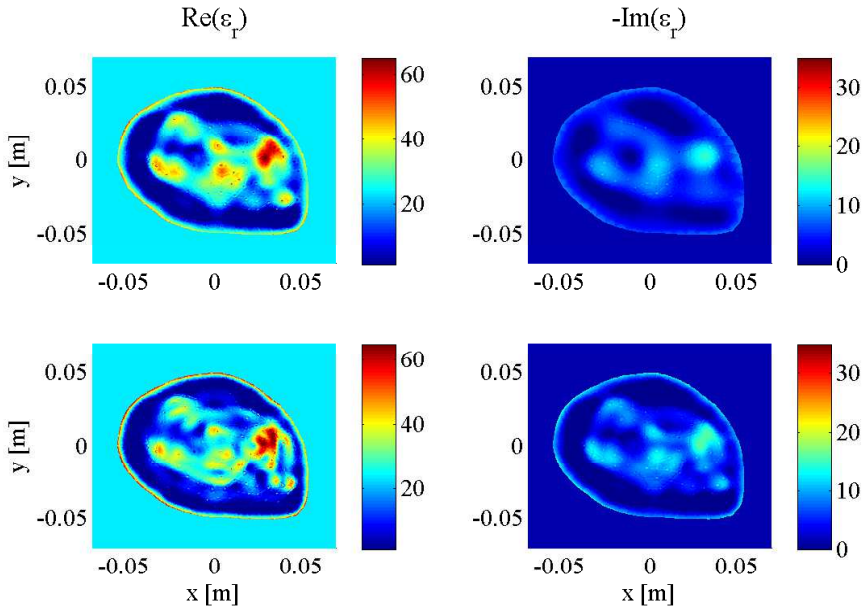

Figure 2.7: DGM-CSI frequency-hopping reconstructions of complex dielectric properties of synthetic breast model at 2.0 GHz (top) and 3.0 GHz (bottom) using tissue-dependent mapping technique.

frequency cycling is observed.

2.4.3 Frequency cycling vs. frequency hopping

While the advantage of combining the use of tissue-dependent mapping of the imaginary part and frequency cycling is evident, a separate simulation was carried out to isolate the effect of frequency cycling on its own. The resulting REN values of a direct 500-iteration per frequency reconstruction, beginning at 1.0 GHz, jumping to 2.0 GHz and terminating after 3.0 GHz, compared to a reconstruction of the same frequency datasets but using 250 iterations per frequency and cycled back once to 1.0 GHz, with no modification of intermediate results, are shown in Figure 2.11. Note that the REN values do not monotonically decrease since the frequency-cycled reconstructions appear to worsen temporarily, but the final result following the last

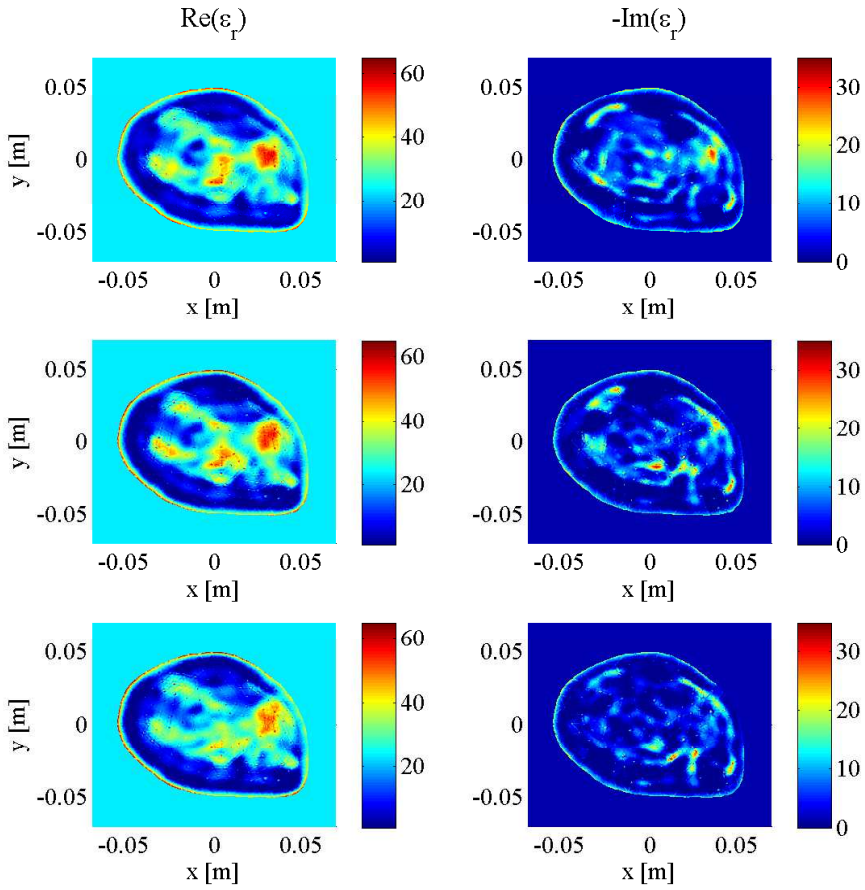

Figure 2.8: DGM-CSI frequency-cycled reconstructions of complex dielectric properties of synthetic breast model at 1.0 GHz (top) using final reconstruction of Fig. 2.6 as initial guess, 2.0 GHz (middle) and 3.0 GHz (bottom), without modifying intermediate solutions.

3.0 GHz reconstruction shows a modest benefit with frequency cycling, after the same number of iterations (1500 total). Although the intermediate and final reconstructions of each case (not shown) appear subjectively similar, it is worth noting that the choices of 500 iterations versus 250 iterations for each frequency was arbitrary. Preliminary incorporation of objective stopping criteria rather than a fixed-iteration approach has shown promise in accentuating the benefit of frequency-cycled reconstructions, and is being studied further.

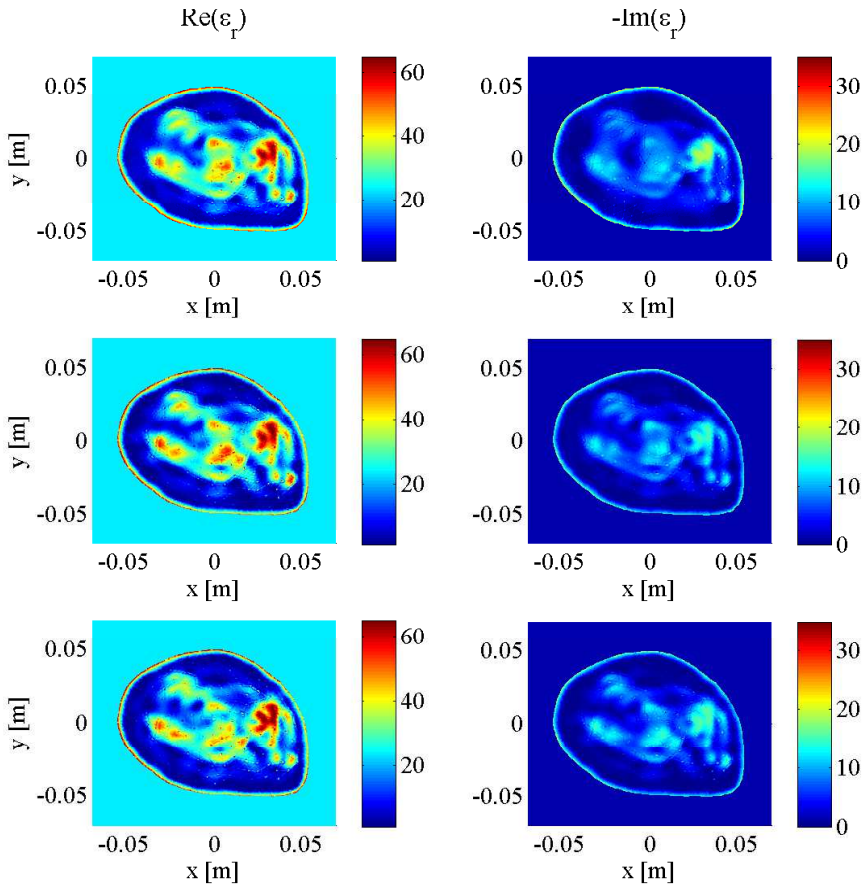

Figure 2.9: DGM-CSI frequency-hopping reconstructions of complex dielectric properties of synthetic breast model at 1.0 GHz (top) using final reconstruction of Fig. 2.7 as initial guess, 2.0 GHz (middle) and 3.0 GHz (bottom) using tissue-dependent mapping technique.

2.4.4 Imaging with PEC boundaries

To demonstrate this method's robustness to a smaller, more realistic frequency bandwidth and different boundary conditions, a set of simulations similar to those carried out in the previous section were performed, but using PEC boundaries and data from frequencies of 1.0 GHz, 1.25 GHz and 1.50 GHz, as mentioned in Section 3.3.6. The final imaging results for two scenarios, together with one additional intermediate result, are shown in Figure 2.13. A plot of the relative error norms similar to the open boundary cases, employing REN calculations based on the current

reconstruction frequency's model, is also provided in Figure 2.12. For these simulations, a frequency-hopping sequence of reconstructions was completed first without the use of tissue-dependent mapping, using an arbitrary 400 iterations per frequency for a total of 1200 iterations. This "conventional" approach was compared to reconstructions using 200 iterations per frequency (subtotaling 600 iterations per set) and tissue-dependent mapping and anchoring of the imaginary part, with a single repetition through the frequency cycle performed for an equal total of 1200 iterations. The positive effect of frequency cycling with tissue-dependent mapping on imaging results is again evident from Figure 2.12 and Figure 2.13. However, it is again observed that the REN values are not monotonically decreasing, and that in this case the final result of the new imaging approach was not the optimal solution; the minimum relative error norms occurred following the second reconstruction of 1.0 GHz data (after 800 iterations), and it is subjectively the best reconstruction when compared to those of the final results of (see bottom of Figure 2.13).

As this PEC-bounded case represents a more difficult problem than the open boundary case and is performed with data taken at lower frequencies, it was not expected that the results would be as impressive as earlier scenarios. However, it is again clear from the images in Figure 2.12 that there is an improvement in the recovery of the imaginary component when tissue-dependent mapping is used (middle and bottom); a modest improvement in the real part of ε_r for these scenarios is also noted. The fact that an apparent increase in relative error norm and subjective decline in imaging quality may be occurring after certain numbers of iterations in frequency-cycled scenarios further motivates the need for objective stopping criteria for the algorithm to halt reconstructions at an optimal error minimum, presumably representing the best possible result.

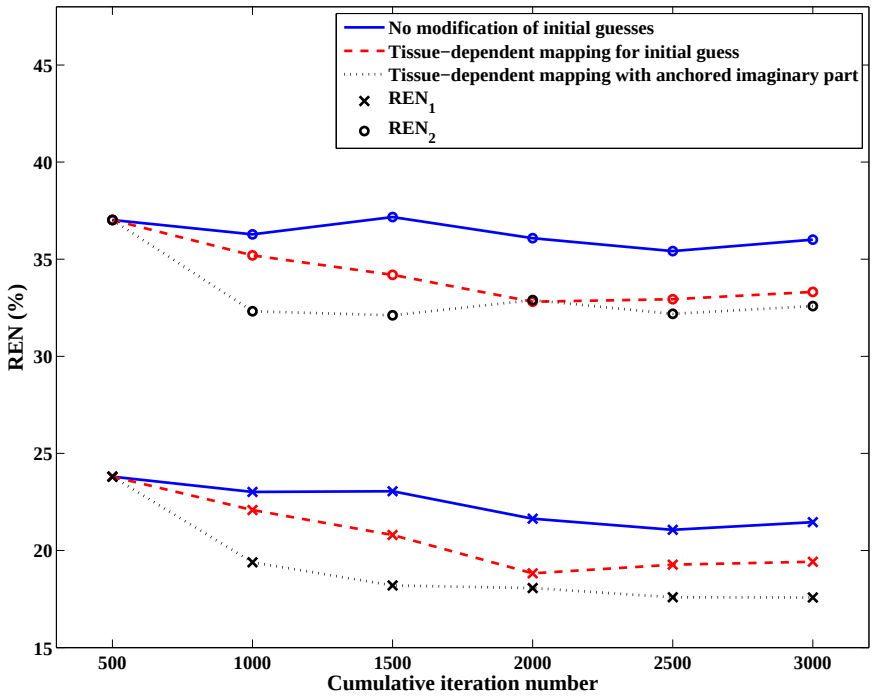

Figure 2.10: Relative error norms of the fixed-iteration imaging scenarios depicted in Fig. 2.6–2.9, including an additional case allowing reconstruction of both real and imaginary parts of the permittivity at all times.

2.5 Conclusion

It has been shown that the implementation of the described tissue-dependent mapping and frequency cycling techniques has had a significant positive effect on resulting 2D synthetic microwave breast DGM-CSI reconstructions using fixed-iteration scenarios. Gains in image quality imparted through these modifications to the imaging algorithm are preserved across different frequency bandwidths and boundary conditions. An open question relating to the application of this technique lies in the choice of stopping criteria for the algorithm, to determine the number of iterations that should be expended on each frequency hop and the number of frequency cycles that should be performed before terminating the reconstruction entirely. Significant efforts have been made developing an automated approach to this problem, employing

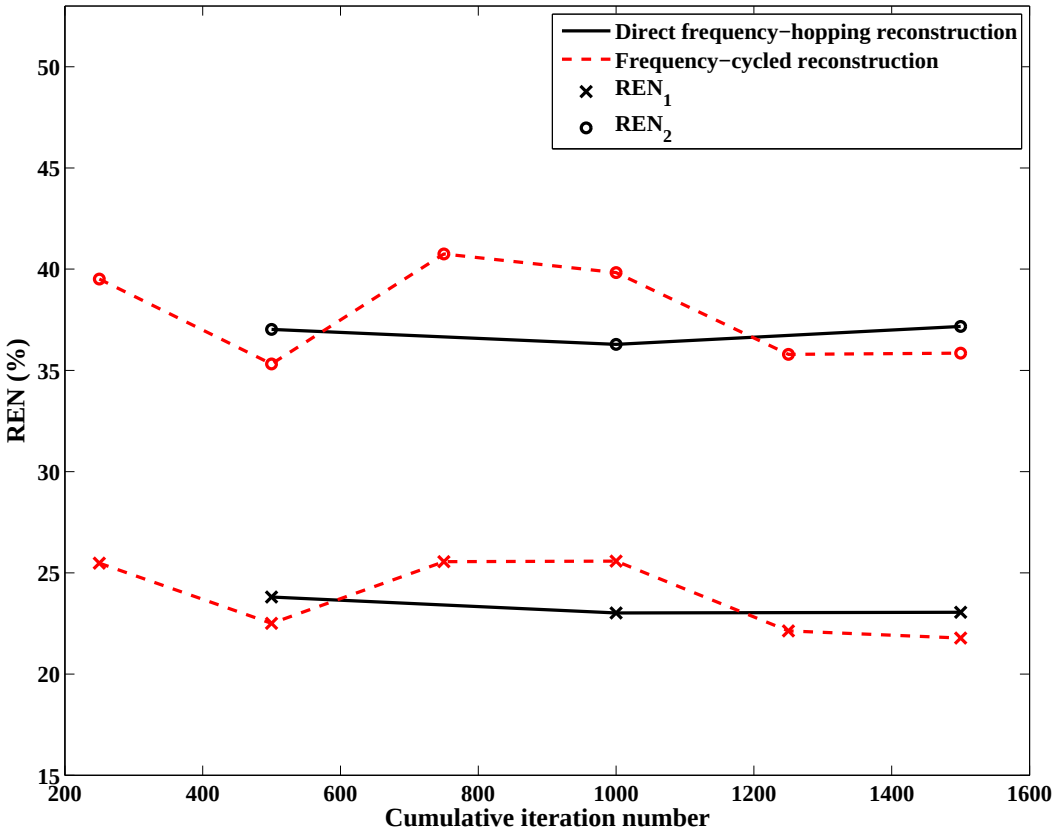

Figure 2.11: Relative error norms of a direct frequency-hopping reconstruction terminating after 3.0 GHz (at 500 iterations per frequency) versus a frequency-cycled reconstruction of the same data terminating after 3.0 GHz following a single cycle back to 1.0 GHz (at 250 iterations per frequency)

a thorough statistical analysis of the algorithm's data error, and a detailed study is forthcoming. Furthermore, as only 2D simulations have been tested in this study, a logical next step is the application of this technique to the 3D DGM-CSI algorithm developed at the University of Manitoba; preliminary efforts to that end are ongoing.

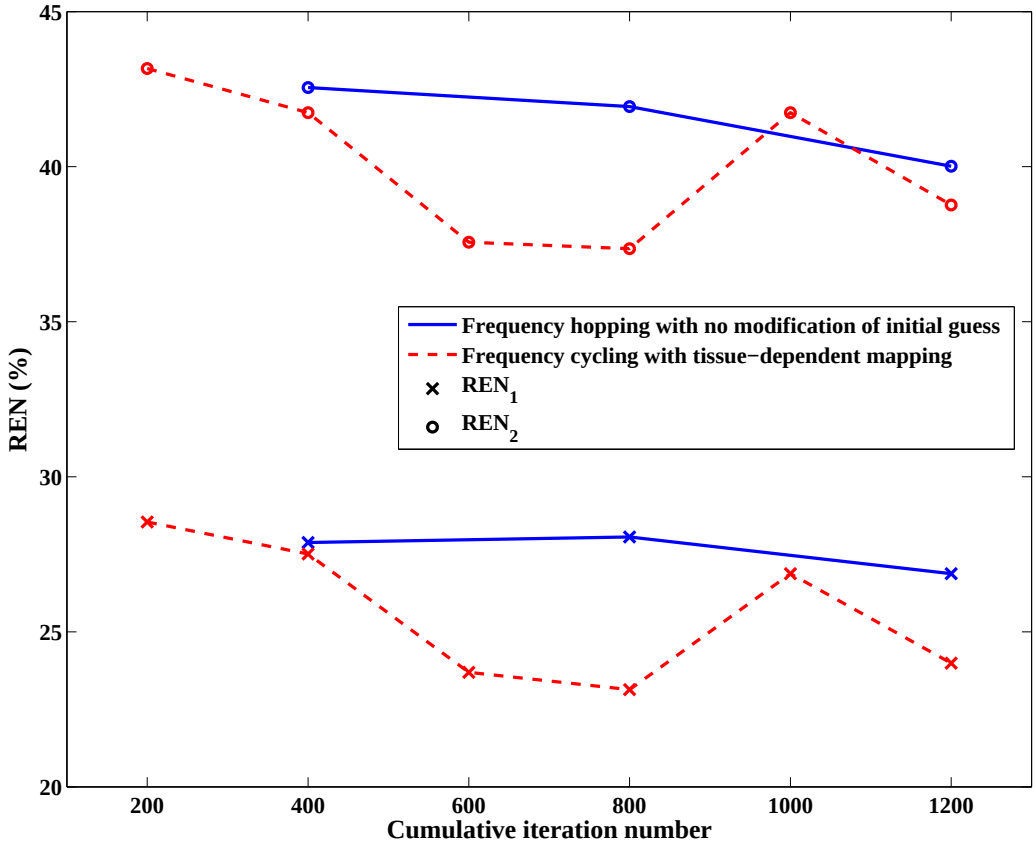

Figure 2.12: Relative error norms of reconstructions with PEC boundaries. The first scenario (solid line) uses standard frequency hopping from 1.0 GHz, 1.25 GHz and 1.5 GHz at 400 iterations per frequency, without any modification to the initial guess after each frequency hop. The second scenario (dashed line) uses tissue-dependent mapping and anchoring of the imaginary part for the initial guess after each frequency change, and performs a single repeat cycle through each frequency (200 iterations per frequency).

Acknowledgment

The authors would like to thank the University of Calgary for providing the 2D Category C synthetic breast model used for the reconstructions presented in this work.

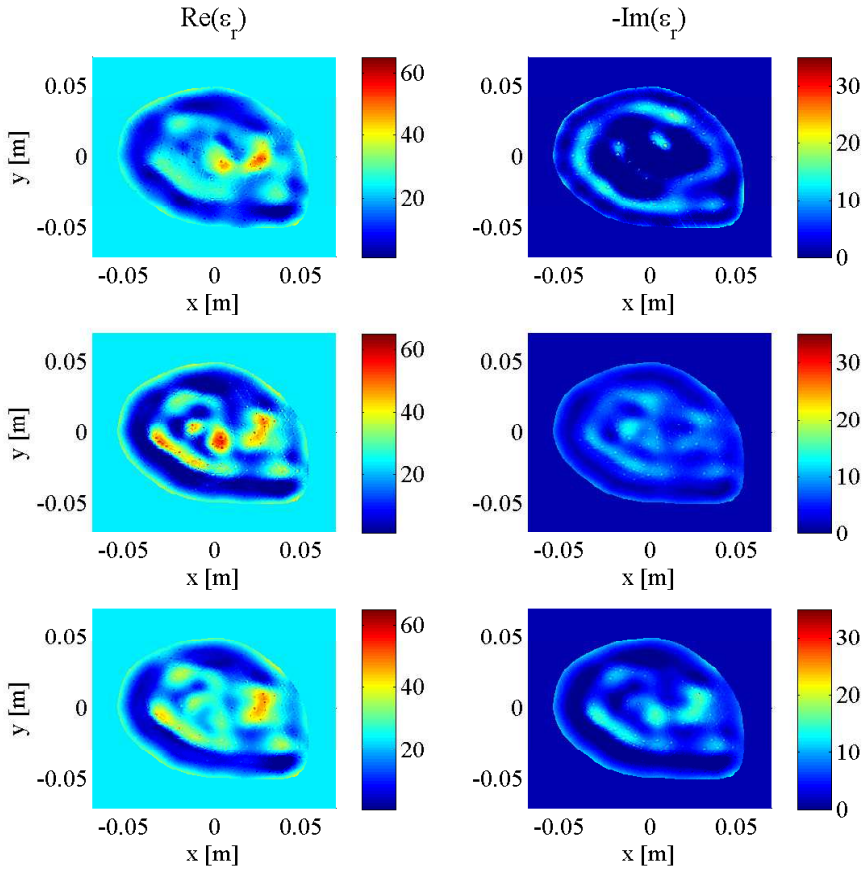

Figure 2.13: Results of DGM-CSI complex dielectric property reconstruction of PEC-bounded synthetic breast model using 1.0 GHz–1.5 GHz data. Top: frequency hopping without modification of intermediate initial guesses (1200 iterations total). Middle: frequency cycling with tissue-dependent mapping of the imaginary part (1200 iterations total). Bottom: an intermediate result using frequency cycling and tissue-dependent mapping of imaginary part, with the lowest relative error norm values (800 iterations total, halted following second reconstruction at 1.0 GHz).

3

Article 2*: Novel Stopping Criteria for Optimization-Based Microwave Breast Imaging Algorithms

3.1 Abstract

A discontinuous Galerkin formulation of the Contrast Source Inversion algorithm (DGM-CSI) for microwave breast imaging employing a frequency-cycling reconstruction technique has been modified here to include a set of automated stopping criteria that determine a suitable time to shift imaging frequencies and to globally terminate the reconstruction. Recent studies have explored the use of tissue-dependent geometrical mapping of the well-reconstructed real part to its imaginary part as initial guesses during consecutive frequency hops. This practice was shown to improve resulting 2D images of the dielectric properties of synthetic breast models, but a fixed number of iterations was used to halt DGM-CSI inversions arbitrarily. Herein, a new set of stopping conditions is introduced based on an intelligent statistical analysis of

*Reprinted with permission from Cameron Kaye, Ian Jeffrey and Joe LoVetri, "Novel Stopping Criteria for Optimization-Based Microwave Breast Imaging Algorithms," *Journal of Imaging* Special Issue *Microwave Imaging and Electromagnetic Inverse Scattering Problems*, vol. 5, no. 5, May 2019.

a window of past iterations of data error using the two-sample Kolmogorov-Smirnov (K-S) test. This non-parametric goodness-of-fit test establishes a pattern in the data error distribution, indicating an appropriate time to shift frequencies, or terminate the algorithm. The proposed stopping criteria are shown to improve the efficiency of DGM-CSI while yielding images of equivalent quality to assigning an often liberally overestimated number of iterations per reconstruction.

3.2 Introduction

Microwave imaging (MWI) has made steady progress towards widespread clinical application in breast cancer detection and monitoring over the past decade, offering a safety advantage over established x-ray-based modalities due to its use of non-ionizing radiation and a significant cost benefit over magnetic resonance imaging (MRI). While its currently attainable spatial resolution does not match that of cancer screening tools like mammography, concurrent use of MWI of the breast in its current state could lead to decreased false positive rates among certain population groups, particularly pregnant women or those with radiographically dense ("Category C" and "Category D") breasts, as classified by the American College of Radiology's Breast Imaging Reporting and Data System (BI-RADS) [22, 23].

Methods of utilizing MWI for biomedical applications have been investigated for almost half a century [71, 72]. Some recent representative research can be found in [73]. MWI algorithms can be split into those producing qualitative images, where the reconstructed value at each pixel is a relative quantity, and those producing quantitative reconstructions of a physical property, typically the complex-valued permittivity. Examples of qualitative algorithms are those utilized in so-called radar imaging techniques [74], and those retrieving only qualitative aspects of the target, such as

its support [75, 76]. The interest in this paper are quantitative imaging methods that solve the full electromagnetic inverse problem.

It is well known that the electromagnetic inverse problem associated with MWI, where one attempts to reconstruct the complex-valued permittivity of an object-of-interest (OI), is ill-posed [77]. The ill-posedness stems from the non-uniqueness of the inverse-source problem where one attempts to reconstruct the electromagnetic sources responsible for a remotely measured field. In the electromagnetic inverse problem, these sources are the contrast-sources that are illuminated by the interrogating field. Various regularization techniques have been developed over several decades of research to deal with the ill-posedness of the problem [78]. The electromagnetic inverse problem is not only ill-posed but also non-linear with respect to the two unknowns within the inaccessible imaging domain, the electromagnetic field and the permittivity. The Contrast Source Inversion (CSI) technique effectively linearizes the problem by casting the data-error norm in terms of contrast-source variables, which vary with the interrogating field, and regularization is performed by introducing the so-called Maxwellian regularizer which is written in terms of the contrast-sources and the contrast [79]. Much research has been performed on advancing the CSI algorithm since it was first reported, including the addition of a multiplicative regularizer [80].

For biomedical imaging applications, which are of interest in the context of the present work, the incorporation of discretized numerical inversion models into CSI that are based on either the finite-element method (FEM) or the discontinuous Galerkin method (DGM) forward solvers have provided much flexibility and several advantages for the overall inversion process [58, 59, 67]. Most importantly, these forward solvers have allowed one to incorporate prior information into the inversion model that has the effect of regularizing the inversion, enabling high-contrast re-

constructions such as are required for breast imaging [45, 81–83]. The flexibility of these partial differential equation (PDE) based solvers has also allowed advancements in data-acquisition systems utilized to acquire scattered-field data for MWI [3, 84]. Other potential advancements in MWI for breast tumor detection include the use of contrast agents [47]

Recent work in multi-frequency imaging has shown promise in increasing the spatial resolution and correspondingly, the amount of distinguishable anatomic detail in MWI reconstructions. For instance, while the use of "frequency hopping" has long been shown to be an effective means of obtaining images from high-frequency data by feeding low-frequency solutions as "initial guesses" into inversion algorithms [52], a so-called "frequency cycling" and "tissue-dependent mapping" framework has been adopted in recent studies to perform multi-frequency imaging demonstrating significant enhancement in the quality of resulting 2D images [39, 40]. In those works, an arbitrary fixed number of iterations was used as the stopping condition for the imaging algorithm, but it was noted that further exploration into more intelligent stopping criteria was justified, particularly based on the observation that running the algorithm longer than necessary could deteriorate the imaging results. In fact, to date, there has been little exploration into optimizing the conditions to which a microwave imaging algorithm should adhere when determining the appropriate point to move on from intermediate inversions to the next frequency in a multi-frequency sequence, or when to terminate reconstructions entirely.

While monitoring the convergence of data error has been the most common objective approach to halting microwave imaging algorithms, as it is often difficult to ascertain whether a chosen error limit will undershoot, overshoot, or consistently meet the attainable image reconstruction quality for a given dataset, several early stud-

ies focusing on synthetic and experimental imaging performance fell into the same habit of simply pre-assigning an arbitrary number of iterations for the algorithm to complete, chosen for convenience or through trial and error [49, 79, 85, 86].

Although there have been previous attempts to develop more intelligent stopping criteria for imaging algorithms in recent literature [81], a more thorough statistical analysis of the data error is undertaken here and employed as part of a logical multi-variable framework of stopping criteria for a frequency-cycling tissue-dependent mapping formulation of Contrast Source Inversion (CSI). For comparison purposes, some 2D imaging results from a recent study are included in this work to demonstrate the significant gains in efficiency and image quality granted through the incorporation of the described stopping criteria [40]. Reconstruction results are subjected to quantitative analysis using common image error metrics to provide an objective measurement of these improvements.

3.3 Materials and Methods

3.3.1 DGM-CSI Algorithm

An implementation of CSI using a high-order frequency-domain formulation of Maxwell's curl equations has been used for all 2D breast images presented here, employing the discontinuous Galerkin method (DGM) as a forward solver. Nodal coefficients in high-order polynomial expansions represent unknown field and contrast quantities in the resulting DGM-CSI algorithm. Independent from this choice of implementation, among the benefits of CSI is its use of operators that are functions of frequency and the material properties of the background medium only, which do not change from iteration to iteration [79]. As aforementioned, further improvement

in performance has been demonstrated through the use of a tissue-dependent mapping process and the practice of cycling back to low-frequency reconstructions [40], and a brief overview of this process is provided in Section 3.3.2. Further details specific to DGM-CSI can be found in [57, 58], but a summary of the relevant quantities and definitions involved in the CSI cost functional is included here, since it pertains to the discussion of data and domain error that follows.

The microwave imaging problem in Figure 3.1 depicts an object of interest (OI) with an unknown dielectric contrast $\chi(\vec{r})$, a function of position vector $\vec{r}$, typically defined as

$$\chi(\vec{r}) = \frac{\hat{\varepsilon}_r(\vec{r}) - \hat{\varepsilon}_b}{\hat{\varepsilon}_b}, \tag{3.1}$$

where $\hat{\varepsilon}_r$ is the complex relative permittivity and $\hat{\varepsilon}_b$ is the complex background permittivity. In breast imaging applications, the background permittivity is usually represented as the homogeneous immersion medium in which the breast is submerged and the imaging domain $\mathcal{D}$ is an area typically chosen to be contained by the outer skin layer of the breast. An array of $t = 1, 2, \ldots, T$ transmitters is used to generate probing incident fields; the resulting scattered fields are measured by an array of R receivers that make up a discrete measurement surface $\mathcal{S}$.

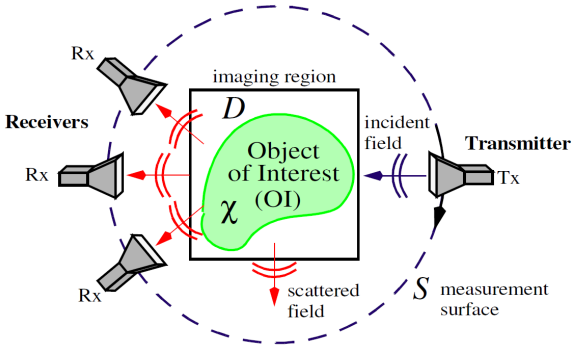

Figure 3.1: Two-dimensional representation of the imaging problem. The object of interest (OI) has an unknown contrast χ, where $\mathcal{D}$ is the imaging domain and $\mathcal{S}$ is the surface containing the transmitters (Tx) and receivers (Rx).

It is assumed that the reader is familiar with the standard CSI algorithm, and only the aspects important to the proposed stopping criteria will be reviewed. The CSI algorithm solves for the contrast $\chi(\vec{r})$ of breast tissue within $\mathcal{D}$ from this scattered field data by minimizing the following two-part cost functional:

$$\mathcal{F}^{\text{CSI}}(\chi, w_t) = \mathcal{F}^{\mathcal{S}}(w_t) + \mathcal{F}^{\mathcal{D}}(\chi, w_t), \tag{3.2}$$

where both the contrast $\chi(\vec{r})$ and the transmitter-dependent contrast sources $w_t(\vec{r}) = \chi(\vec{r})u_t^{\text{tot}}$ (a product of the contrast and the total field u_t^{tot}) are unknown and confined to the domain $\mathcal{D}$.

The first term of Equation (3.2) represents the "data error", given by

$$\mathcal{F}^{\mathcal{S}}(w_t) = \frac{\sum_t \|u_t^{\text{sct}} - \mathcal{L}_{\mathcal{S}}\{w_t\}\|_{\mathcal{S}}^2}{\sum_t \|u_t^{\text{sct}}\|_{\mathcal{S}}^2}, \tag{3.3}$$

and correspondingly, the second term represents the "domain error",

$$\mathcal{F}^{\mathcal{D}}(\chi, w_t) = \frac{\sum_t \left\|\chi u_t^{\text{inc}} - w_t + \chi\mathcal{L}_{\mathcal{D}}\{w_t\}\right\|_{\mathcal{D}}^2}{\sum_t \|\chi u_t^{\text{inc}}\|_{\mathcal{D}}^2}, \tag{3.4}$$

with $\|\cdot\|_{\mathcal{D}}$ and $\|\cdot\|_{\mathcal{S}}$ denoting the L_2 norms on $\mathcal{D}$ and $\mathcal{S}$. The measured scattered field data is represented above by u_t^{sct} at R receiver locations per transmitter t, and the incident field inside $\mathcal{D}$ is u_t^{inc}. The forward operator $\mathcal{L}_{\mathcal{S}}$ converts contrast source estimates w_t in $\mathcal{D}$ to scattered field values at R receiver points per transmitter t on the measurement surface $\mathcal{S}$; $\mathcal{L}_{\mathcal{D}}$ performs a similar function, but transforms contrast sources to scattered field values within $\mathcal{D}$. For further simplicity, the "data error" per iteration i can be defined from the numerator of Equation (3.3) as

$$\rho_t^{(i)} = d_t - \mathcal{L}_{\mathcal{S}}\{w_t^{(i)}\} \tag{3.5}$$

and correspondingly, the "domain error" from the numerator of Equation (3.4) as

$$r_t^{(i)} = \chi^{(i)} u_t^{\text{inc}} - w_t^{(i)} + \chi^{(i)} \mathcal{L}_{\mathcal{D}}\{w_t^{(i)}\}. \tag{3.6}$$

These error values, particularly the data error of Equation (3.5), are subject to analysis for evaluating convergence behaviour of DGM-CSI in this study, described in Section 3.3.3.

3.3.2 Frequency-Cycling Tissue-Dependent Mapping Technique

The well-documented dielectric properties of breast tissues lead to the observation that the geometry of the real and imaginary parts of tissues' permittivity profiles should be qualitatively similar [39, 40]. The quantitative permittivity values of different types of breast tissue also form reasonably discrete ranges that are highly correlated between real and imaginary components, making it easy to stratify these

values into expected tissue types (i.e., fat, transitional, fibroglandular, and cancer) [1]. Through a tissue-dependent mapping of the imaginary part based on geometric and quantitative reconstructions of the dielectric constant, an "artificial" imaginary component was proposed as part of the initial guess for the next frequency dataset in the imaging sequence, to good effect [39, 40].

In addition to tissue-dependent mapping, this previous work invoked "frequency cycling" as opposed to conventional frequency hopping, where frequency cycling simply continues the reconstruction process past the highest frequency in a multi-frequency sequence by returning to the lowest frequency dataset (with an initial guess based on the highest frequency solution) [40]. The initial studies using DGM-CSI have shown that this practice preserves the fine detail acquired from high-frequency data, and produces better results than a single incremental frequency-hopping sequence operating for the same total number of iterations. In a practical microwave imaging scenario without the benefit of foreknowledge of this total number of iterations, however, a potential drawback to frequency cycling would be the increased number of iterations required to produce images when arbitrary or overly-stringent stopping conditions are applied.

3.3.3 Stopping Criteria for Single-Frequency Reconstructions

As described in Section 3.3.1, iterative inversion methods such as DGM-CSI attempt to solve the inverse scattering problem by minimizing the cost functional of Equation (3.2), which includes a data error $\rho_t^{(i)}$ (Equation (3.5)) represented by the difference between the measured and computed fields on $\mathcal{S}$ for a given transmitter t. If U is the total number of data points across all receivers R and sources T, then the $U \times 1$ data-error vector $\bar{\rho}^{(i)}$ can be represented as a concatenation of every

transmitter's data errors, such that

$$\bar{\rho}^{(i)} = [\rho_1^{(i)}; \rho_2^{(i)}; \ldots; \rho_T^{(i)}] \tag{3.7}$$

After all contrast sources $w_t^{(i)}$ are updated for each transmitter t, the inversion process by convention performs a convergence check that calculates the new data-error vector $\bar{\rho}^{(i+1)}$. The goal is to reduce this new data error as much as possible, and aside from simply assigning a maximum number of iterations, one could monitor the data error until it falls below an arbitrarily-chosen tolerance level δ such that some form of a termination condition examining its sum, maximum value, or norm applies, commonly implemented as

$$\text{if}\,(\|\bar{\rho}^{(i+1)}\| < \delta)\,\text{stop.}$$

Alternatively, the difference between the normalized data-error vector at two successive iterations, $\bar{\rho}^{(i)}$ and $\bar{\rho}^{(i+1)}$, can be calculated until it falls within a prescribed tolerance to check for convergence [86].

Such conditions would seem to be reasonable criteria by which termination of the inversion algorithm should take place. However, the total data error often has little bearing on the accuracy of the resulting reconstruction, despite properly converging to a preset minimum. While liberally large values of error tolerance will logically terminate the imaging algorithm prematurely, it has also been observed that conservatively small choices of error tolerance will result in a poorer quality image. This outcome is likely due to the supposition that the minimization of a cost functional towards zero arguably means accounting for any and all error in modeling, calibration, and measurements (i.e., noise) through non-physical changes in the reconstructions. The apparent inadequacy of having the data error converge to within an arbitrary

tolerance alone served as motivation to develop a multifaceted approach to stopping criteria that improves the reconstructions of a frequency-cycling reconstruction technique through statistical analysis of data and domain error of each iteration.

This proposed framework stops the imaging algorithm based primarily on the statistical *distribution* of the contributing terms to the data-error vector $\bar{\rho}$. Referring the reader back to Equation (3.7), assuming a best-case scenario where the forward operator $\mathcal{L}_{\mathcal{S}}$ is able to perfectly model the field behaviour of the imaging system and the contrast sources w_t had been iteratively solved to the exact solution, the data error ρ_t would be reduced to the difference between the field values d_t experimentally measured at the receivers for all given transmitters and the ideal noise-free field values generated by $\mathcal{L}_{\mathcal{S}}\{w_t^{(i)}\}$. This difference would amount to the noise of the experimental system, which would presumably converge to a known pattern, such as a Gaussian distribution.

However, it is clear that even if one could acquire completely noise-free measurement data, it is not practical, or even possible, to find a numerical model that could exactly match it. This so-called modeling error, attributed to mismatches between the approximate representation of the imaging environment $\mathcal{L}_{\mathcal{S}}$ (which varies by formulation, mesh granularity, order number, etc.) and the true, unknowable functions that perfectly predict field behaviours within the system, invalidates the assumption that the remaining data-error vector $\bar{\rho}$ (upon convergence of the imaging algorithm to a solution) consists simply of noise. Modeling error is the primary reason why data calibration must be performed on experimental data, and it is not a trivial issue to address in MWI [87].

Correspondingly, since the contributions to the data error are multifactorial in nature and vary with each experimental set-up and possibly with each target, it

will not necessarily converge to a known family of statistical distributions. Use of any of the myriad of statistical normality tests available (such as the Anderson–Darling or Shapiro–Wilk test) on the data error as part of the proposed algorithmic stopping criteria would therefore be unreliable. However, the profile of the data error distribution (regardless of its final form) should reach a steady state when the algorithm has sufficiently converged to a particular solution. To confirm that this trend occurs during a reconstruction requires comparison of the current iteration's data error distribution to those of multiple previous iterations, which is accomplished in this work with an implementation of the *two-sample Kolmogorov-Smirnov* (K-S) test.

The two-sample K-S test is a non-parametric goodness-of-fit hypothesis test that evaluates the maximum absolute difference D between the cumulative distribution functions (CDF) of two sample data vectors over a range of x in each data set. Recall that the CDF (F_X) of a continuous random variable X can be expressed as the integral of its probability density function (PDF) f_x (that is, a function whose value at any given sample can be interpreted as providing a relative likelihood that the value of the random variable would be equal to that sample), such that

$$F_X(x) = \int_{-\infty}^{x} f_X(t)\,dt. \tag{3.8}$$

In the discrete case, $F_X(x)$ would be equivalent to the proportion of values in $f_X(x)$ less than or equal to a specified value of x.

Suppose the data-error vector PDFs from two consecutive iterations of the DGM-CSI imaging algorithm, $\bar{\rho}^{(i)}$ and $\bar{\rho}^{(i+1)}$, each have some observed CDF, say $\hat{P}^{(i)}(x)$ and $\hat{P}^{(i+1)}(x)$; that is, for any specified value of x, the value of $\hat{P}(x)$ is the proportion of error values less than or equal to x in the corresponding dataset. Consider the

quantity

$$D = \max_x(|\hat{P}^{(i+1)}(x) - \hat{P}^{(i)}(x)|), \tag{3.9}$$

that represents the maximum error between two CDFs. The K-S test makes use of this D value to return a probability, in the form of a scalar asymptotic p-value in the range of $[0, 1]$, which represents the likelihood that the two samples were drawn from the same distribution. More precisely, the p-value is defined as the probability of observing a test statistic (D) as extreme or more extreme than the observed value, for the null hypothesis that the data in these two vectors are from the same continuous distribution [88–91]. In the implementation of the test, the decision to reject the null hypothesis is based on comparing the returned p-value with a preset significance level (commonly 5% for many applications). The test becomes very accurate for large sample sizes, and is believed to be reasonably accurate for sample sizes U_1 and U_2, such that $(U_1 \times U_2)/(U_1 + U_2) \geq 4$, which is the case for a collection of data error values in a system of 24 transmitters and receivers operating at a single frequency (representing a total of 576 data points).

While the strength of the two-sample K-S test lies in determining when two samples are from differing distributions, the nature of the test guarantees that the smaller the value of D, the higher the returned p-value will be. This feature allows the test's p-value to be used as a numerical indicator for how likely the two samples were drawn from the same distribution (i.e., how closely their CDFs match), as opposed to its primary use in *rejecting* the null hypothesis.

Empirical studies of the real and imaginary parts of the data error of DGM-CSI reconstructions indeed revealed that the shape of the probability distribution curves fluctuate significantly with large variances in early iterations (Figure 3.2) but gradually reach a steady state in later iterations as expected, once all remarkable

subjective change in the resulting images had ceased (Figure 3.3). Since any two neighboring iterations' data error may only change slightly and be interpreted as being drawn from the same distribution by the two-sample K-S test, it was decided that a sliding window of past iterations' data errors should be examined and compared to that of the current iteration. Moreover, the threshold value that the returned p-value should surpass for any given K-S test within this sliding window needed to be high enough to similarly reject subtler variations in two iterations of data error that would otherwise pass the goodness-of-fit test. This wider breadth of analysis ensured that more gradual changes were detected so that any corresponding stopping criteria would not halt the reconstruction prematurely.

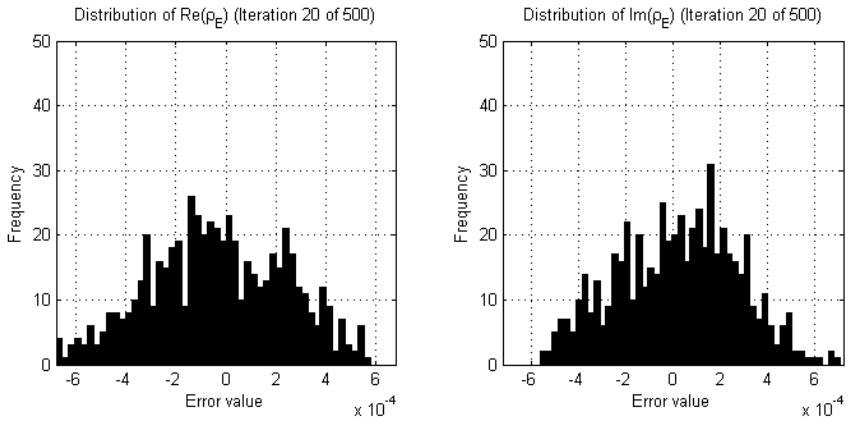

Figure 3.2: Examples of histograms demonstrating estimates of the probability distribution of the real and imaginary parts of the data error (ρ_{E}) during a DGM-CSI inversion of an arbitrary 2D synthetic breast model early in the reconstruction process (iteration 20).

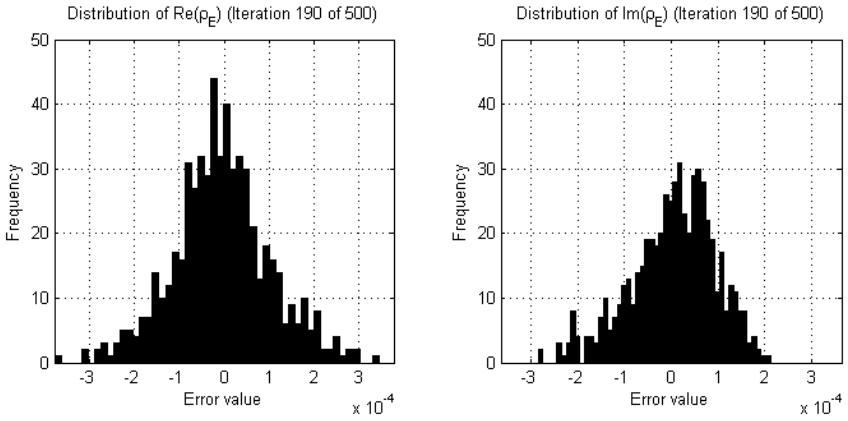

Figure 3.3: Examples of histograms demonstrating estimates of the probability distribution of the real and imaginary parts of the data error (ρ_{E}) during the same DGM-CSI inversion as Figure 3.2, later in the reconstruction process (iteration 190).

Therefore, the window size of iterations under scrutiny, the p-value threshold (assumed constant over the window), and the percentage of that window's iterations reaching or surpassing that p-value threshold, are all parameters to the stopping criteria for the algorithm based on the K-S test, which is applied separately for the real and imaginary parts of each iteration's data error. A preliminary study attempting to establish the effects of these parameters was undertaken for the frequency-cycled reconstruction of a 2D breast model, described in Section 3.4.1.

It should be noted that the statistical analysis governing the aforementioned stopping criteria only makes use of the *data* error, which may be sufficient for certain MWI algorithms (such as the distorted Born iterative method) whose minimized cost functional consists solely of a data error term. However, as shown in Section 3.3.1, CSI-based iterative inversion algorithms make use of cost functionals containing a second domain error term dealing with total field values inside the imaging domain [79, 86]. Therefore, another *ad hoc* stopping condition based on the domain error is also prudently employed in the algorithm, as described in the next subsection.

3.3.4 Global Termination of Multi-Frequency Reconstructions

The stopping conditions described in Section 3.3.3 are appropriate for halting single-frequency inversions, but multiple-frequency reconstructions have thus far not been addressed. In a frequency-hopping scenario, the stopping criteria based on K-S tests alone can be easily employed to determine when each individual inversion should terminate and move on to the next frequency, with global termination occurring following reconstruction of the highest frequency.

However, in a frequency-cycling reconstruction scheme, the cycle of reconstructions could theoretically continue *ad infinitum* without another explicit set of rules in place governing the global termination of the imaging process. A separate, secondary *ad hoc* global termination criterion was therefore implemented, based on a previous study [82]; once each frequency's dataset in the cycle is subjected to the K-S test stopping criteria at least once, if the percentage of relative change in domain error between two successive iterations falls below 0.1%, then it is deemed appropriate to globally terminate the frequency cycle and end the reconstruction. This provision could also serve as a fallback contingency in the event that the data error-based conditions turn out to be too strict to satisfy for a given individual frequency.

3.3.5 Full Description of Multi-Frequency Imaging Procedure

The key concepts involved in the proposed multi-frequency imaging procedure, while implemented herein for the DGM-CSI algorithm, can easily be applied (with minor modifications) to other iterative algorithms widely used in MWI, including Gauss-Newton Inversion (GNI) and distorted Born Iterative Method (DBIM). As such, a

descriptive approach to the technique is undertaken here in order to keep its applicability as general as possible. Taking into account the stopping criteria described throughout Section 3.3.3 and using the procedural description of the frequency-cycling reconstruction approach with tissue-dependent mapping described in [40], the new consolidated multi-frequency imaging procedure is proposed as follows:

1. The real and imaginary parts of the complex permittivity are reconstructed using the lowest frequency data available (e.g., 1.0 GHz). The termination point of this reconstruction is dictated by the results of successive two-sample K-S tests performed on both the real and imaginary parts of the data error separately, comparing the current iteration to those of a sliding window of past iterations, governed by a choice of parameters for p-value, window size, and percentage of windowed iterations reaching this p-value threshold. For robustness, a back-up termination condition may be implemented, either related to the relative change in domain error for CSI-based algorithms as described in Section 3.3.4, or a maximum number of iterations.

2. A point-by-point search through the reconstructed real part of each nodal basis coefficient in the DGM-CSI mesh (or more generally, each mesh element or pixel of the reconstructed image) classifies the type of breast tissue. This classification is based solely on the range of expected values of dielectric constant at that frequency, as outlined in [40].

3. An initial guess for the next imaging frequency (e.g., 2.0 GHz) is generated using the tissue-dependent mapping process [39,40]. It consists of the unmodified real parts of the reconstructed ε_r at the mesh nodal points, and a new imaginary part created from a simple linear interpolation of the expected range of dielectric

loss values, based on the appropriate Cole-Cole models of tissues classified in Step 2. This technique preserves the geometry of the real and imaginary parts of the solution.

4. This new initial guess for the complex permittivity is used to run the inversion algorithm at the next frequency (e.g., 2.0 GHz). As per the procedure outlined in [40], the user may choose to keep the imaginary part constant during this inversion and update only the real part to converge to a new solution. This "anchoring" process has been shown to improve overall imaging results due to the tendency of CSI-based inversion algorithms to cause significant deterioration of the imaginary part at high-frequency reconstructions. Again, the aforementioned parameterized stopping criteria would be primarily employed to determine the appropriate point to halt this reconstruction.

5. If more than two frequencies are used in the frequency hop, steps 2–4 are repeated as necessary until the reconstruction of the final frequency of the succession is complete (e.g., 3.0 GHz). This succession may include "frequency cycling"; that is, returning the inversion algorithm to the lowest frequency data and incrementally stepping through each frequency again [40].

If a simple frequency-hopping scheme is employed, the reconstruction will terminate after the highest-frequency inversion, again as decided by the parameterized stopping criteria based on K-S tests of the data error. However, if a frequency-cycling scheme is used, and if the imaginary part of the solution has been "anchored" in place following the first inversion in Step 1, there are further considerations that come into play for global termination of the imaging process, and to address concerns of full CSI optimization:

- When each available dataset in the frequency cycle has been used *at least once* to contribute to the overall image reconstruction, a global termination criterion will become active, which will monitor the relative change in the domain error between successive iterations (Section 3.3.4). If this relative change falls below 0.1% at any point, the current reconstruction is halted and the frequency cycle is broken.

- Regardless of the frequency at which the algorithm was halted by this relative domain error threshold, if the imaginary part of the solution has been continuously held constant during the frequency cycle after Step 1, one last initial guess is generated as in Step 3 and a final reconstruction is run at the lowest frequency available (e.g., 1.0 GHz) with both the real and imaginary parts allowed to converge to a solution (i.e., the imaginary part is no longer "anchored"). This final inversion is terminated by the parameterized stopping criteria *or* a relative change of domain error between successive iterations falling below 0.1%, whichever occurs first. The purpose of this final run is to demonstrate the stability of the final solution and ensure that its imaginary part, despite being originally based on the geometry and tissue properties of the real part, does indeed satisfy full CSI optimization.

3.3.6 Synthetic Breast Models

Initial testing of the described stopping criteria and comparison to fixed-iteration scenarios were carried out on synthetic transverse magnetic (TM) data collected from a two-dimensional MRI-derived BI-RADS Category C (heterogeneously dense) breast model supplied by the University of Calgary, derived from an MRI slice of a cancer

patient with a breast tumour visible at the "3 o'clock" position. To demonstrate the robustness of the technique across different breast phantoms, an additional two-dimensional MRI-derived BI-RADS Category D ("extremely dense") healthy breast model supplied by the University of Wisconsin's public database (ID: 070604PA2) was employed. Both models are depicted at three different frequencies (1.0 GHz, 2.0 GHz, and 3.0 GHz) in Figures 3.4 and 3.5, illustrating the similarities between breast tissues' dielectric permittivity at the low-gigahertz band. The values of the tissue-dependent complex permittivity in all cases were calculated for every frequency using an appropriate fitted single-pole Cole-Cole model (or equivalently, a single-pole Debye model as the exponent parameter $\alpha = 0$), and for the University of Calgary model, then subjected to random perturbations of $\pm 10\%$ [68].

Data was collected for both models in a low-loss background of $\epsilon_r = 23 - 1.13i$ with 24 transmitters and 24 receivers evenly distributed at a radius of 10 cm, employing a finite-element method (FEM) forward solver with a finely-discretized mesh independent from that used for the DGM-CSI inversion. The synthetic data was collected for open boundary conditions at 1.0 GHz, 2.0 GHz, and 3.0 GHz. To test the robustness of the stopping criteria to problems with PEC boundaries, and to better reflect the capabilities of a recent University of Manitoba imaging system prototype [4], data was collected a second time with the Category C model surrounded by a circular PEC boundary with a radius of 15 cm at a reduced bandwidth. The frequencies used for the PEC-bounded case were 1.0 GHz, 1.25 GHz, and 1.5 GHz. Uniformly-distributed noise at 5% of the maximum field magnitude was used to corrupt the E_z scattered electric field data for the Category C model, and several noise levels (3%, 5%, 7.5%, and 10%) were tested for the Category D model to evaluate the effect of noise on the stopping criteria's performance. The skin thickness and inner skin boundary both

remained unknown; the only prior information used during inversions was the outer skin boundary.

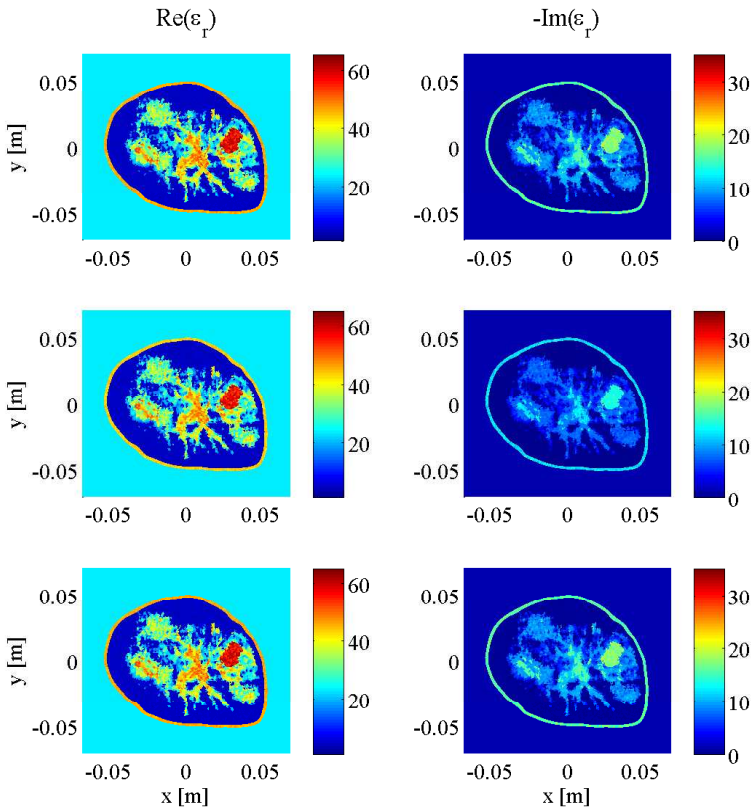

Figure 3.4: Complex dielectric properties of University of Calgary 2D synthetic breast model at 1.0 GHz (**top**), 2.0 GHz (**middle**) and 3.0 GHz (**bottom**).

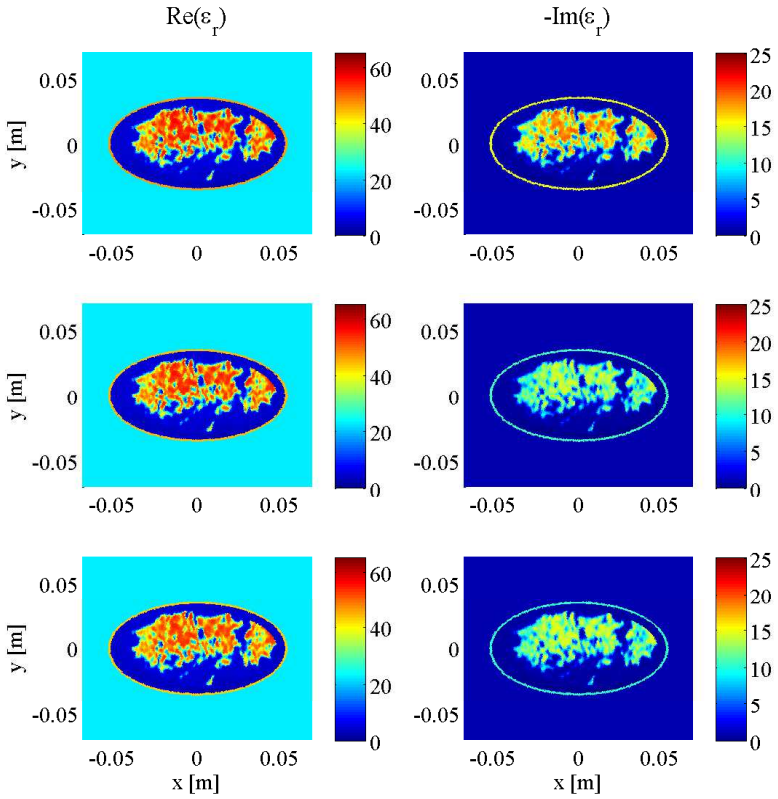

Figure 3.5: Complex dielectric properties of University of Wisconsin 2D synthetic breast model at 1.0 GHz (**top**), 2.0 GHz (**middle**) and 3.0 GHz (**bottom**).

3.3.7 Error Calculation

An objective method of evaluating the DGM-CSI algorithm's performance for differing imaging scenarios was accomplished by comparing the reconstruction results to the original Category C and Category D synthetic models of the *current* frequency being used in the reconstruction cycle, unless otherwise specified. The models and reconstructions each employed different underlying meshes, so their complex permittivity values were interpolated onto a common 250 $\times$ 250-pixel square grid (N = 62,500) that encompassed an area covering $(x_1, y_1) = (-0.07, -0.07)$ [m] to

$(x_2, y_2) = (0.07, 0.07)$ [m]. The relative error of L_1 and L_2 norms of the difference between the model (actual) complex permittivity $\hat{\varepsilon}_r^{\,\mathrm{act}}$ and the reconstructed complex permittivity $\hat{\varepsilon}_r^{\,\mathrm{rec}}$ over each pixel k were used as primitives to evaluate the performance of the imaging algorithm. For convenience, these will hereafter be referred to as the relative error norms REN_1 and REN_2, and are calculated and expressed as percentages, where

$$\begin{aligned} \mathrm{REN}_1(\hat{\varepsilon}_r^{\,\mathrm{act}}, \hat{\varepsilon}_r^{\,\mathrm{rec}}) &= \frac{\|\hat{\varepsilon}_r^{\,\mathrm{act}} - \hat{\varepsilon}_r^{\,\mathrm{rec}}\|_1}{\|\hat{\varepsilon}_r^{\,\mathrm{act}}\|_1} \times 100\% \\ &= \frac{\sum_{k=1}^{N} |\hat{\varepsilon}_r^{\,\mathrm{act}}(k) - \hat{\varepsilon}_r^{\,\mathrm{rec}}(k)|}{\sum_{k=1}^{N} |\hat{\varepsilon}_r^{\,\mathrm{act}}(k)|} \times 100\%, \end{aligned} \tag{3.10}$$

$$\begin{aligned} \mathrm{REN}_2(\hat{\varepsilon}_r^{\,\mathrm{act}}, \hat{\varepsilon}_r^{\,\mathrm{rec}}) &= \frac{\|\hat{\varepsilon}_r^{\,\mathrm{act}} - \hat{\varepsilon}_r^{\,\mathrm{rec}}\|_2}{\|\hat{\varepsilon}_r^{\,\mathrm{act}}\|_2} \times 100\% \\ &= \sqrt{\frac{\sum_{k=1}^{N} [\hat{\varepsilon}_r^{\,\mathrm{act}}(k) - \hat{\varepsilon}_r^{\,\mathrm{rec}}(k)]^2}{\sum_{k=1}^{N} [\hat{\varepsilon}_r^{\,\mathrm{act}}(k)]^2}} \times 100\%. \end{aligned} \tag{3.11}$$

The raw numerical value of the norms will be slightly reduced since the square grid covers an area *outside* of the imaging domain of the problem, which will consist of common unaltered background permittivity in both the model and reconstruction and thus represent pixels of zero error. Since the REN values serve primarily as a means of monitoring iterative trends in solution convergence and to demonstrate comparative improvement between imaging scenarios with equally-sized interpolated grids and imaging domains, the impact of this artificial error reduction is of little

significance.

3.4 Results and Discussion

3.4.1 Imaging with Open Boundaries

As mentioned in the introduction of the stopping criteria in Section 3.3.3, the approach had three variables: the p-value threshold that any given two-sample K-S test would use to conclude the two data error samples were drawn from the same distribution, the window size of past iterations' data errors compared to that of the current iteration, and the percentage of that window's iterations that would need to to reach or surpass the chosen p-value threshold in order to halt the reconstruction at the current frequency, deemed the "pass percentage". For the same Category C breast model in Figure 3.4, DGM-CSI was run in a frequency-cycled configuration using the rules described in Section 3.3.5 for every combination of p-value thresholds of 0.90, 0.95 and 0.99, window sizes of 10, 30, and 50, and pass percentages of 80%, 90%, and 100%. There were 27 simulations whose total number of iterations would vary based on the laxity or stringency of stopping criteria associated with low and high variable values respectively. Error norms (REN_1 and REN_2) for each scenario were plotted for every frequency jump (Figure 3.6), and the best variable combination (resulting in the lowest error metric magnitudes upon termination) was found to be a p-value threshold of 0.99, a window size of 30, and a pass percentage of 80%. This combination of values was subsequently used for all future simulations employing the stopping criteria. Note that in Figure 3.6 and in all subsequent plots of REN values, the x-axis' number of iterations represents the cumulative total throughout all frequency-hopping or frequency-cycling steps of the reconstruction.

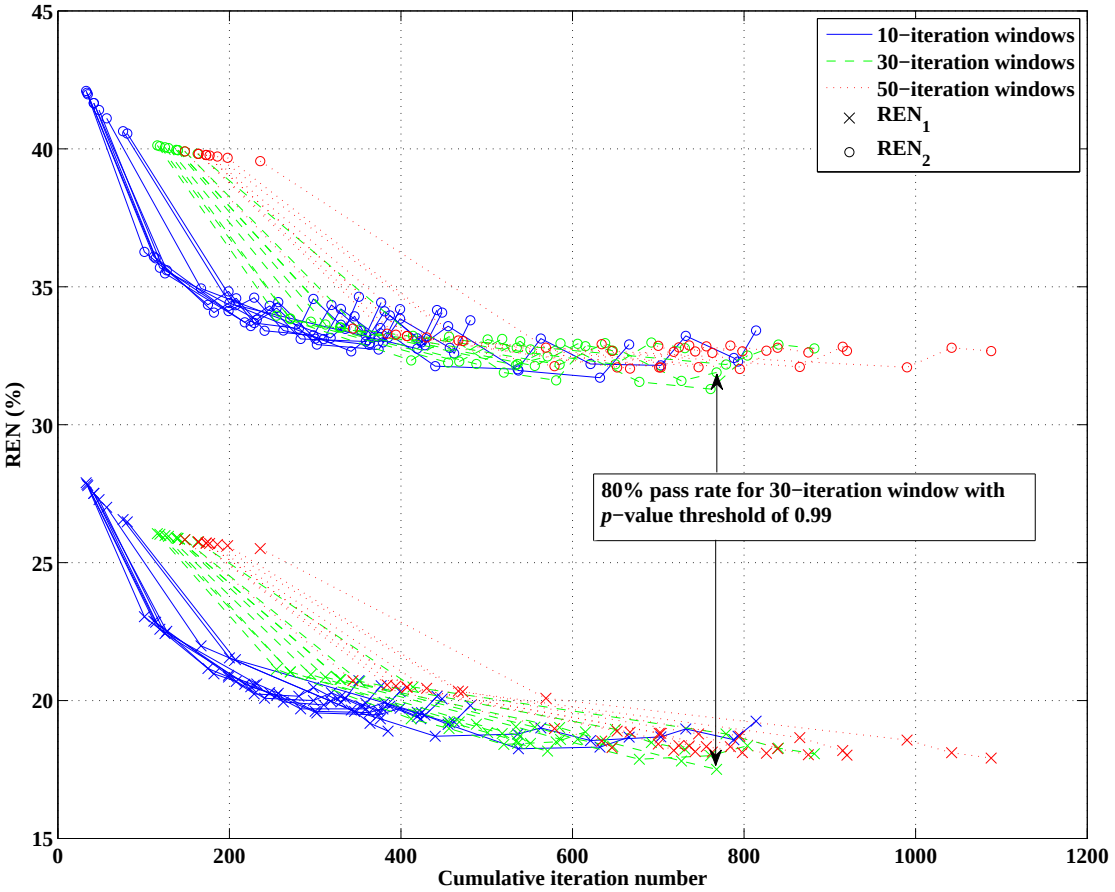

Figure 3.6: Relative error norms of open-boundary 2D DGM-CSI reconstructions across several choices of stopping criteria parameter values. Each curve in the figure corresponds to a frequency-cycled inversion for a particular choice of the three parameters (Section 3.4.1), with the window sizes coded by color for convenience. Data points on each curve correspond to REN values for the reconstructed model at each frequency change. Arrows point to the final REN values of simulations that terminated with the lowest relative error norms, indicating the best combination of parameters among those tested for this imaging scenario.

Having established an appropriate set of variables to govern the stopping criteria, a series of simulations adhering to the full description of the technique in Section 3.3.5 could be carried out to demonstrate its benefit in efficiency over conventional methods. The REN values of three scenarios (A, B, and C from Table 3.1) comparing fixed-iteration reconstructions (with and without tissue-dependent mapping) to the

use of both tissue-dependent mapping and the stopping criteria, are shown in Figure 3.7. The final imaging reconstructions of these three cases are also depicted in Figure 3.8. As the proposed stopping conditions introduce an unpredictable halt to the reconstruction cycle that could occur at any frequency and also includes a mandatory return to the lowest frequency (in this case, 1.0 GHz) for the final optimization, each REN data point may not represent consecutive frequencies of the cycle. For consistency, the REN values shown in Figure 3.7 are therefore all calculated based on the same 2.0 GHz model from Figure 3.4. For clarity, the frequency associated with each data point plotted in Figure 3.7, along with the triggering condition that caused a change in frequency or termination in the reconstruction (when relevant), is shown in Table 3.1.

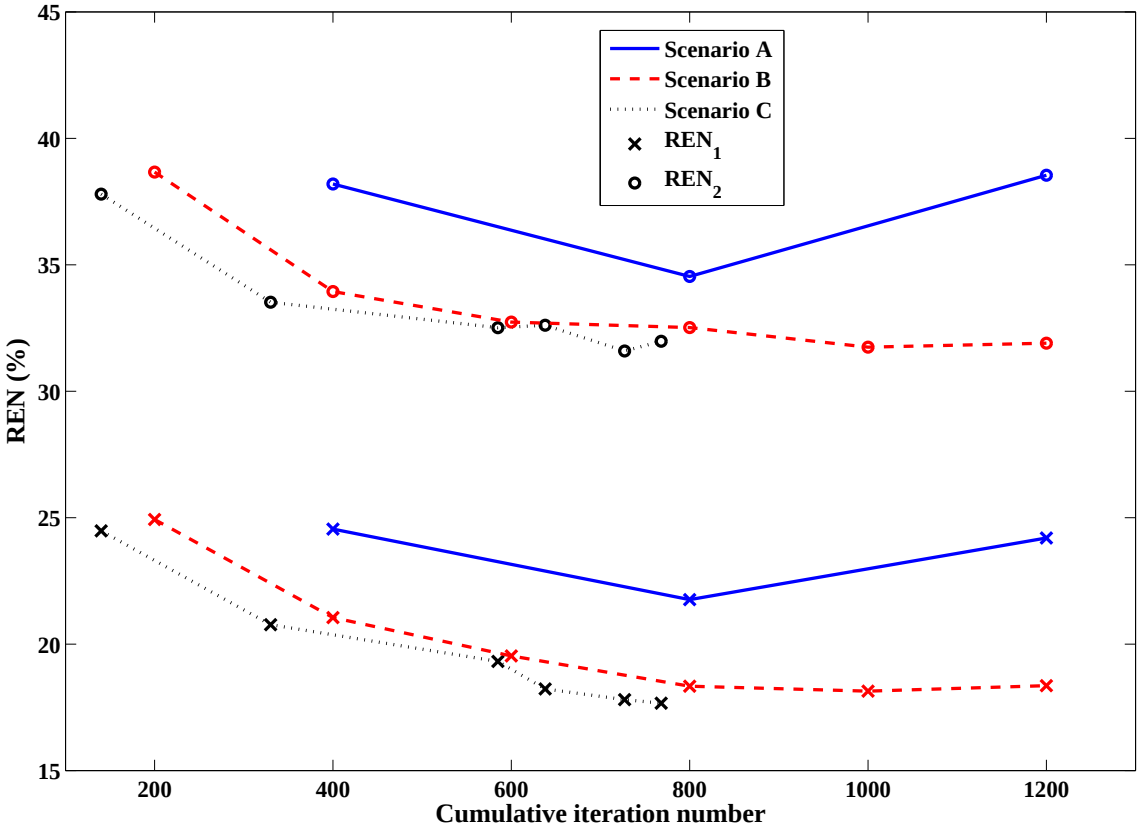

Figure 3.7: Relative error norms of frequency-hopping and frequency-cycled reconstructions: Scenario A (solid line)—without tissue-dependent mapping at 400 iterations per frequency terminating after first inversion of 3.0 GHz, Scenario B (dashed line)—with tissue-dependent mapping at 200 iterations per frequency, cycling through reconstruction frequencies once (with imaginary component "anchored" following initial 1.0 GHz inversion), Scenario C (dotted line)—with tissue-dependent mapping and stopping criteria in place, terminating after two consecutive inversions of 1.0 GHz data (one with the imaginary component "anchored" and the final run with the imaginary component freely optimized according to the guidelines of Section 3.3.5). See Table 3.1 for further details.

Table 3.1: Reconstruction progression of open boundary scenarios (Figure 3.7).

Scenario	**TM**	**SC**	**Frequency:**						**Total**
			No. of Iterations (Stopping Condition)						
			Components Reconstructed						
A	No	No	**1.0 GHz:**	**2.0 GHz:**	**3.0 GHz:**				1200
			400 (F)	400 (F)	400 (F)				
			Re, Im	*Re, Im*	*Re, Im*				
B	Yes	No	**1.0 GHz:**	**2.0 GHz:**	**3.0 GHz:**	**1.0 GHz:**	**2.0 GHz:**	**3.0 GHz:**	1200
			200 (F)	200 (F)	200 (F)	200 (F)	200 (F)	200 (F)	
			Re, Im	*Re*	*Re*	*Re*	*Re*	*Re*	
C	Yes	Yes *	**1.0 GHz:**	**2.0 GHz:**	**3.0 GHz:**	**1.0 GHz:**	**2.0 GHz:**	**1.0 GHz:**	768
			140 (KS)	190 (KS)	255 (KS)	53 (KS)	89 (DE)	41 (KS)	
			Re, Im	*Re*	*Re*	*Re*	*Re*	*Re, Im*	

TM = tissue mapping; SC = stopping criteria; F = fixed; KS = Kolmogorov-Smirnov test window; DE = Domain error; *Re* = Real part; *Im* = Imaginary part. * 80% of a 30-iteration data error window must reach or surpass a K-S test p-value threshold of 0.99.

Although DGM-CSI, like other iterative microwave imaging algorithms, performs reasonably well in recovering the real component of breast models it reconstructs, it has difficulty producing an accurate profile of the imaginary part, most notably at higher frequencies. This deficiency is illustrated from the Scenario A inversion of the Category C breast model in the top image of Figure 3.8. Subjectively, the benefit of employing the tissue-dependent mapping in the fidelity of the imaginary component is obvious in both the middle and bottom images. It has been already shown elsewhere that the described mapping technique and "anchoring" of the imaginary component at each subsequent frequency stage, along with the practice of frequency cycling, imparts a benefit to the quality of the real part of the reconstructions following the same number of iterations [39,40]. However, these other studies only tested reconstructions that used fixed numbers of iterations as termination conditions; the addition of the stopping criteria for the latter case here (Scenario C) does not appreciably degrade the quality of the final image, while reducing the total number of iterations by over 35%.

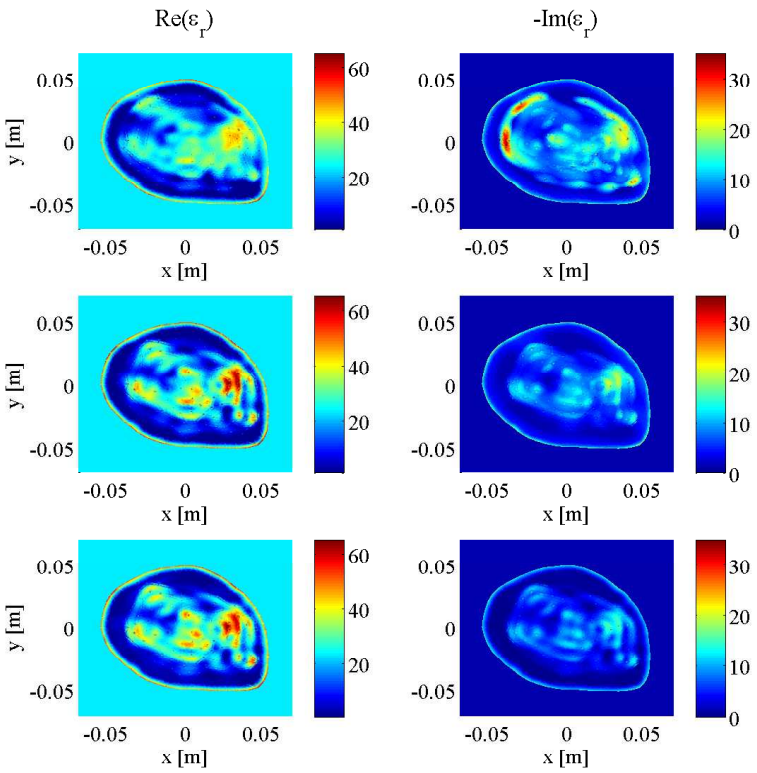

Figure 3.8: Final results of DGM-CSI frequency-hopping and frequency-cycled complex dielectric property reconstruction of synthetic breast model using 1.0–3.0 GHz data, without modification of intermediate initial guesses (Scenario A—**top**), using tissue-dependent mapping at fixed 200 iterations per frequency (Scenario B—**middle**), and employing stopping criteria and tissue-dependent mapping (Scenario C—**bottom**).

3.4.2 Imaging with PEC Boundaries

A set of simulations similar to those carried out in the previous section were performed using PEC boundaries and data from frequencies of 1.0 GHz, 1.25 GHz and 1.50 GHz, to demonstrate this method's robustness to smaller frequency bandwidths and different boundary conditions, as mentioned in Section 3.3.6. Scenarios D and E are imaging simulations recreated from an earlier study that employed fixed-iteration

reconstructions exclusively [40]; they are included in order to emphasize the benefit of adding stopping criteria in Scenario F. The imaging results are shown in Figure 3.10 with a breakdown of the reconstruction progression documented in Table 3.2. A plot of the relative error norms again similar to the open boundary cases, employing REN calculations based on the original 1.25 GHz model, is also provided in Figure 3.9.

As explained in [40], it was expected that the results would not be as impressive as open-boundary scenarios since PEC-bounded problems are generally more difficult to solve, and data was taken at lower frequencies. However, it is again clear from Figure 3.10 that there is an improvement in the recovery of the imaginary component when tissue-dependent mapping is used (middle and bottom images), more so for Scenario F. A modest improvement in the real part of ε_r for Scenarios E and F is also noted. Without the use of stopping criteria, however, Scenario E overshoots the expected values of dielectric constant in several areas. Its REN values depicted in Figure 3.9 correspondingly suffer increases relating to the fact that the reconstruction cycle has perhaps been allowed to run too long, as pointed out in [40]. The introduction of the stopping criteria has effectively prevented this degradation by terminating the reconstruction cycle close to the observed nadir of these error values from Scenario E, while once again demonstrating a sizable increase in computational efficiency by reducing the number of iterations by an impressive 66%.

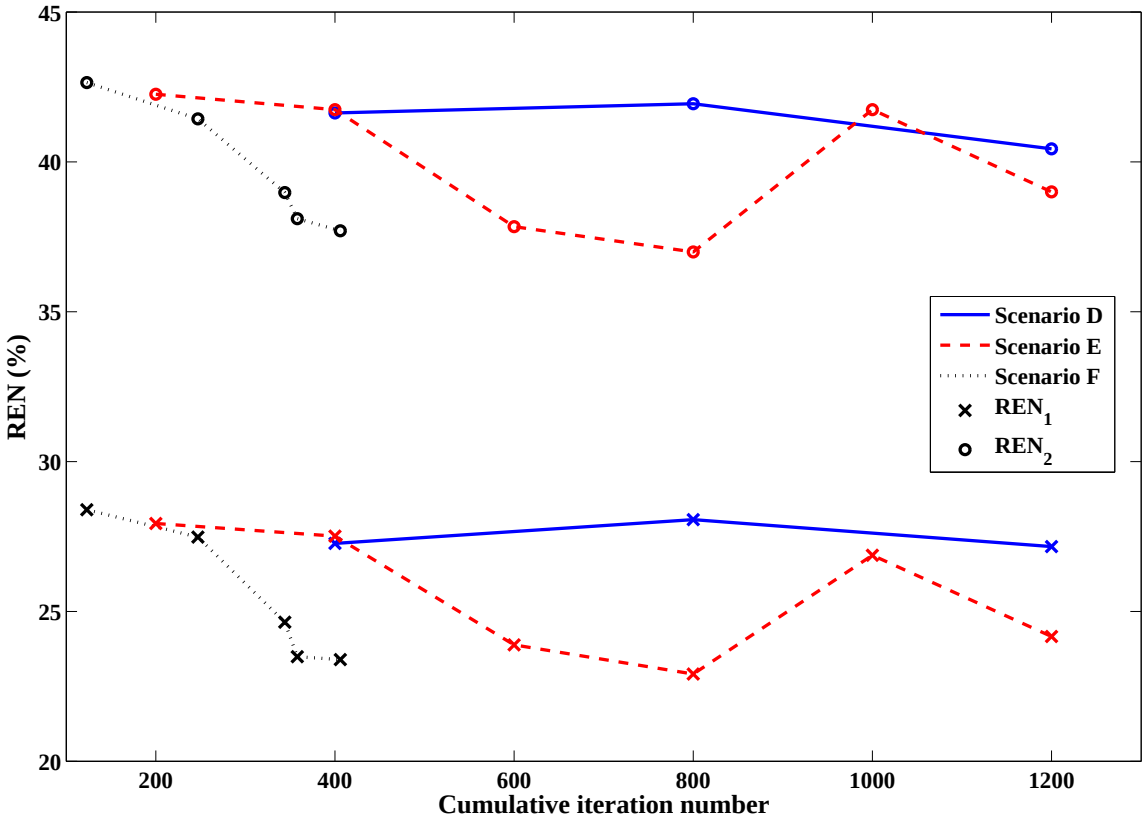

Figure 3.9: Relative error norms of reconstructions with PEC boundaries: Scenario D (solid line)—without tissue-dependent mapping at 400 iterations per frequency terminating after first inversion of 1.5 GHz data, Scenario E (dashed line)—with tissue-dependent mapping at 200 iterations per frequency, cycling through reconstruction frequencies once (with imaginary component "anchored" following initial 1.0 GHz inversion), Scenario F (dotted line)—with tissue-dependent mapping and stopping criteria in place, terminating after two consecutive inversions of 1.0 GHz data (one with the imaginary component "anchored" and the final run with the imaginary component freely optimized according to the guidelines of Section 3.3.5). See Table 3.2 for further details.

Table 3.2: Reconstruction progression of PEC-bounded scenarios (Figure 3.9).

Scenario	**TM**	**SC**	**Frequency:**						**Total**
			No. of Iterations (Stopping Condition)						
			Components Reconstructed						
			1.0 GHz:	**1.25 GHz:**	**1.5 GHz:**				
D	No	No	400 (F)	400 (F)	400 (F)				1200
			Re, Im	*Re, Im*	*Re, Im*				
			1.0 GHz:	**1.25 GHz:**	**1.5 GHz:**	**1.0 GHz:**	**1.25 GHz:**	**1.5 GHz:**	
E	Yes	No	200 (F)	200 (F)	200 (F)	200 (F)	200 (F)	200 (F)	1200
			Re, Im	*Re*	*Re*	*Re*	*Re*	*Re*	
			1.0 GHz:	**1.25 GHz:**	**1.5 GHz:**	**1.0 GHz:**	**1.0 GHz:**		
F	Yes	Yes *	123 (KS)	124 (KS)	97 (KS)	14 (DE)	48 (DE)		406
			Re, Im	*Re*	*Re*	*Re*	*Re, Im*		

TM = tissue mapping; SC = stopping criteria; F = fixed; KS = Kolmogorov-Smirnov test window; DE = Domain error; *Re* = Real part; *Im* = Imaginary part. * 80% of a 30-iteration data error window must reach or surpass a K-S test p-value threshold of 0.99.

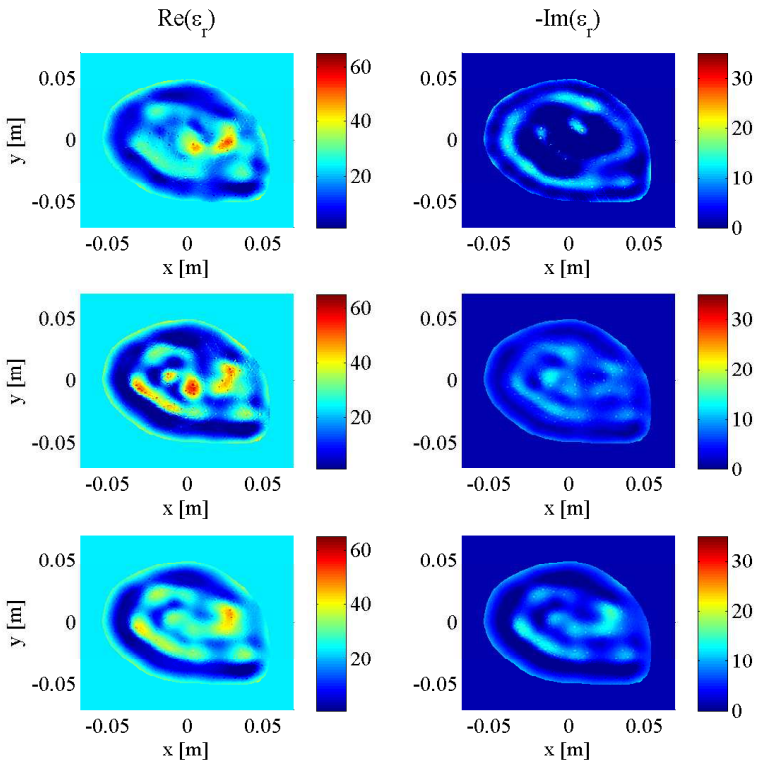

Figure 3.10: Final results of DGM-CSI frequency-hopping and frequency-cycled complex dielectric property reconstruction of PEC-bounded synthetic breast model using 1.0–1.5 GHz data, without modification of intermediate initial guesses (Scenario D—**top**), using tissue-dependent mapping at fixed 200 iterations per frequency (Scenario E—**middle**), and employing stopping criteria and tissue-dependent mapping (Scenario F—**bottom**).

3.4.3 Effect of Noise Levels

To validate that the stopping criteria developed and tested on the BI-RADS Category C 2D model would perform similarly on different breast models and be robust to varying levels of noise, another full set of simulations were carried out on the aforementioned Category D model from the University of Wisconsin database using open boundary data at 1.0 GHz, 2.0 GHz, and 3.0 GHz (Figure 3.5). The uniformly-distributed noise used to corrupt the E_z scattered electric field data was generated

at 3%, 5%, 7.5%, and 10% of the maximum field magnitude. The imaging results are shown in Figure 3.11 with a breakdown of the reconstruction progression documented in Table 3.3. A plot of the relative error norms again similar to the Category C cases, employing REN calculations based on the original 2.0 GHz Category D model, is also provided in Figure 3.12.

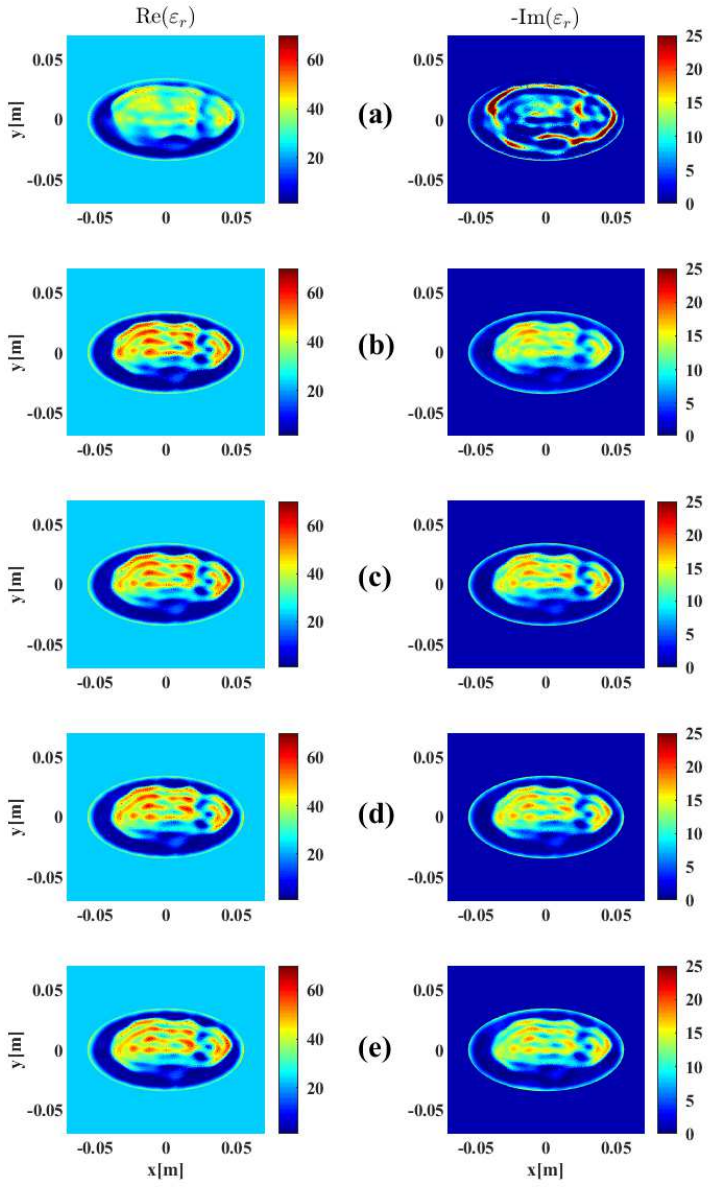

Figure 3.11: Final results of DGM-CSI frequency-hopping and frequency-cycled complex dielectric property reconstruction of open-boundary Category D synthetic breast model using 1.0–3.0 GHz data: (**a**) Scenario G—without tissue-dependent mapping at 400 iterations per frequency terminating after first inversion of 3.0 GHz (5% noise), (**b**) Scenario H—with tissue-dependent mapping and stopping criteria in place at 3% noise, (**c**) Scenario I—with tissue-dependent mapping and stopping criteria in place at 5% noise, (**d**) Scenario J—with tissue-dependent mapping and stopping criteria in place at 7.5% noise, (**e**) Scenario K—with tissue-dependent mapping and stopping criteria in place at 10% noise. See Table 3.3 for further details.

As shown in the final images of Figure 3.11, there is an obvious improvement using tissue-dependent mapping and stopping criteria over the simple frequency-hopping approach (Scenario G), especially in the imaginary part, whose geometry is not reconstructed properly and contains a large overshooting boundary artifact. However, remarkably, there is very little subjective difference in the images reconstructed from data corrupted with different levels of noise (from 3% to 10% for Scenarios H through K), with subtle changes in the real and imaginary parts visible only with careful scrutiny.

The relative error norms of all scenarios depicted in Figure 3.12 and the reconstruction break-down in Table 3.3 offer more objective measurements of the effect of noise. Specifically, lower final REN values are observed for images inverted from data containing lower noise levels, as would be expected. Also, the stopping criteria transitions frequencies and halts the entire reconstruction cycle sooner for higher noise levels. These trends are consistent for all reconstructions employing tissue-dependent mapping and stopping criteria in each level of noise used in the simulations. For instance, data containing 3% noise (Scenario H) runs longest, for a total of 759 iterations; this total is observed to gradually decrease at the 5% and 7.5% noise levels, and data containing 10% noise (Scenario K) runs for only 448 iterations.

These observations are congruous with the theory introduced in Section 3.3.3 that data containing higher magnitudes of noise would have less useful information for the optimization algorithm to extract before the distribution of data error reached a steady state (i.e., before the algorithm began to reconstruct noise) and continuing the inversion would be superfluous, or perhaps even detrimental to the final image. Overall, while these additional 2D simulations do not necessarily represent a fully comprehensive investigation across all possible breast models and imaging scenarios,

the performance of the proposed stopping criteria appears satisfactory on the Category D model, and behaves as expected on noisier datasets, even with parameter choices derived from the Category C model reconstructions.

Table 3.3: Reconstruction progression of Category D model noise-variant scenarios (Figure 3.12).

Scenario (Noise %)	**TM**	**SC**	**Frequency** :						**Total**
			No. of Iterations (Stopping Condition)						
			Components Reconstructed						
G (5%)	No	No	**1.0 GHz:**	**2.0 GHz:**	**3.0 GHz:**				1200
			400 (F)	400 (F)	400 (F)				
			Re, Im	*Re, Im*	*Re, Im*				
H (3%)	Yes	Yes *	**1.0 GHz:**	**2.0 GHz:**	**3.0 GHz:**	**1.0 GHz:**	**2.0 GHz:**	**1.0 GHz:**	759
			155 (KS)	140 (KS)	265 (KS)	50 (KS)	52 (DE)	43 (DE)	
			Re, Im	*Re*	*Re*	*Re*	*Re*	*Re, Im*	
I (5%)	Yes	Yes *	**1.0 GHz:**	**2.0 GHz:**	**3.0 GHz:**	**1.0 GHz:**	**1.0 GHz:**		586
			139 (KS)	140 (KS)	265 (KS)	34 (DE)	8 (DE)		
			Re, Im	*Re*	*Re*	*Re*	*Re, Im*		
J (7.5%)	Yes	Yes *	**1.0 GHz:**	**2.0 GHz:**	**3.0 GHz:**	**1.0 GHz:**	**1.0 GHz:**		487
			91 (KS)	112 (KS)	234 (KS)	37 (DE)	13 (DE)		
			Re, Im	*Re*	*Re*	*Re*	*Re, Im*		
K (10%)	Yes	Yes *	**1.0 GHz:**	**2.0 GHz:**	**3.0 GHz:**	**1.0 GHz:**	**1.0 GHz:**		448
			87 (KS)	90 (KS)	228 (KS)	11 (DE)	32 (DE)		
			Re, Im	*Re*	*Re*	*Re*	*Re, Im*		

TM = tissue mapping; SC = stopping criteria; F = fixed; KS = Kolmogorov-Smirnov test window; DE = Domain error; *Re* = Real part; *Im* = Imaginary part. * 80% of a 30-iteration data error window must reach or surpass a K-S test p-value threshold of 0.99.

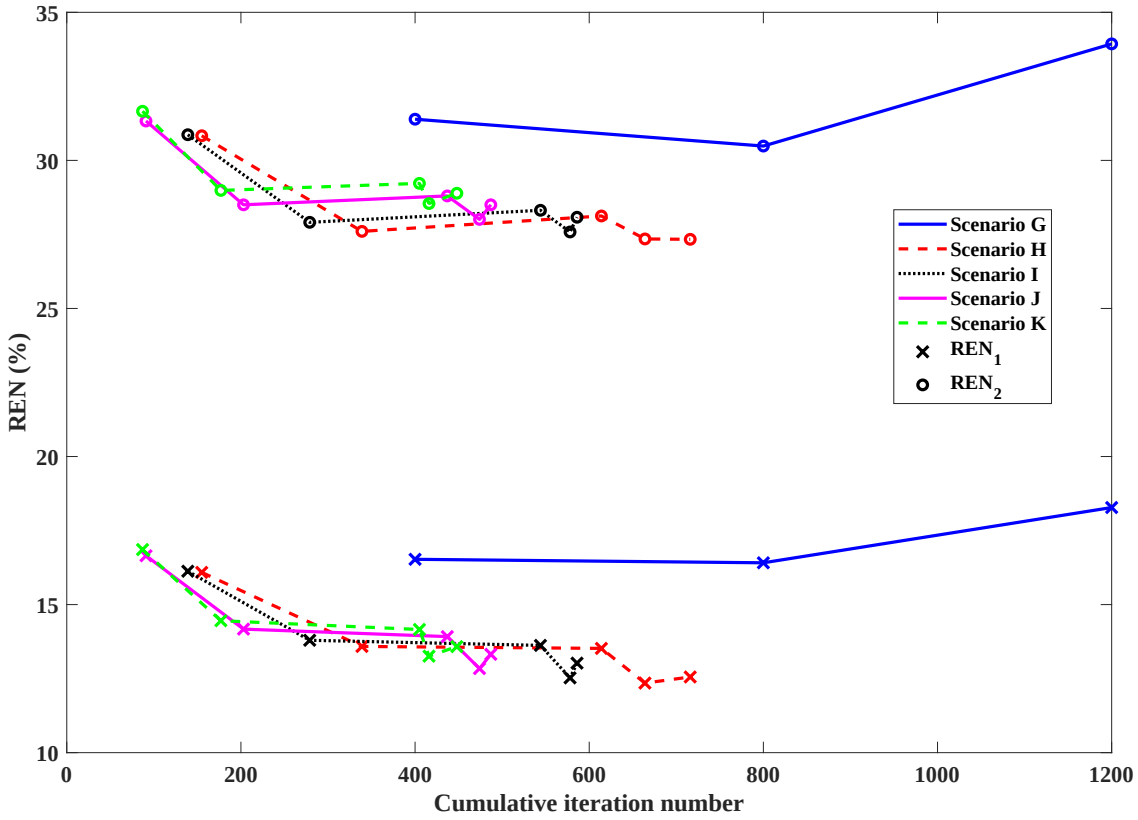

Figure 3.12: Relative error norms of frequency-hopping and frequency-cycled reconstructions of Category D model: Scenario G (blue solid line)—without tissue-dependent mapping at 400 iterations per frequency terminating after first inversion of 3.0 GHz (5% noise), Scenario H (red dashed line)—with tissue-dependent mapping and stopping criteria in place at 3% noise, Scenario I (black dotted line)—with tissue-dependent mapping and stopping criteria in place at 5% noise, Scenario J (magenta solid line)—with tissue-dependent mapping and stopping criteria in place at 7.5% noise, Scenario K (green dashed line)—with tissue-dependent mapping and stopping criteria in place at 10% noise. See Table 3.3 for further details.

3.5 Conclusions

It has been demonstrated that a stopping condition based on the similarities of the statistical distribution of data error at successive iterations has the capability of significantly speeding up the DGM-CSI algorithm while having no appreciable

detrimental effect on the final imaging results, even yielding superior solutions than fixed-iteration scenarios. This boost of efficiency is granted through novel use of sequential two-sample K-S tests on the data error to determine appropriate times to halt the imaging algorithm, truncating likely unnecessary (and in some cases counterproductive) reconstruction iterations.

Whether or not the best set of parameters used in this analysis represents the true optimal values for the stopping criteria for other breast models, or if these same values are applicable to 3D inversions, is open to debate. However, given the promising imaging results obtained from this initial set of tests, and the gains in efficiency provided through significant reduction of the number of iterations needed to converge to these solutions, it was judged appropriate to keep the best parameters from this introductory exploration of the method and leave a more comprehensive examination of parameter optimization for future investigations.

The most interesting form of the proposed multi-frequency imaging procedure employs tissue-dependent mapping and "anchoring" of the imaginary part along with the new stopping criteria. This *ad hoc* procedure also returns the reconstruction cycle to stable low-frequency data after recovering anatomical detail from higher frequencies, allowing both real and imaginary parts to properly converge before global termination. The advantages gained by this use of both tissue-dependent mapping and novel stopping criteria have also been demonstrated to be robust for different breast models, frequency bandwidths, boundary conditions, and noise levels.

In fact, the stopping criteria have a more dramatic effect on the imaging results obtained from the more complex PEC-bounded problem and data with higher noise levels, suggesting this technique may be especially useful for avoiding image degradation and reconstruction artifacts in difficult cases such as full 3D reconstructions in

semi-resonant enclosures, including experimental measurements that may be excessively noisy or contain poor frequency data unsuitable for inversion. To explore this possibility, preliminary extension of this technique to the 3D DGM-CSI algorithm developed at the University of Manitoba is a logical next step, along with parameter optimization studies of the stopping criteria for data from experimental systems.

Acknowledgments

The authors would like to thank the University of Calgary for providing the 2D Category C synthetic breast model used for the reconstructions presented in this work. This research is partially supported by the Natural Sciences and Engineering Research Council of Canada (NSERC).

4

Article 3*: Enhanced Detection of Magnetic Nanoparticles using a Novel Microwave Ferromagnetic Resonance Imaging System

4.1 Abstract

Objective: An aluminium faceted chamber designed for 3D microwave imaging (MWI) of the breast has been integrated into an electromagnet in order to carry out signal acquisition experiments for an inverse scattering-based ferromagnetic resonance imaging (FRI) system, or magnetic contrast-enhanced MWI system. *Methods:* For this proof of concept, the chamber has been equipped with four wire monopole antennas, and low-contrast oil-based targets have been tested with varying concentrations of iron oxide magnetic nanoparticles (MNP) to serve as ferromagnetic contrast agents. The electromagnet is capable of sustaining a static polarizing magnetic field (PMF) greater than 0.2 Tesla (2000 Gauss) across the imaging chamber to modulate

*Reprinted with permission from Cameron Kaye, Colin Gilmore and Joe LoVetri, "Enhanced Detection of Magnetic Nanoparticles using a Novel Microwave Ferromagnetic Resonance Imaging System," accepted for publication in *IEEE Transactions on Biomedical Engineering*, August 2020.

the MNPs' ferromagnetic response, effectively changing the targets' magnetic permeability. Differential scattered field data are then collected through the application and withdrawal of this PMF. *Results:* This study has successfully characterized a particular narrow band of frequencies within the asymmetric faceted chamber that demonstrate significant differential responses corresponding to the weak magnetic signal physically isolated from the MNPs, tested on different sizes and positions of targets containing various concentrations of MNPs. *Conclusion:* Similar to ferromagnetic resonance (FMR) spectroscopy, in which detection of FMR phenomena is best achieved at probing frequencies coinciding with the structural resonant frequency of a metallic cavity, these resonant frequencies of interest yield a high level of sensitivity to MNP permeability changes and are suitable for imaging within the chamber. *Significance:* These represent the first experimental results of a full-scale FRI system capable of detecting and eventually imaging MNPs at biologically relevant concentrations.

4.2 Introduction

Iterative optimization-based approaches to solving the electromagnetic inverse scattering problem have been established for over twenty years, with contrast source inversion (CSI) algorithms being among the most promising techniques in biomedical applications of microwave imaging (MWI), particularly for breast cancer detection and treatment monitoring [67]. Implementations of CSI based on finite-element method (FEM) forward solvers and more recently, the time-harmonic discontinuous Galerkin (DG) formulation of Maxwell's curl equations, have proven effective when modelling complicated imaging environments such as resonant chambers, and the use of FEM-CSI and DGM-CSI in many two-dimensional and three-dimensional

imaging scenarios, for dielectric and magnetic targets, has been extensively studied [48, 57–59, 92].

While conventional MWI continues to advance towards clinical application as a low-cost complementary imaging tool, a competitive need to improve the modality's limited spatial and contrast resolution has steered research towards microwave contrast media. Such contrast enhancement is a relatively new extension to the field, and since changes in relative permeability (μ_r) have been largely ignored for biomedical applications due to the intrinsically non-magnetic environment of the human body, most of the studies that have been carried out have focused primarily on agents that modify the relative permittivity (ε_r) of the targeted tissues [26, 27, 47]. However, recent exploration of magnetic contrast-enhanced imaging and "theranostic" uses of the technology, such as microwave hyperthermia treatment of tumours, has introduced novel contrast agents like magnetic nanoparticles (MNPs) to artificially accentuate the complex magnetic properties of the cancerous regions in which they accumulate [93–95].

One group has made significant progress in advancing magnetic contrast-enhanced MWI through the use of a static or sinusoidal polarizing magnetic field (PMF) to modulate the magnetic response of the weakly scattering MNPs, isolating it from the much stronger electrical response of lossy biological tissue [2]. They have shown, through inversions of synthetic data based on the truncated singular value decomposition (TSVD) scheme and through experimental assessment of MNP-laden *ex vivo* porcine tissue, that the detection of these targeted induced magnetic anomalies is possible within otherwise purely dielectric biological tissues [28, 95, 96]. Our DGM-CSI algorithm supports quantitative inversion of electrical and magnetic properties simultaneously, and can take full advantage of PMF-mediated physical isolation of the

MNPs' weak magnetic signal through the use of a two-stage imaging procedure [37]. However, it has not yet been tested on experimental data, since an imaging system capable of generating differential signals from magnetic contrast-enhanced regions had not heretofore been developed.

This work describes the implementation and preliminary testing of a microwave ferromagnetic resonance imaging (FRI) system, coined as such since it combines the fundamental concept of ferromagnetic resonance (FMR) spectroscopy with the core elements of magnetic contrast-enhancement and 3D MWI within resonant cavities. FMR spectroscopy is a powerful experimental technique used to probe the magnetic properties of ferromagnetic materials, and has been studied extensively for decades in physics and material science [97–99]. Its basic set-up consists of an electromagnet and a microwave resonant cavity tuned to a specific resonant frequency, with a detector monitoring the microwave absorption within the system; the ferromagnetic sample is placed in the cavity and exposed to an external DC magnetic field sweeping through a range of field strengths. When the magnetization precession frequency of the sample (shifted by the external field) matches cavity's natural resonant frequency, a strong absorption is detected.

In this study, an air-based quasi-resonant flat-faceted chamber serves as the imaging platform and resonant cavity, equipped for these preliminary tests with four simple wire monopole antennas as transmitters and receivers, which elicit complex resonance modes within the imaging domain [3, 4]. It has been lowered into the bore of a large electromagnet capable of producing a DC magnetic field strong enough to accomplish the aforementioned physical isolation of weak magnetic signals consistently across the imaging domain. The electromagnet is activated at various field strengths, and the S-parameters are collected from pairs of antennas and analyzed for changes in mag-

nitude associated with shifts in the MNPs' ferromagnetic resonance frequencies and thus the complex magnetic permeability. Unlike the simple metallic waveguides often used in FMR spectroscopy, the complex structure of the asymmetric faceted chamber allows for differing active resonance modes at different frequencies and loading conditions, thus providing potentially several bands of resonant frequencies suitable for imaging.

This paper is organized as follows: Section 4.3 describes the theory behind modelling the magnetic properties of the iron oxide MNPs used as the ferromagnetic material within the system, and subsequent experimental confirmation of these properties. Section 4.4 introduces the experimental apparatus, including the capabilities and specifications of the custom-made electromagnet, and outlines the procedure to obtain signals from the system along with the characteristics of the targets and their positions. Section 4.5 details the results of trials on several target compositions, sizes, and concentrations of MNPs; the interpretation and discussion of these results is covered in Section 4.6.

4.3 Magnetic Response of MNPs at Microwave Frequencies

4.3.1 Model of Complex Magnetic Susceptibility

In order to properly understand the physical phenomena at play when acquiring data from dielectric targets containing embedded clusters of MNPs, a realistic estimate of the expected quantitative values of complex relative permeability ($\hat{\mu}_r$) or equivalently, the complex magnetic susceptibility ($\hat{\chi}_\mu = \hat{\mu}_r - 1 = \chi'_\mu + i\chi''_\mu$)

should be determined. These values can be predicted by mathematical models that describe the MNPs' behaviour when suspended in a carrier fluid, which appropriately represents the environment of the magnetic material employed in our experiments.

Each single-domain, magnetically anisotropic MNP is subject to a permanent magnetic dipole $\mathbf{m}$ that aligns spontaneously along an energetically favourable direction within the particle referred to as its *easy magnetization axis* [100]. This axis reacts to the exposure of a time-harmonic electromagnetic field of angular frequency ω according to three different physical phenomena: Brownian relaxation, Néel relaxation, and ferromagnetic resonance. The details of these mechanisms' individual influences are left to the references [2, 100, 101], but their combined effect on the overall frequency-dependent magnetic response of a colloidal suspension of MNPs (a "ferrofluid") can be adequately described by the complex quantities of longitudinal susceptibility ($\chi_{\mu\parallel}$) and transverse susceptibility ($\chi_{\mu\perp}$) such that:

$$\hat{\chi}_{\mu}(\omega) = \frac{\big(\chi_{\mu\parallel}(\omega) + 2\chi_{\mu\perp}(\omega)\big)}{3}. \tag{4.1}$$

The low-frequency contribution (in the hundreds of megahertz range) is attributed to Brownian and Néel relaxation, expressed simultaneously by an effective relaxation time τ_{eff} and modelled as a Debye-like dispersion

$$\chi_{\mu\parallel}(\omega) = \frac{\chi_{\mu\parallel 0}}{1 + i\omega\tau_{\text{eff}}} \tag{4.2}$$

where $\chi_{\mu\parallel 0}$ is the MNP- and concentration-dependent static parallel susceptibility [100]. At gigahertz-range frequencies, the transverse susceptibility predominates and is governed primarily by ferromagnetic resonance, which is well characterized by the

equation originally proposed by Landau and Lifshitz [102]:

$$\chi_{\mu\perp}(\omega) = \chi_{\mu\perp 0}\frac{\omega_0^2(1+\alpha^2) + i\omega\omega_0\alpha}{\omega_0^2(1+\alpha^2) - \omega^2 + i2\omega\omega_0\alpha}. \tag{4.3}$$

The damping coefficient α, the static traverse susceptibility $\chi_{\mu\perp 0}$, and the ferromagnetic resonance frequency ω_0 of the MNPs are all material-dependent, but the latter two properties can be influenced by the application of an external magnetic field H_{PMF}. The value of ω_0, also referred to as the resonance frequency of the Larmor precession, specifically follows the relationship:

$$\omega_0 = \gamma(H_a + H_{\text{PMF}}), \tag{4.4}$$

where γ is the gyromagnetic ratio and H_a is the anisotropy field given by $H_a = 2K_a/(\mu_0 M_s)$, with μ_0 being the permeability of free space, K_a defined as the MNP-dependent anisotropy constant, and M_s the saturation magnetization of the MNP core. Values of properties for polymer-coated magnetite (Fe_3O_4) MNPs shown in Table 4.1 were either provided by the manufacturer (Ferrotec® product EMG1300) or estimated from the literature for similar MNPs. Again, we refer the reader to [2] for a more complete description of these properties' relationships to the quantities shown in (4.1)–(4.3). The modelled complex magnetic susceptibility of a ferrofluid containing a 20 mg/ml concentration of the MNPs of Table 4.1, assuming a 60% iron oxide content by weight (per manufacturer) suspended in a proprietary hydrocarbon-based fluid (Ferrotec® product EMG900 solvent) is shown in Figure 4.1 across a frequency range of 0.5–4.5 GHz for three cases: in the absence of a magnetic field, with a PMF of $H_{\text{PMF}} = 100\ \text{kA}\cdot\text{m}^{-1}$ or $H_{\text{PMF}} \approx 1250\text{G}$, and finally a PMF of $H_{\text{PMF}} = 160\ \text{kA}\cdot\text{m}^{-1}$ or $H_{\text{PMF}} \approx 2000\text{G}$ (solid, dashed and dotted lines respectively).

Table 4.1: Physical properties of magnetite nanoparticles

Mean diameter	10 nm
Saturation magnetization	$M_s = 400\ \mathrm{kA \cdot m^{-1}}$
Anisotropy field	$H_a = 39.79\ \mathrm{kA \cdot m^{-1}}$
Gyromagnetic ratio	$\gamma = 2.23 \times 10^5\ \mathrm{m \cdot A^{-1} \cdot s^{-1}}$

Although there are further modifications to (4.2) and (4.3) described elsewhere that fully account for the addition of PMF dependency [103], it is adequate to note that the application of a PMF both attenuates the resonance signal and shifts its peak to a higher frequency (outside of the observable range if sufficiently strong), effectively reducing the overall magnetic susceptibility of the ferrofluid to a weaker residual constant at our 2-3 GHz range of interest (see dashed and dotted trends in Figure 4.1). This "quenching" phenomenon increases with greater PMF magnitude; it is this effect that motivates research on imaging of differential data using MNPs [2, 28, 37, 94–96]. In this case, at an imaging frequency of 2.15 GHz chosen based on experimental observations described later, with the PMF "off", the magnetic susceptibility for 10 nm-diameter MNPs is expected to be $\hat{\chi}_\mu^{\text{off}} = -0.00277 - i0.0104$. While our electromagnet is capable of sustaining a static B-field of 2000 Gauss ($H_{\text{PMF}} \approx 160\ \mathrm{kA \cdot m^{-1}}$), to simplify later experimental validation, and given the minimal change in expected differential magnetic signal, we adopted a weaker applied PMF ("on" state) of 1250 Gauss ($H_{\text{PMF}} \approx 100\ \mathrm{kA \cdot m^{-1}}$), yielding a theoretical change in the magnetic response of the ferrofluid at 2.15 GHz of $\Delta\hat{\chi}_{\mu,\,\text{sim}}^{\text{on-off}} \approx 0.0183 + i0.00562$ or $|\Delta\hat{\chi}_{\mu,\,\text{exp}}^{\text{on-off}}| \approx 0.019$.

4.3.2 Experimental Measurement of Complex Magnetic Susceptibility

To confirm that the synthesized magnetic nanoparticles exhibit behaviour similar to the model of Figure 4.1, a sample of ferrofluid composed of the magnetite nanoparticles with the characteristics of Table 4.1 was prepared in the aforementioned hydrocarbon-based carrier fluid (Ferrotec® product EMG900 solvent) and injected into a measurement cell created with two mated N-type non-magnetic adapters (Figure 4.2).

The experimental procedure was carried out in much the same capacity as outlined in [2], though as the adapters used were commercial products and not custom-made, two adjacent holes needed to be drilled in close proximity through the outer shielding of the female-to-female N-type adapter into the air cavity formed by mating to the male adapter, to allow filling and for air to escape; the custom-made measurement cell in [2] had sufficient room to allow the air and filling holes to be on opposite ends of the cavity.

The S-parameters were measured from 0.5–4.5 GHz using an Agilent E5071C ENA for the ferrofluid-filled cavity placed within the bore of the electromagnet, and collected without any applied magnetic field, and with a steadily increasing PMF at increments of 50 Gauss until a maximum strength of 2000 Gauss was reached. These measurements were processed according to the procedure outlined in [2], ultimately based on treating the cavity formed by the N-type adapters mathematically as an annular disk of dielectric material within a transmission line, as in [104]. The measured experimental magnetic susceptibility of the 20 mg/ml concentration of ferrofluid is depicted in Figure 4.3 for an absent magnetic field (solid lines) and a PMF of 1250 Gauss.

The cables and connectors surrounding the cavity were not completely composed of non-ferromagnetic material, and given that the measurements of magnetic permeability were based on a maximum field strength of 2000 Gauss, the results were subject to residual magnetic susceptibility that required compensation. Furthermore, the manufactured nanoparticles are polydisperse; that is, while their nominal diameter was 10 nm, their true composition is comprised of a normal distribution of sizes from 4 nm to 17 nm. As such, it was not expected that the experimental magnetic permeability would necessarily reproduce as clean a representation of the resonance curve as the monodisperse model of Figure 4.1. The experiment nonetheless confirmed the superparamagnetic nature of the iron oxide nanoparticles and demonstrated a ferromagnetic resonance curve that yielded an expected change in the magnetic response of the ferrofluid between 0 and 1250 Gauss of $\Delta\hat{\chi}_{\mu,\,\mathrm{exp}}^{\text{on-off}} \approx 0.0193 + i0.0091$ or $|\Delta\hat{\chi}_{\mu,\,\mathrm{exp}}^{\text{on-off}}| \approx 0.021$ at 2.15 GHz, which compares favorably with the model.

4.4 Description of Experimental Imaging System and Targets

Having established the expected magnetic permeability for a given concentration of MNPs, we could approach experimental measurement of these properties within a realistic imaging environment. However, design choices for several components of this system and its targets needed to be established before experiments could be undertaken.

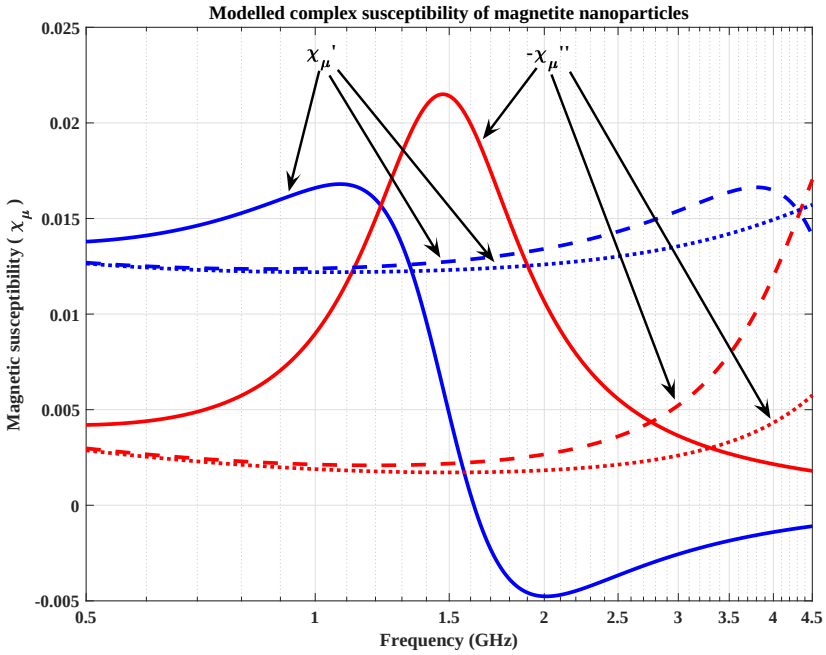

Figure 4.1: Theoretical broadband response of the magnetic susceptibility ($\hat{\chi}_\mu = \chi'_\mu - i\chi''_\mu$) for 10 nm-diameter magnetite MNPs suspended in a oil-based solvent, modelled for three cases: when a PMF is absent (solid lines), and when a PMF of magnitude $H_{\mathrm{PMF}} = 100\ \mathrm{kA \cdot m^{-1}}$ or $H_{\mathrm{PMF}} = 160\ \mathrm{kA \cdot m^{-1}}$ are present (dashed and dotted lines respectively).

4.4.1 Faceted Resonant Chamber

The hemispherical faceted chamber used in this work is described in [3, 4, 84] and its design presented several advantages over simpler chamber geometries, including reduced modeling error and introducing mixed resonant modes that could result in more useable inversion frequencies. It was milled out of a block of solid aluminium, and its unique asymmetrical design is comprised of 44 flat pentagonal or hexagonal facets, each with mounting holes drilled into them for placement of antennas or probes (see Figure 4.4).

The configuration of this imaging chamber went through several iterations in order to investigate its behaviour when testing MNP-enhanced targets within the

Figure 4.2: Measurement cell composed of a straight female-to-male N-type adapter (left, Pasternack® product 'PE91040') mated to a female-to-female N-type adapter (right, Pasternack® product 'PE91140'), with two holes visible in the body of the latter to allow for proper filling. The bodies, center conductors and plating of the adapters all consist of non-ferromagnetic material.

bore of the electromagnet. There were a few important design considerations that ultimately guided the choice of transmitter/receiver and boundaries of the imaging system, described in the following subsections.

4.4.2 Antenna Design

The frequency range of interest expected to produce the highest magnetic susceptibility contrast from the iron oxide MNPs, according to the theoretical and experimental studies of Section 4.3, was in the 1.5–2.5 GHz range; any antennas employed would need to operate well at these frequencies, especially since the differential magnetic signal could be on the order of -100 dB, depending on MNP concentration and target composition [95]. The original H-field-sensitive coplanar half-loop probes developed for the faceted chamber, introduced in [4], were primarily designed to operate at 1.0–1.5 GHz and were not sufficiently sensitive at frequencies above this limit to

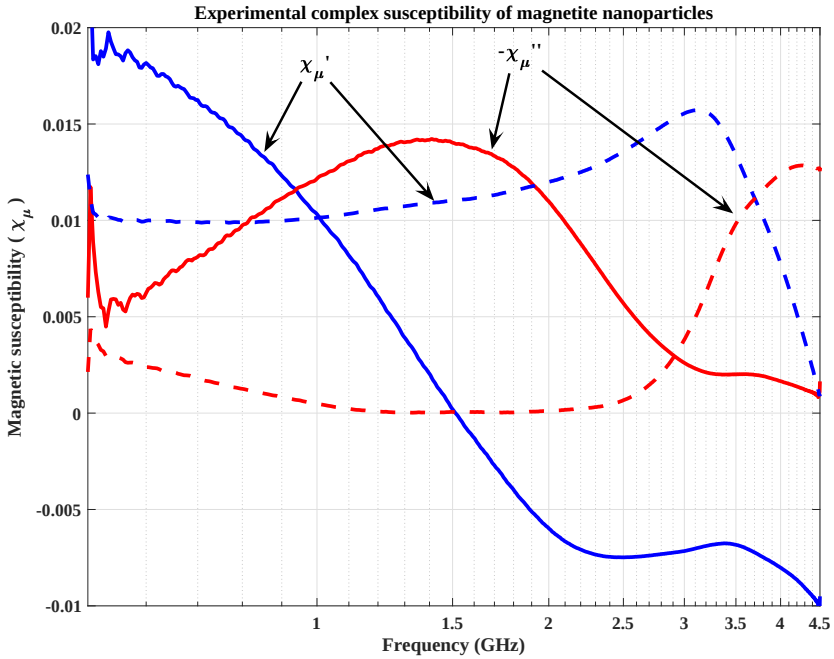

Figure 4.3: Experimental broadband response of the magnetic susceptibility ($\hat{\chi}_\mu = \chi'_\mu - i\chi''_\mu$) for 10 nm-diameter magnetite MNPs suspended in a oil-based solvent, derived according to the procedure outlined in [2] from measurements taken with a PMF of $H_{\text{PMF = 'ON'}} = 160$ kA $\cdot$ m^{-1} representing the 'ON' state, and the 'OFF' state represented by data with a PMF absent (solid lines) and a PMF of $H_{\text{PMF = 'OFF'}} = 100$ kA $\cdot$ m^{-1} (dashed lines).

be of use in this application without redesign.

As there were many unknowns in terms of how the choice of probes, targets, and their respective locations would interact with the faceted chamber's natural resonant modes, ease of customization for quick investigation of several frequency bands was another consideration for the antennas. A suitable design was found to be simple wire monopoles, as they can be readily shortened, lengthened, and manipulated as needed. These were made from unplated copper center conductors of semi-rigid cable plugged into the center jacks of bare SMA female bulkhead connectors, screwed into place through the faceted chamber's mounting holes. In this work, different lengths of copper monopoles were tested, in straight and helically-wound configurations.

These wire monopoles had sufficiently broad bandwidth in the frequency ranges of interest and are sensitive to the normal component of the electric field along the metallic facet in which they are installed. The use of monopoles and half-loop antennas has been previously investigated in [69, 70], where detailed analyses of the suitability of measuring fields within a quasi-resonant chamber are described.

4.4.3 Antenna Placement

The positioning of the wire monopoles within the chamber for the measurements reported herein is shown in Figure 4.5, in which four antennas are placed approximately equidistant in a tetrahedron-like distribution. While there are 88 mounting holes in the faceted chamber, providing over two million potential combinations of four-antenna arrays, it was found that a roughly triangular placement of three monopoles (labelled "Antenna 1–3"), surrounding the chamber's center on approximately the same horizontal plane, with the fourth monopole placed on the chamber's bottom pentagonal facet ("Antenna 4"), provided a variety of field polarity measurements with respect to the target area in the center, while maintaining adequate spacing of the antennas to minimize the potential effects of mutual coupling. The remaining unused mounting holes were covered with copper tape shielding to prevent signal leakage.

The wire monopole along the chamber's bottom ("Antenna 4") initially presented a challenge in its original vertical orientation, since the signal measured between it and the other three antennas was very low in magnitude at the 2.0–2.3 GHz range, and its vertical extent threatened to encroach upon the 3D printed plastic shell (described in Section 4.4.6) housing the targets at the chamber's center. To increase the clearance between the plastic outer shell and the bottom antenna, its distal 1.5 cm length was

bent 90° (parallel to the surface of its pentagonal facet) forming an "L" shape, which also significantly boosted the magnitude of the recorded transmission between its counterparts, owing largely to the change in polarization of the electric field being measured by the horizontal portion of the wire element in this orientation.

While not providing sufficient data for imaging purposes, this four-antenna layout allowed measurement of a diverse range of interrogation energy distributions within the chamber and an adequate number of field receiver points for the purposes of this preliminary study. The data could also easily be acquired using a four-port network analyzer (Agilent E5071C) available at the Electromagnetic Imaging Laboratory (EIL). Of course, for a full imaging experiment, all potential transmitter-receiver points would need to be populated, and the EIL has a suitable switch-matrix available that will be employed to collect this data in future studies.

4.4.4 Chamber Boundary

A final experimental detail of the system that needed to be addressed was the faceted chamber's top boundary condition, specifically whether an open top surrounded with insulating foam would be used ("open") versus a flat metal plate with a sufficiently large opening to allow the insertion of targets ("closed"). The former configuration, constituting a semi-resonant enclosure, was found to produce simple patterns of wideband S-parameters that were weak in magnitude; these signals were correspondingly more vulnerable to environmental noise, despite the use of insulating foam shielding, so this layout proved to be insufficiently sensitive at the frequency range of interest to detect the weak magnetic signal from the tested targets. The latter "closed" set-up, however, consisting of an aluminium plate (containing a 10 cm-diameter centered circular opening) affixed over the top of the faceted chamber (see

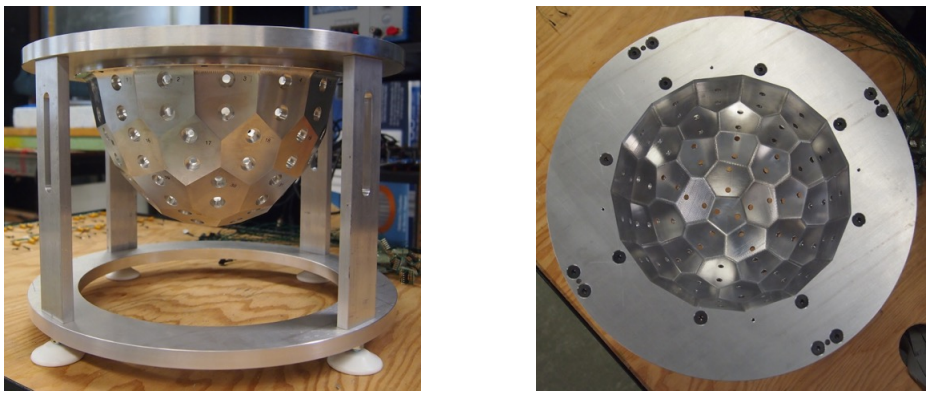

(a) (b)

Figure 4.4: Original frame of empty aluminium faceted chamber, reproduced from [3] with permission from the authors. (a) Side and (b) Top view.

Figure 4.6), represented a nearly fully resonant enclosure; the resulting wideband S-parameter responses were more complex due to the excitation of several mixed resonant modes, were much stronger in magnitude and less susceptible to environmental noise owing to the shielding of the metallic boundary.

This "closed" configuration provided a quasi-resonant environment with sufficient resonant field modes to allow the discovery of corresponding field distributions that would be exquisitely sensitive to changes in the magnetic properties of the particular MNP-infused targets being tested. This quasi-resonant enclosure is analogous to the aforementioned metallic microwave cavities used in FMR studies.

4.4.5 Custom-made Electromagnet

A custom external electromagnet was developed (by 151 Research Inc) specifically for the purpose of performing the aforementioned ferromagnetic resonance imaging (FRI) experiments. The electromagnet represents a critical component of the imaging procedure, producing the magnetic susceptibility contrast required by the imaging

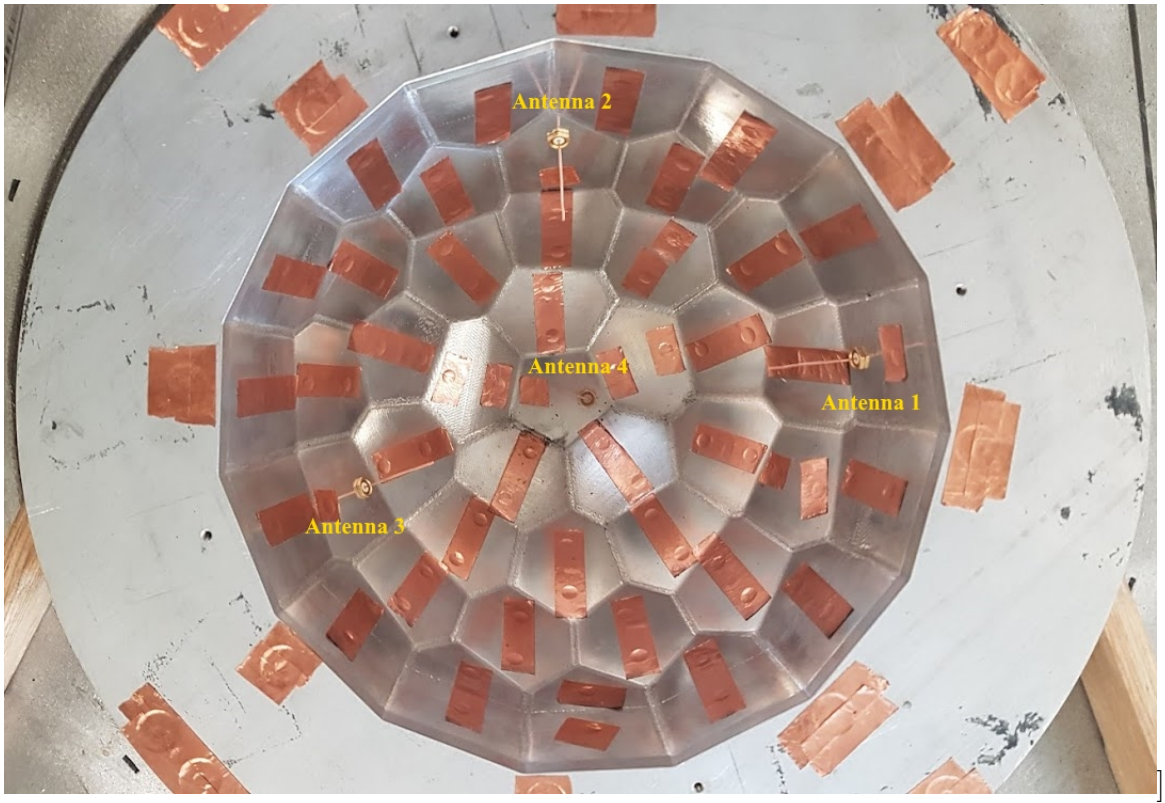

Figure 4.5: Top view of this study's experimental set-up of the faceted chamber, with four simple copper wire monopoles (labelled Antenna 1 through 4) inserted into exposed female SMA jacks, in turn connected to the four-port Agilent E5071C ENA via 3–4 m cables, at a safe distance from the magnet bore. The unused mounting holes have been covered in copper tape shielding.

(a) (b) (c)

Figure 4.6: Top view of the faceted chamber in the "closed" configuration, with an aluminium plate affixed to the superior boundary. (a) The centered circular 10 cm-diameter opening is visible to accommodate shell and target placement. (b) The plastic shell inserted into the aluminium top plate, with the styrofoam platform along its bottom showing a vacant centered position. (c) Another styrofoam platform accommodating a spherical inclusion with a radial offset of 2.0 cm (towards "Antenna 2").

algorithm. In order to isolate this weak microwave scattered-field response from the much stronger dielectric response, these magnetic fields must be applied and withdrawn in short periods of time (*i.e.* on the order of seconds), without moving the imaging target.

A photograph and schematic of the electromagnet is shown in Figures 4.7–4.8. To avoid perturbing the magnetic field, the frame of the magnet is made of non-magnetic materials: aluminium, wood, and brass screws. Temperature and magnetic fields are monitored by an on-board Arduino microprocessor and embedded temperature and magnetic field sensors. The magnet has an air-filled cylindrical bore with a diameter of 43 cm and a height of 24 cm, capable of housing the microwave breast imaging faceted chamber described in the previous section. Within the bore, the electromagnet is capable of creating a minimum DC magnetic field of 2160 Gauss, with a peak magnetic field of 2920 Gauss inside the imaging region containing the

Figure 4.7: Photo of custom electromagnet designed and constructed by 151 Research Inc. The bore's width and height are 43 cm and 24 cm, respectively.

microwave breast imaging chamber.

Starting from room temperature (around 20 °C), the electromagnet is capable of running at full strength for approximately 10 minutes while remaining below 50 °C (which has been selected as a maximum operating temperature). The magnet is driven by a DC power supply (Magna-Power TSA500-40) that is capable of a maximum 40 A of current and 500 V. The electromagnet has a DC resistance of 8.3 ohms at room temperature, rising to 9.5 ohms at the maximum operating temperature. The power supply can thus maintain a current of 40 A (or peak magnetic field of 2920 Gauss) throughout the operating temperature range.

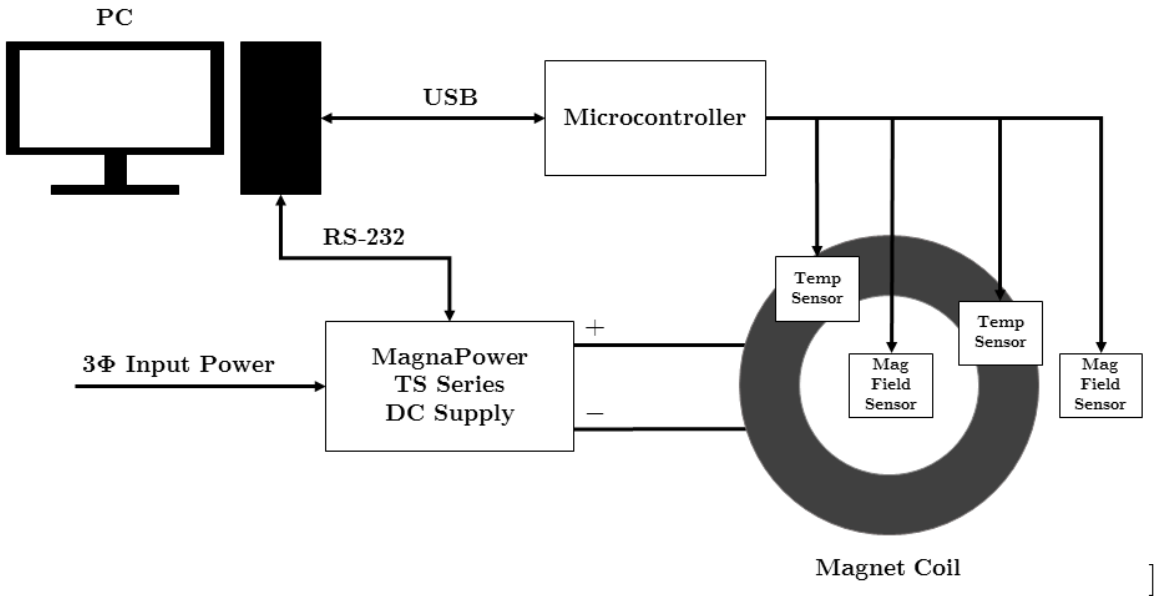

Figure 4.8: Schematic of electromagnet's control system and peripheral sensors (3Φ = three-phase alternating current, DC = direct current).

4.4.6 Target Descriptions

The external phantom consisted of a 3D printed plastic shell 10 cm in diameter, similar to that used in [3], which was left as an air-filled cavity serving mainly to house and support placement of spherical inclusions (see Figure 4.10). These inclusions were thin plastic-walled balls of three different diameters (35 mm, 38 mm and 40 mm) filled with the aforementioned proprietary hydrocarbon-based solvent (Ferrotec® product EMG900 solvent) described in Section 4.3, with various concentrations of iron oxide nanoparticles. The polymer-coated MNPs (Ferrotec® product EMG1300) used in this experiment were designed to form stable suspensions in this oil. The fluid itself has low conductivity and a relatively flat frequency-dependent dielectric permittivity (Figure 4.9), making it a low-contrast target for these initial tests with respect to the surrounding air cavity within the plastic shell and air background of the chamber. Note that these spherical inclusions are large in diameter and are not representative

of breast tumours; they are intended to serve as preliminary MNP-enhanced objects of interest for this proof-of-concept study. The use of these simple targets essentially produced a quasi-homogeneous environment in terms of relative permittivity, with the inclusion containing the MNPs constituting the strongest scatterer within the imaging region. The ferrofluid concentrations used – 0 mg/ml, 10 mg/ml, 20 mg/ml, and 50 mg/ml – were similar to those used in earlier investigations of MNP-enhanced MWI targets [2, 28, 96]. In terms of breast imaging applications, the lowest concentration of 10 mg/ml is perhaps along the upper limit of what can conceivably be delivered to breast tumours by active targeting [95, 105]. However, as mentioned, in this preliminary work these figures were not chosen to test biologically-achievable phantoms as opposed to providing a guaranteed useful signal above the noise level of the employed measurement apparatus, and thus definitively demonstrate the capacity to elicit the desired physical ferromagnetic resonance effects in a new large-scale imaging environment.

Each spherical inclusion was placed on a fitted styrofoam hemisphere seated flush with the bottom hemispherical boundary of the outer plastic shell with a portion of its flat top carved out to accommodate consistent secure placement of the inclusions, elevating the center of the sphere roughly 5 cm in the z-plane from the shell's bottom (Figure 4.10). Two different styrofoam supports were made to carry out signal acquisition tests in two different positions in x-y plane: once with the spherical target exactly centered, and once with the target radially offset by 2.0 cm approximately towards "Antenna 2", shown in Figure 4.6, (b) and (c). In addition to the three sizes of solvent-filled plastic balls, containing either no MNPs or the three other aforementioned concentrations, another target consisting of a 38 mm-diameter aluminium ball was also employed as a control (Figure 4.11) to ensure that the signals expected to

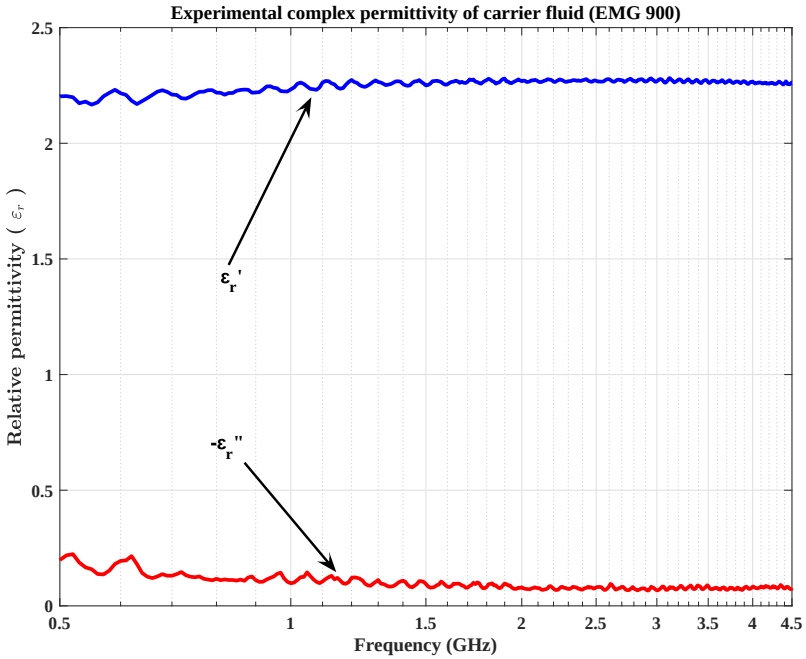

Figure 4.9: Experimental broadband complex relative permittivity ($\varepsilon_r = \varepsilon_r' - i\varepsilon_r''$) of the hydrocarbon-based carrier fluid (Ferrotec® product EMG900 solvent) used to create the ferrofluid targets used in the signal acquisition tests.

arise from the physical ferromagnetic properties of the superparamagnetic nanoparticles (described in Section 4.3) would not occur with a solid non-ferrous metallic sphere.

4.4.7 Final Experimental Procedure

For the signal acquisition tests, the top of the faceted chamber containing the four wire monopoles was covered by the aluminium plate, the 10 cm-diameter circular opening of which was centered over the chamber in the horizontal plane and taped in place. The plastic shell, itself having a 10 cm diameter and designed to fit within the circular gap of the aluminium plate, was lowered into place (containing the styrofoam base with the desired spherical inclusion at one of two positions); the 3D printing of

Figure 4.10: Two styrofoam hemispheres are pictured, with manually-carved hollow hemispherical cavities of approximately 38 mm in diameter to provide two target positions (centered, and a radial offset of roughly 2 cm) for spherical inclusions, to be placed inside the blue 3D printed plastic shell (right) with a 10 cm diameter.

Figure 4.11: The aluminium sphere (left) was used as a non-magnetic metallic control (38 mm diameter) and the thin plastic-walled balls of three different diameters (35 mm, 38 mm and 40 mm, from right to left) pictured with electrical tape covering their filling holes. A syringe was used to pierce the plastic wall of the spheres and inject either pure carrier fluid or various concentrations of ferrofluid, as required.

the shell included a narrow lip along its superior boundary that secured it in place to the aluminium plate, suspending it within the approximate center of the chamber.

The faceted chamber itself was then lowered into the bore of the electromagnet on wooden supports, centered in the horizontal plane with the inferior boundary of the chamber descended roughly 10 cm within the bore, and taped in place. Before beginning data acquisition, a gaussmeter was placed at the surface of the styrofoam platform within the plastic shell (representing the approximate position of the center of the spherical targets) with its probe oriented to measure magnetic fields along the z-axis, and the amounts of current required to obtain magnetic field strengths from 50 G to 2000 G in 50-Gauss increments were recorded.

The four-port Agilent E5071C ENA used as a signal source was then connected to four 3–4 m SMA cables subjected to a full four-port SOLT calibration. These cables were then fastened to the four SMA bulkhead connectors housing the four monopoles for the experiments detailed in the next section. It should be noted that these cables and the SMA female-to-female bulkhead connectors were not fully non-magnetic, and could therefore contribute to the experimental error of the system. Finally, since the 10 cm-diameter open top of the plastic shell represented another source of signal leakage or external interference, a large piece of insulating foam was placed over this opening after the placement of every target, to minimize the potential influence of environmental noise.

4.5 Experimental Results

The first signal acquisition trial employed 7.5 cm lengths of copper conductor (representing quarter-λ monopoles at 1.0 GHz in air), with the distal 3 cm ends of each probe wound into a helical coil to shorten the distance each element would

span medially toward the chamber's center, in order to avoid contact with the thin plastic shell used to house the magnetic targets. A relatively wide frequency range was initially scanned, from 0.5 GHz to 2.5 GHz, to investigate the complicated wide-band behaviour of the resonant enclosure and empirically identify narrower ranges or even discrete frequencies of interest potentially representative of natural resonant frequencies of the chamber in its "closed" configuration.

A sample of the magnitudes of measured S-parameters within an empty chamber are shown in Figure 4.12. Analysis of these results showed a peculiar sharp resonant feature at 2.15 GHz that was consistently present in all 16 S-parameters, despite a few preliminary empirical trials that involved moving the helically-wound monopoles to different positions and polarizations. It was surmised that this frequency represented a resonant-type response contributed primarily by the air-filled quasi-resonant chamber.

Signals were then measured with the magnetic field off and again at a strength of 2000 Gauss for the empty chamber, and two 38 mm-diameter centered spherical targets, one containing only the hydrocarbon-based carrier fluid and the other a 50 mg/ml concentration of MNPs. The results of the relative change in magnitude for these three states are shown for the same sample of S-parameters in Figure 4.13, demonstrating an obvious strong differential response for the target containing ferromagnetic material at the frequency of interest, 2.15 GHz.

This observation prompted a second trial with 3.5 cm lengths of copper conductor (representing quarter-λ monopoles at 2.14 GHz in air), and narrowing the frequency range in order to more closely analyze the responses for a wider range of targets. Selected S-parameter measurements for this narrower band of frequencies are shown in Figure 4.14. The shorter antennas proved capable of directing more energy into the chamber at this frequency range, and a resonant feature at 2.15 GHz (albeit

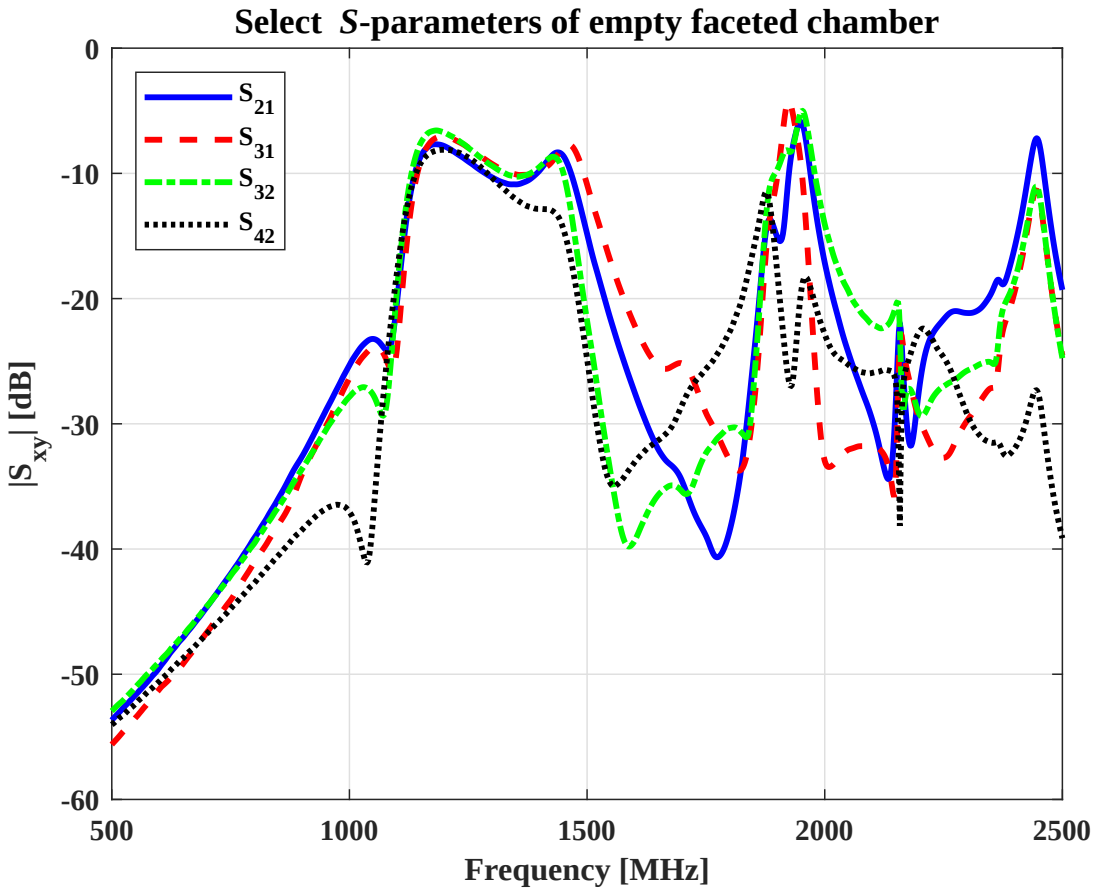

Figure 4.12: Magnitudes of selected S-parameters measured from 0.5–2.5 GHz in the empty faceted chamber using 7.5 cm helically-wound wire monopoles. The peaks seen in the plots correspond to resonances attributable to the chamber as well as the antennas.

more subtle) remained present in all S-parameters. Given that such a feature would not be expected in antenna resonant responses, especially with simple monopoles, this confirmed that this frequency was exciting a resonant mode attributable to the chamber geometry and not the choice of antennas.

Individual measurements of all 16 S-parameters were then carried out from 2.0–2.3 GHz for every target described in Section 4.4 in two positions, recorded for multiple PMF strengths, varying from 0 G to 2000 G in 50-Gauss increments. Results of

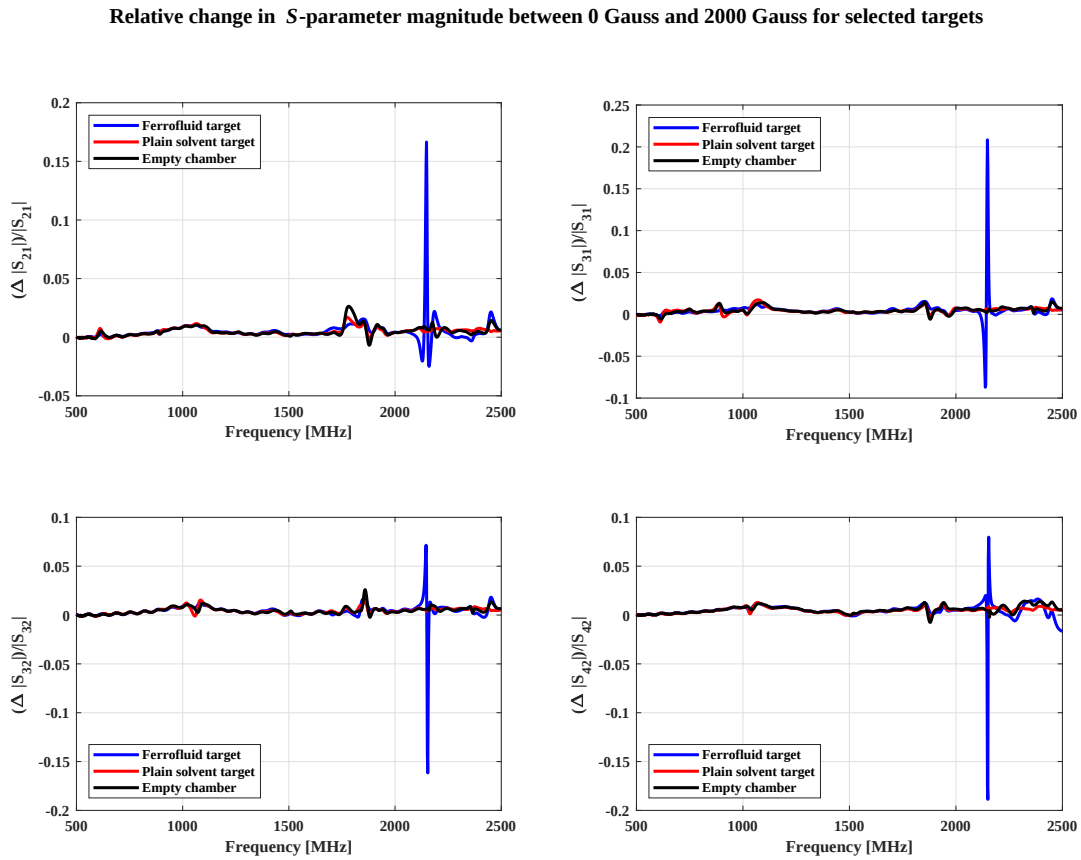

Figure 4.13: Relative change in S-parameter magnitude between two magnetic field strengths of 0 G ($H_{\mathrm{PMF}} = 0$ kA $\cdot$ m^{-1}) and 2000 G ($H_{\mathrm{PMF}} \approx 160$ kA $\cdot$ m^{-1}) measured from 0.5 GHz–2.5 GHz with 7.5 cm helical wire monopoles for three states: 1) an empty chamber, 2) housing a 38 mm-diameter spherical inclusion containing only the hydrocarbon-based solvent or carrier fluid, and 3) housing a 38 mm-diameter spherical inclusion containing a ferrofluid (50 mg/ml concentration of iron oxide MNPs). Note the strong signal obtained at approximately 2.15 GHz for the ferrofluid-containing target.

the differential signal,

$$|\Delta S_{xy}| = 20 \cdot log(|S_{xy}^{H_{\mathrm{PMF}}=H_1} - S_{xy}^{H_{\mathrm{PMF}}=0}|,$$
$$H_1 = 50, 100, \ldots, 2000\ [G] \tag{4.5}$$

for a selection of targets for $S_{xy} = S_{21}, S_{42}$ in the center position are shown in Fig-

ures 4.15–4.16, re-demonstrating the strong magnetic signal around 2.15 GHz for the ferrofluid target. An additional area of potentially useful response is also revealed along a wider portion of the frequency sweep (at approximately 2.2–2.25 GHz), strongest across PMF strengths spanning 250 G to 1000 G, that is not seen in an empty chamber or with non-magnetic targets. A cross-section of the trend at 2.152 GHz for a single S-parameter is shown in Figure 4.17 for the ferrofluid target at various concentrations versus a pure carrier fluid control. The experimental noise floor, without the systemic influence of the PMF, was also added to the plot for reference, as the average difference between 10 consecutive VNA measurements of the empty chamber with the electromagnet turned off (0 G). One also notes that the curves in the signal magnitude roughly flatten out beyond PMF strengths of around 1250 Gauss. Based on this observation of the raw S-parameter data, and in part on the minimal expected benefit in increased $|\Delta\hat{\chi}^{\text{on-off}}_{\mu,\,\text{exp}}|$ by continuing beyond $H_{\text{PMF = 'OFF'}} = 100\ \text{kA} \cdot \text{m}^{-1}$ or 1250 G (as observed in Figure 4.3), it was decided to perform follow-up experiments using our "ON" condition only as high as 1250 G as opposed to a 2000 G (or higher). This cap on the PMF strength also had the added benefit of reducing the required current to the electromagnet and thus significantly increasing its run-time for experimentation before reaching the self-imposed 50 °C temperature limit.

The second set of experiments, therefore, was carried out for all targets and positions for PMF strengths of 0 G and 1250 G only, with 10 measurements averaged for each field strength. The results of the differences in linear magnitude to preserve the sign of the differential signal between "ON" and "OFF" states (that is, $\Delta|S^{\text{on-off}}_{xy}| = |S^{\text{on}}_{xy}| - |S^{\text{off}}_{xy}|$) for a selection of S-parameters across different concentrations of MNPs for a single inclusion size of 38 mm are shown in Figure 4.18, and

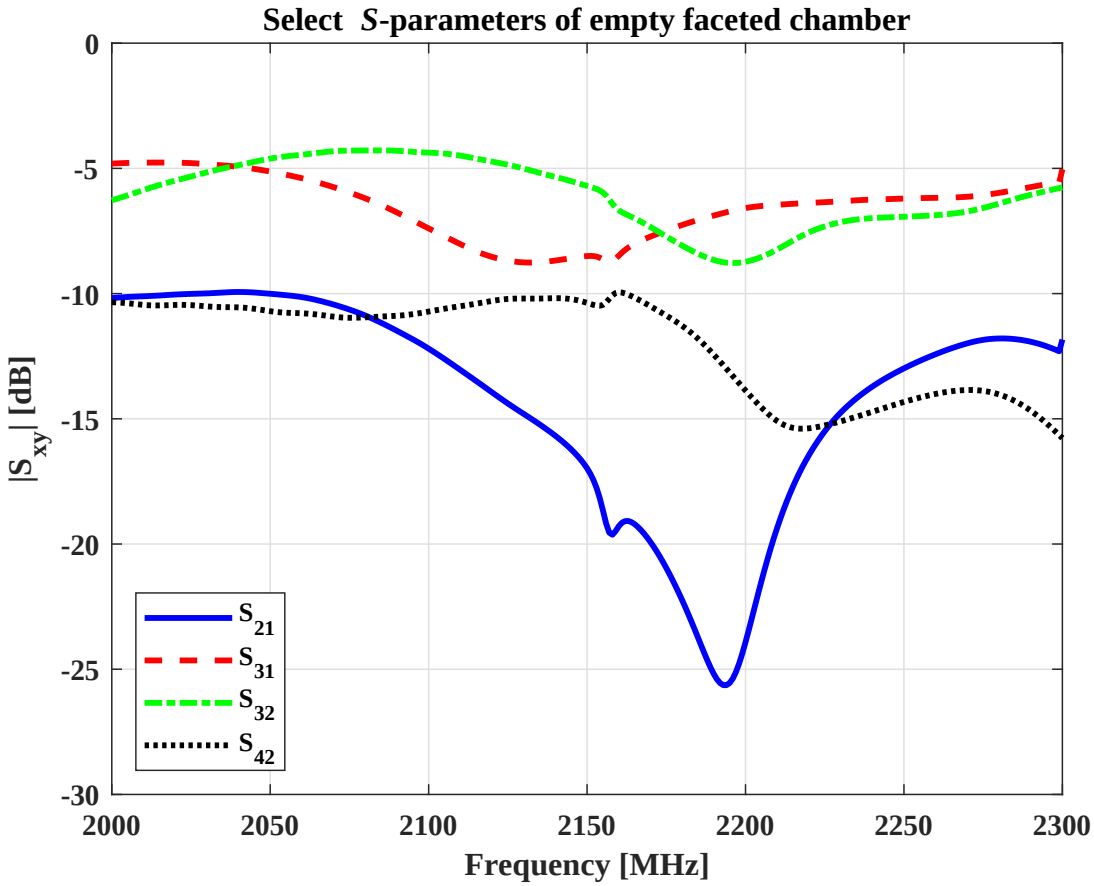

Figure 4.14: Magnitudes of selected S-parameters measured from 2.0–2.3 GHz in the empty faceted chamber using 3.5 cm wire monopoles. Note the more subtle discontinuities at 2.15 GHz for all magnitude plots.

for multiple sizes of inclusion at a single concentration of 50 mg/ml in Figure 4.19, with error bars. An additional plot depicting the difference in signal magnitudes with target position (centered versus the 2 cm radial offset) is shown for a single inclusion size of 38 mm in Figure 4.20.

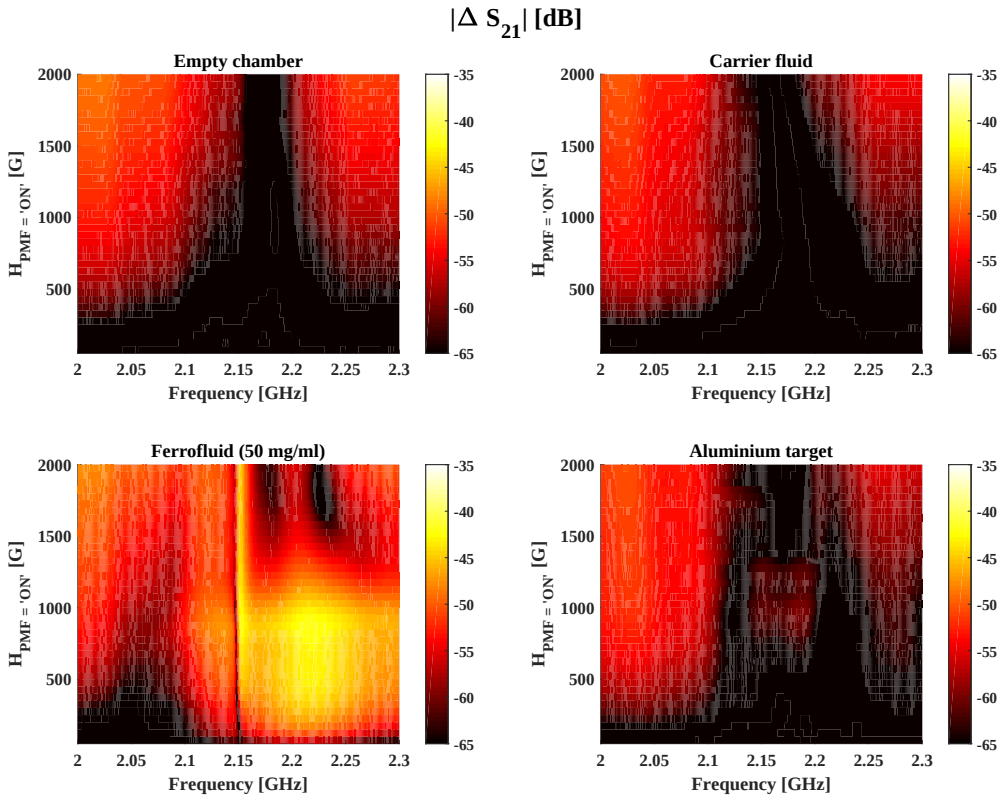

Figure 4.15: Magnitudes of ΔS_{21} plotted for strengths of $H_{\text{PMF = 'ON'}}$ varying from 50 G to 2000 G compared to $H_{\text{PMF = 'OFF'}} = 0\ G$, measured from 2.0–2.3 GHz, for an empty faceted chamber (top left) and for three different centered 38 mm-diameter targets: containing pure carrier fluid (top right), 50 mg/ml ferrofluid (bottom left), or solid aluminium (bottom right).

4.6 Discussion

It is clear through observation of the behaviour of the differential S-parameter magnitudes for various targets within the faceted chamber that for the ferrofluid spherical inclusions, the desired ferromagnetic resonance phenomenon is providing a measurable response within the examined 2.0–2.3 GHz band, particularly at the aforementioned sensitive resonant frequency around 2.15 GHz. The reader may note that there is a gradual change of magnitude measured with increasing PMF strength

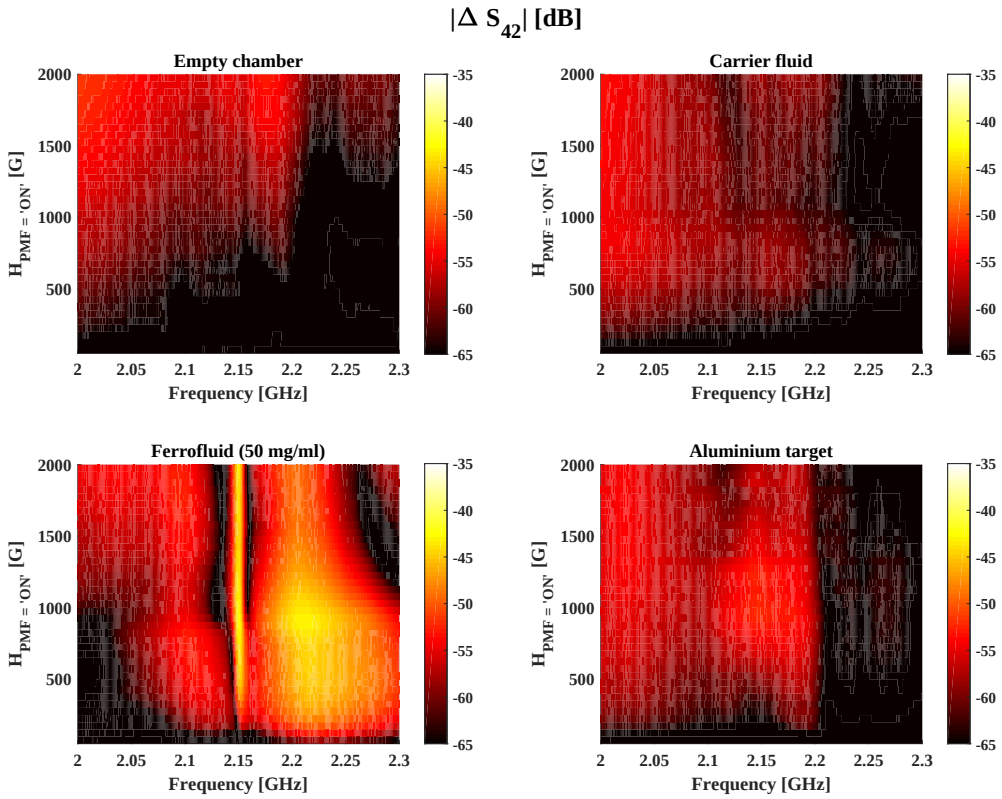

Figure 4.16: Magnitudes of ΔS_{42} plotted for strengths of $H_{\text{PMF = 'ON'}}$ varying from 50 G to 2000 G compared to $H_{\text{PMF = 'OFF'}} = 0\ G$, measured from 2.0–2.3 GHz, for an empty faceted chamber (top left) and for three different centered 38 mm-diameter targets: containing pure carrier fluid (top right), 50 mg/ml ferrofluid (bottom left), or solid aluminium (bottom right).

even when the chamber is empty or for targets containing pure carrier fluid (see red plot of Figure 4.17), albeit at a lower magnitude than that recorded for the MNP-laden targets. In an ideal experimental scenario, there should be no change in the measured signal for a non-magnetic carrier fluid target between application and withdrawal of the PMF, and the differential magnitude should in theory roughly correspond to the experimental noise floor of around -94 dB. This is clearly not the case, so the observed trend indicates the influence of ferromagnetic material remaining within the apparatus of the imaging system (cables, connectors, and screws). As such, the

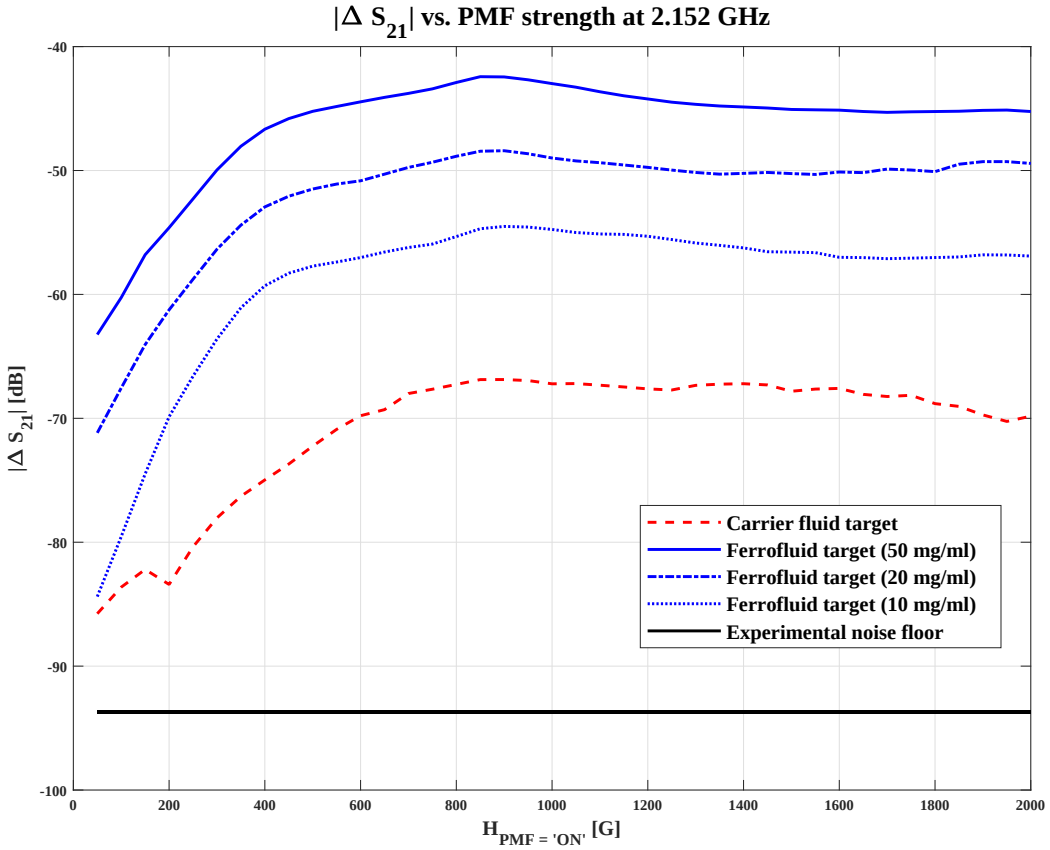

Figure 4.17: Measured magnitudes of ΔS_{21} depicted exclusively at the resonant frequency of interest, 2.152 GHz, for strengths of H_{PMF} varying from 50 G to 2000 G for centered 38 mm-diameter targets, one containing pure carrier fluid (red line) and others containing concentrations of ferrofluid (blue lines) varying from 10 mg/ml to 50 mg/ml. The experimental noise floor of the system is also shown (black line).

effective detection threshold of the experimental system in its current configuration is represented in Figure 4.17 by the PMF-dependent differential magnitude of the carrier fluid control target, which peaks as high as -67 dB at PMF strengths around 900 G. Following analysis of the trends observed in this cross-sectional data, the reader can see that the signal magnitudes exhibited from the ferrofluid targets scale linearly with MNP concentration. Encouragingly, there remains at least a 10 dB gap in magnitude between the differential signal of the lowest experimentally-tested MNP concentration (10 mg/ml) and that of the carrier fluid control target across all PMF

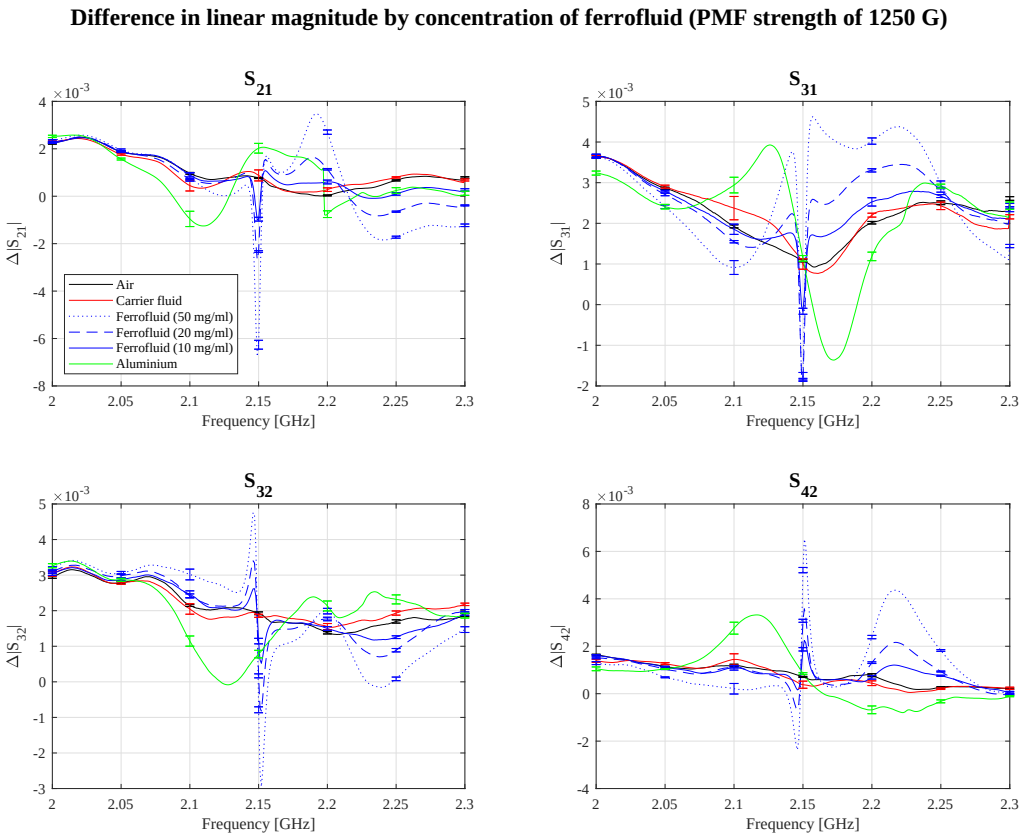

Figure 4.18: The differences in linear magnitudes ($\Delta|S_{xy|}$) of various centered targets, measured from 2.0–2.3 GHz for $S_{xy} = S_{21}, S_{31}, S_{32}, S_{42}$ plotted for a PMF strength of $H_{\text{PMF}} = 1250\ G$, with error bars. The ferrofluid targets here were all 38 mm in diameter but varied in MNP concentration (50 mg/ml, 20 mg/ml, and 10 mg/ml), and a directly proportional decrease in signal strength with dilution can be observed (blue lines) while the resonant frequency of interest (roughly 2.15 GHz) remains constant.

strengths, which bodes well for future investigations of MNP concentrations below 10 mg/ml.

Moreover, although there are more significant magnitude changes seen with the solid aluminium target (see the green trends of Figures 4.18–4.20), they clearly do not conform to the same pattern as that exhibited by the ferrofluid inclusions. Given that the aluminium ball is a strong scatterer itself, it provides a significant perturbation within the faceted chamber that would change the resonant modes excited by the

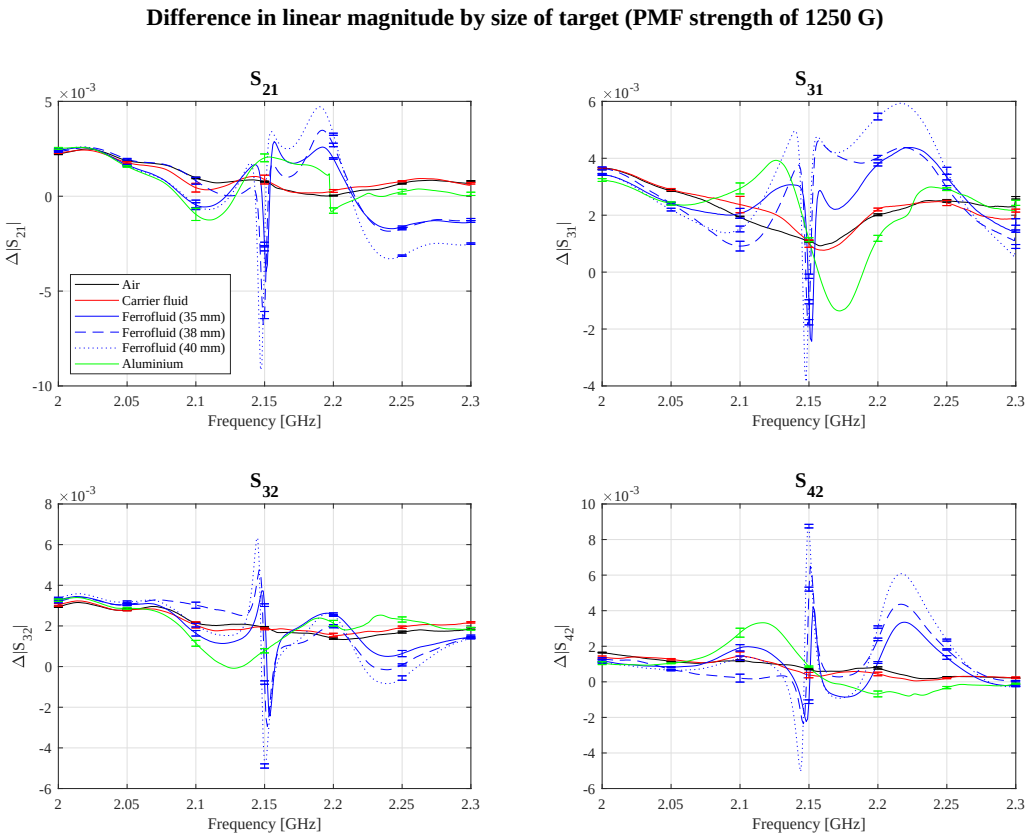

Figure 4.19: The differences in linear magnitudes ($\Delta|S_{xy}|$) of various centered targets, measured from 2.0–2.3 GHz for $S_{xy} = S_{21}, S_{31}, S_{32}, S_{42}$ plotted for a PMF strength of $H_{\text{PMF}} = 1250\ G$, with error bars. The ferrofluid targets here all had a constant concentration of 50 mg/ml but varied in diameter (35 mm, 38 mm and 40 mm), and a steady decrease in signal strength with decreased ferrofluid volume can be observed, along with a subtle upward shift in the sensitive resonant frequency with decreased target size (blues lines). This latter behaviour is consistent with loading effects imparted on the resonant faceted chamber by the volume of dielectric material within the targets. The carrier fluid control target has a diameter of 38 mm.

wire monopoles, perhaps distorting or amplifying the effect of the ferromagnetic material within the cables and connectors of the faceted chamber, and could be subject to induced eddy currents, all of which could explain the fluctuations in magnitude seen with changes in PMF strength. The fact that these magnitude changes for the aluminium target also vary considerably with position (Figure 4.19) lends credence to the likelihood that these measurements are predominantly artifactual.

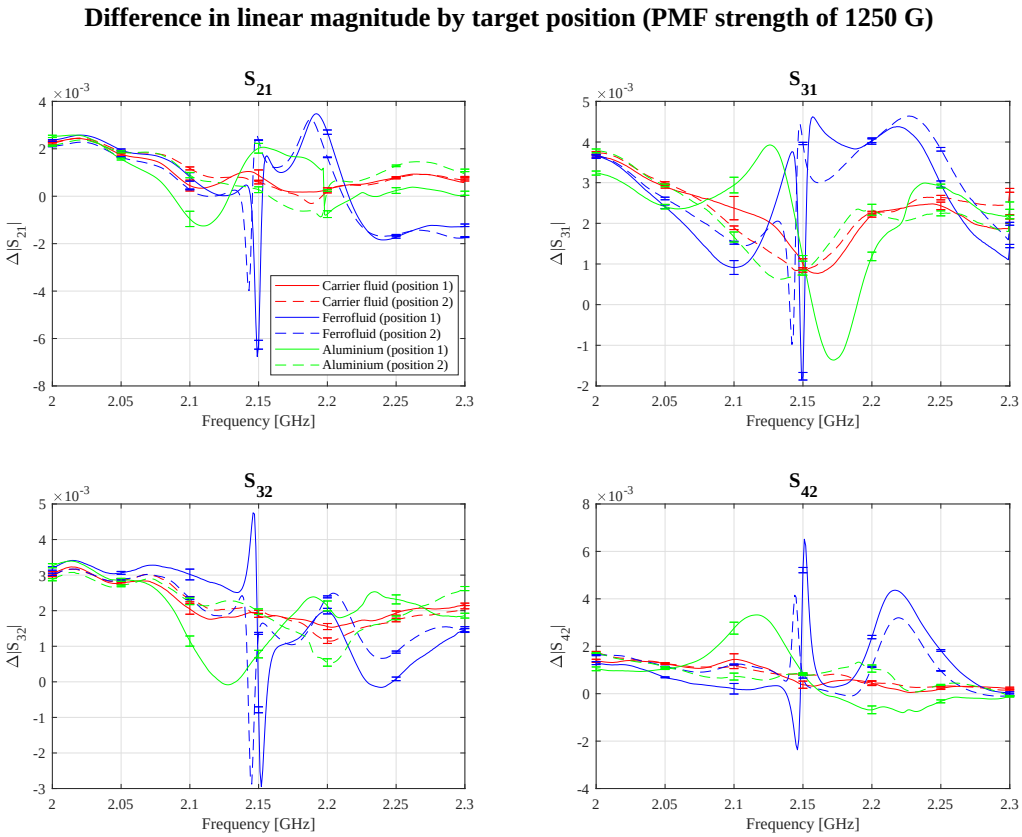

Figure 4.20: The differences in linear magnitudes ($\Delta|S_{xy}|$) of various targets in two positions, measured from 2.0–2.3 GHz for $S_{xy} = S_{21}, S_{31}, S_{32}, S_{42}$ plotted for a PMF strength of $H_{\text{PMF}} = 1250\ G$, with error bars. Targets were all 38 mm in diameter, and either centered (position 1) or radially off-set by approximately 2.0 cm towards Antenna 2 (see Figure 4.5–4.6). Ferrofluid target concentration was 50 mg/ml. A shift in the behaviour of the resonant curve and its peak frequency can be observed between position 1 and 2, consistent with slight changes in the resonant mode excited within the faceted chamber dependent on dielectric target placement.

The blue trends of Figure 4.18 for the ferrofluid targets demonstrate an expected directly proportional decrease in signal strength with dilution of the MNPs while the faceted chamber's resonant frequency of interest (roughly 2.15 GHz) remains constant, providing further reassurance that the observed differential signals are due to ferromagnetic resonant phenomena within the sample. While the magnitude change is weaker at the most dilute ferrofluid tested (10 mg/ml), it remains above the threshold

of detection for this imaging system. As several prior studies of MNP-enhanced MWI have pointed out, the most challenging aspect of employing this technology in biomedical applications, in particular for the early diagnosis of breast cancer, lies in targeting a sufficient amount of MNPs into the tumour via systemic administration [95, 106]. While the MNP concentrations employed here are comparable to these prior studies [93, 96], there have been recent discouraging reviews suggesting that the efficiency of nanoparticle targeting technologies may not currently be up to the task, demonstrating only a median of 0.7% of systemically injected nanoparticles are successfully delivered to solid tumours [105]. Nonetheless, although the most dilute MNP concentration used herein may currently be above the upper limit of biologically-achievable systemic delivery of MNPs to target breast lesions, the concentrations in this proof-of-concept study are not intended to represent realistic clinical values. Moreover, the lower limit of experimentally-detectable MNP concentrations in this prototype FRI system has not yet been established, and will be determined in future investigations of the system's experimental feasibility for biomedical applications.

It is acknowledged once more that the large diameters of the targets and their low-contrast non-conductive homogeneous contents greatly aid in their detection, and they are not representative of true biological imaging conditions. However, it is clear that significant improvement in sensitivity can be attained through the removal of unwanted ferromagnetic material in the next prototype FRI system such that more complex, multi-layer, high-permittivity breast phantoms can be confidently tested.

The S-parameter magnitude changes with ferrofluid target diameter seen in Figure 4.19 provide another interesting trend in that the observed differential signal steadily decreases in magnitude with smaller diameters of inclusions (due to the corresponding decrease in the volume of ferromagnetic material) while also exhibiting

a subtle upward shift in the sensitive resonant frequencies of the chamber with decreasing diameter. This latter behaviour is consistent with loading effects imparted on the faceted chamber by increasing or decreasing the volume of dielectric material within the targets; classical cavity-material perturbation theory states in general terms that any increase in ε and/or μ within a cavity can only decrease its resonance frequency [107], and correspondingly, any reduction in these dielectric or magnetic values would increase its resonance frequency.

Similarly, when plotting the changes in S-parameter magnitude with target position in Figure 4.20, the sensitive frequency band is also subject to a shift in peak location, as well as an alteration in the response pattern. This suggests that even when a dielectric load (*i.e.* an imaging target) of identical volume is placed elsewhere within the enclosure, the mode having a peak magnetic field at the new target position will occur at a different frequency.

The results of Figures 4.19 and 4.20 therefore demonstrate that the resonant mode distribution of the chamber is slightly changing, along with the resultant geometry-dependent resonant frequencies sensitive to the PMF-regulated fluctuations in magnetic susceptibility, and that these changes are coupled to the imaging target itself. The influence of the dielectric target's shape, size and position perturbs the resonance frequencies of the asymmetric enclosure; the underlying ferromagnetic resonance behaviour of the MNPs themselves within the target remains unaltered.

This logical dependency of the faceted chamber's resonant modes upon the imaging domain's dielectric contents, both in position and volume, leads to an interesting consequence when projecting future experimentation with more complicated, realistic imaging targets. For the simplified low-dielectric targets tested herein, determination of frequencies responsive to changes in ferromagnetic targets was fairly easily accom-

plished empirically, through observation of a single wideband 0.5–2.5 GHz sweep that was subsequently restricted to a relatively small frequency band (2.0–2.3 GHz). With biological phantoms consisting of large-volume high-permittivity tissue layers with irregular margins, these frequencies will likely be subject to significant downward shifts. Alternatively, the cavity-material coupling may deepen the complexity of the resonant mode distribution within the faceted chamber, introducing new second-order resonant effects that may yield useful ferromagnetic resonance signals at previously unsuitable imaging frequencies.

These observations would suggest that for practical application of the faceted chamber as an imaging system, each target to be imaged should be subject to a wideband "scout" scan of only a few transmitter-receiver pairs for a single PMF "on-off" cycle, and the differential data quickly analyzed to determine which discrete frequencies or frequency bands would be acceptable choices to proceed with full imaging data collection. The concept of pre-scanning complicated multiantenna imaging environments for selection of suitable imaging frequencies is not new, as similar methods to avoid frequencies where excessive antenna coupling occurs are well documented [108]. Consequently, the antennas employed in the system should ideally operate efficiently over a relatively wide frequency band. However, given the acceptable differential signal strengths obtained here (especially in earlier tests) using simple wire monopoles out of their efficient operating ranges, it would seem that wideband excitation of resonant modes can be achieved even with conventionally narrow-band antenna elements within the faceted chamber. Interestingly, such wideband data may demonstrate specific features unique to the shape, size and position of targets that could prove useful on its own for non-imaging applications, such as tumour detection and monitoring.

4.7 Conclusion

Preliminary signal acquisition and analysis of a microwave "ferromagnetic resonance imaging" or FRI system has been described, employing an air-based quasi-resonant flat-faceted enclosure deployed in a four-antenna configuration using simple wire monopoles, together with a powerful custom-designed electromagnet. The system was able to provide PMF-controlled differential electromagnetic signals potentially suitable for future imaging from low-dielectric targets infused with a ferromagnetic contrast agent in an air background. Exploitation of ferromagnetic resonance phenomena inherent to iron oxide MNPs in MWI has been demonstrated in earlier works through simulation and limited small-scale experiments, but to the authors' knowledge, this is the first test of a full-scale prototype imaging system able to fully realize magnetic contrast-enhanced 3D MWI.

It has been shown that the complex resonant mode distribution and corresponding contrast-sensitive frequency band within the asymmetric faceted chamber is heavily influenced by the size and position of dielectric material in the imaging domain. While this may seem to present a troubling complication to obtaining consistent, reliable imaging data, the issue could be overcome by changing the usual paradigm of designing 3D quantitative inverse-scattering-based MWI systems constrained to operate at narrow bands or discrete frequencies. As aforementioned, such solutions could include "scout" scans to determine target-specific best choices for imaging frequencies, and exploring non-imaging applications of wideband data.

In addition to revising the experimental setup to remove all potentially ferromagnetic material from the imaging environment, and using more realistic breast phantoms with complex permittivities consistent with human tissues, a systematic study of the field distributions within the chamber will be undertaken using 3D mod-

els to determine the effect of particular antenna designs and loading conditions. These models will guide the next stage of experimentation, which will involve fully populating the faceted chamber with dozens of new imaging antennas or probes to collect sufficient data for full 3D inversion.

Acknowledgment

The authors would like to acknowledge the financial support of the Natural Sciences and Engineering Research Council of Canada (NSERC) and thank our colleagues Evan Olson and Mohammad Asefi for their technical support and time investment in this project.

5

Conclusions and Future Work

5.1 Conclusions

In this thesis, several techniques aimed at improving the aforementioned limitations of MWI's spatial and contrast resolution have been presented through three separate published or submitted journal articles, using fundamentally different approaches. Although each approach addresses differing aspects of the imaging process, involving either the initial guesses used in reconstruction of high-frequency microwave scattered field data, the efficiency of iterative optimization algorithms employed in microwave inversions, or the method of data acquisition itself, they are not mutually exclusive solutions, and are intended to be independent of the underlying iterative optimization MWI algorithm, aside from the obvious modifications required for magnetic contrast-enhanced imaging. All of these techniques are promising tools for the enhancement of the overall quality of microwave images, ultimately helping to advance the modality towards widespread clinical application. The following summarizes the work presented herein and draws some overall conclusions for this thesis:

- The first article of Chapter 2 outlined the development of the described tissue-dependent mapping and frequency cycling techniques, showing their significant

positive effect on 2D synthetic microwave breast DGM-CSI reconstructions using fixed-iteration scenarios for different breast models, frequency bandwidths and boundary conditions. In particular, the remarkable stability imparted to high-frequency inversions of frequency-hopping or frequency-cycling sequences by modifying intermediate solutions based on prior information about human breast tissues and "anchoring" the imaginary part in place has spurred further interest in studying the formulation of initial guesses for iterative reconstruction algorithms. It may also lead to further insights into techniques of algorithmic regularization and the process of balancing real and imaginary contributions to the optimization algorithm's cost functional.

- The logical follow-up question that was raised from this first study, with regards to the choice of termination conditions for frequency-cycling reconstruction sequences, was answered by the second article of Chapter 3, which described the development of a generalized framework of parameterized stopping criteria. Implemented for the modified 2D DGM-CSI algorithm introduced in Chapter 2, these criteria established an automated approach to determine an appropriate number of iterations to be expended on reconstructions of each frequency within a cycle and when the reconstruction cycle has sufficiently converged to globally terminate the algorithm and output a final image. It was shown that these criteria, based on analyses of the statistical distribution of the data error along a window of past iterations, significantly improved the efficiency of the DGM-CSI algorithm, in some cases producing superior images with earlier termination, when compared to fixed-iteration scenarios. These positive effects were also shown to be robust for different breast models, frequency bandwidths, boundary conditions, and noise levels. The dramatic effect on imaging results

from PEC-bounded problems with higher noise levels in particular suggests that these criteria would be especially useful in noisy experimental conditions involving complex resonant enclosures, which conveniently represents the imaging environment currently undergoing extensive study at the EIL.

- The final article, reproduced in Chapter 4, outlines the preliminary efforts in implementing the described FRI system, consisting of a four-antenna array of wire monopoles within an air-based quasi-resonant aluminum faceted chamber housed within a custom-made electromagnet. Although the targets used in the experiment do not represent true breast phantoms, this successful test of a large-scale system capable of detecting the ferromagnetic response of MNPs is an encouraging first step towards full realization of 3D FRI of the breast. The specific discovery of particular antenna-independent sensitive frequency bands within the asymmetric chamber has led to further study of its complex resonant mode distribution and the effects of target composition, size and position within the imaging domain, and how wideband data collected from the system could be used to tailor target-specific imaging frequencies, or employed for non-imaging applications.

5.2 Future Work

The conclusions drawn from the research presented in this thesis, outlined in Chapters 2–4 and summarized in the previous section, along with the understood limitations of the studies published in those chapters' respective source articles, logically lead to several important future research goals, several of which have already been mentioned:

- The tissue-dependent mapping methodology, frequency-cycling technique, and novel stopping criteria, shown to be most effective when used in tandem, have only been fully implemented on the 2D version of the DGM-CSI algorithm, which is not used on experimental data, and only extensively tested on 2D synthetic breast models. While there have been a few subsequent tests of simplified tissue-dependent mapping with 3D DGM-CSI on synthetic data [38], as presented in Appendix B, the next steps would be full incorporation of these tools into the 3D algorithm, further analysis of their performance on 3D synthetic models, and ultimately, application to experimental data from realistic breast phantoms. Furthermore, since the Cole-Cole models employed to generate permittivity value estimates for the tissue-dependent mapping technique are based on dielectric measurements of *ex vivo* breast tissues, additional imaging tests should be carried out using wider ranges of mapped permittivity values to ensure the methodology's robustness to error which may be associated with data collected from *in vivo* tissues.

- Related to the extension of the novel stopping criteria to the 3D domain, further study should be dedicated to optimizing the choice of parameters for these stopping conditions, as described in Chapter 3, since the convergent behaviour of 3D data error and its statistical distribution (for both synthetic and experimental data) may be significantly different than two-dimensional scenarios. An analysis of how the boundary conditions, specifically the size of top aperture in the faceted chamber, would affect the statistics used in the stopping criteria for experimental data would be of particular interest.

- With regards to the signal acquisition tests of the FRI system of Chapter 4, there are several important limitations to these results that follow-up studies should

address. As pointed out in the article itself, the targets used in the experiments do not adequately represent human breast phantoms in that they are too large to approximate typical breast tumours, the dielectric constant of the carrier fluid is too low for human tissue, and the concentrations of MNPs used within these inclusions are higher than would likely be biologically achievable in practice. The four-antenna array also does not provide adequate data for 3D imaging, nor do the wire monopoles themselves represent suitable antenna designs for imaging purposes.

- While an immediate follow-up experiment could perhaps be performed with the current experimental set-up using more realistic multilayer breast phantoms with complex permittivities consistent with human tissues and smaller inclusions containing appropriately lower concentrations of MNPs, efforts should first be focused (as alluded to earlier) on precisely modelling the field distributions with the metallic faceted chamber to fully understand its complex resonant mode behaviour when it contains complicated high-permittivity targets. These models could then be used to determine the expected ferromagnetic resonance-sensitive frequency bands of the system when a breast phantom is within the imaging domain, and thus guide the design of suitable antennas for imaging or non-imaging applications. A potential future design could be based on modified coplanar half-loop probes, originally developed for use within the faceted chamber [4], which are small enough to fully populate the system with twenty-four or more elements.

- Another important consideration in the ongoing development of the experimental FRI system involves the identification and removal of all potentially ferromagnetic material from the imaging environment and subsequent replacement

with non-magnetic components, including the cables and connectors fastened to the faceted chamber, in order to refine the system's sensitivity in future experiments. In fact, a recent investigation by the research group at the University of Naples Federico II and CNR-IREA has confirmed the significant contribution of ferromagnetic connectors as a source of spurious magnetic effects affecting measurements in magnetic contrast-enhanced MWI [109].

- Different methods of PMF modulation should also be investigated as another effective means of lowering the MNP detection limit, such as the sinusoidal modulation technique introduced in [95].

- While referenced in Chapter 4 and elsewhere, the two-stage contrast-enhanced MWI reconstruction methodology which is critical for the recovery of both the complex electrical permittivity and magnetic permeability in strongly electrical and weakly magnetic biological targets has not been explicitly described in the body of this thesis. A 2016 conference paper on the subject has been provided in Appendix A, but results are again only shown for its implementation within the 2D DGM-CSI algorithm on synthetic data. As shown in Appendix B, this two-stage reconstruction technique has since been developed for a version of the 3D DGM-CSI algorithm [38], but has yet to be thoroughly tested on 3D synthetic and experimental data. In order for the FRI system in development to be able to exploit the weak signals detected from magnetic contrast-enhanced inclusions for imaging purposes, this CSI formulation must reliably perform full two-stage 3D quantitative inversion of ε_r and μ_r. As it has been observed in Appendix B that the first-stage reconstruction of the target's permittivity (subsequently used as an inhomogeneous background) has a significant effect on the accuracy of the second-stage reconstruction of magnetic permeability, any means by which

the quality of conventional inversions of ε_r can be improved should be employed in the final implementation of 3D DGM-CSI. As such, the ongoing integration of tissue-dependent mapping, frequency cycling, and stopping criteria within the portion of the 3D DGM-CSI algorithm responsible for reconstructions of complex permittivity will ultimately benefit the development of FRI when the code is extended to include this two-stage reconstruction methodology.

- Finally, alternative algorithms for MNP detection and imaging that do not require reconstructions of the relative permittivity, such as the truncated singular value decomposition (TSVD) scheme published in [33], should be investigated.

A

Appendix*: Two-stage reconstruction of complex dielectric permittivity and magnetic permeability for biomedical microwave imaging employing magnetic contrast agents

A.1 Abstract

An implementation of the Contrast Source Inversion algorithm employing the discontinuous Galerkin method (DGM-CSI) has been modified to produce quantitative 2D images of both the dielectric permittivity and magnetic permeability of synthetic contrast-enhanced breast models. These numerical models contain breast tumours embedded with accumulations of magnetic nanoparticles (MNP), with simulated magnetic properties appropriate for physiologically achievable concentrations. A reconstruction of the breast model's permittivity profile is obtained first and used as an inhomogeneous background for a second-stage reconstruction of the magnetic

*Reprinted with permission from Cameron Kaye, Ian Jeffrey and Joe LoVetri, "Two-stage reconstruction of complex dielectric permittivity and magnetic permeability for biomedical microwave imaging employing magnetic contrast agents," *4th Advanced Electromagnetics Symposium (AES)*, Malaga, Spain, July 2016.

permeability only, based on differential data obtained through the use of a static magnetic field. A brief description of this two-stage methodology for contrast-enhanced microwave imaging along with an example reconstruction of synthetic data is provided.

A.2 Introduction

Microwave imaging (MWI) has seen steady advancement towards specialized biomedical applications for several years, particularly in the field of diagnostic breast imaging. To that end, there has been interest in applying contrast enhancement to the modality to bolster its cancer detection and monitoring capabilities, leading to a number of studies of biocompatible substances that alter the gigahertz-range complex electrical permittivity of a tissue of interest, when properly targeted [26,27]. Magnetic contrast media have been recently explored as an alternative to permittivity-modifying agents, as these materials augment the complex magnetic permeability of the bodily tissues in which they accumulate, a property that has conventionally been ignored in MWI. In particular, suspensions of iron oxide magnetic nanoparticles (MNP), already approved and employed in magnetic resonance imaging (MRI), have encouraging potential as microwave contrast agents due to their strong ferromagnetic resonance properties at gigahertz frequencies [28, 96]. Another attractive quality of MNPs at nanometer diameters is their response to a static polarizing magnetic field (PMF), which modulates their aforementioned ferromagnetic resonance response such that the magnetic permeability boost afforded to the target tissue can effectively be turned on and off [2]. In a clinical setting, this characteristic provides an ideal mechanism to obtain reliable differential measurements through swift application and withdrawal of a weak PMF during signal acquisition. This process would minimize troublesome delays oth-

erwise associated with contrast-enhanced imaging during pre-contrast, post-contrast and wash-out periods that could yield images beset by artifacts related to patient motion. Moreover, the PMF-induced physical separation of tissues' electrical and magnetic responses validated the development of a two-stage reconstruction methodology described here; a discontinuous Galerkin formulation of the Contrast Source Inversion algorithm (DGM-CSI) has consequently been employed to produce quantitative images of both the complex dielectric permittivity and magnetic permeability of a 2D breast model.

A.3 Methods

A.3.1 DGM-CSI algorithm

All 2D breast images presented here have been reconstructed with a CSI algorithm that uses a high-order frequency-domain formulation of Maxwell's curl equations, employing the discontinuous Galerkin method (DGM-CSI) as a forward solver to support distinct high-order expansions for the fields, contrasts and contrast sources. Further details on DGM-CSI can be found in [57, 58].

A.3.2 Two-stage inversion procedure

The DGM-CSI formulation theoretically allows simultaneous recovery of both relative dielectric permittivity (ε_r) and magnetic permeability (μ_r) from electric and magnetic field data, but in practice, the coupling between the fields produced by both electric and magnetic targets makes it difficult to recover accurate images for both properties concurrently. Moreover, a small concentration of MNPs in a specific

volume of target tissue represents a very weak magnetic scatterer within a highly lossy biological environment, and the useful scattering signal from the MNP inclusion, being several orders of magnitude smaller than the strong electrical responses, is easily drowned out during simultaneous inversion of ε_r and μ_r. To overcome this difficulty, a two-stage reconstruction strategy was implemented that hinges on the fact that separate measurement data is available for two sets of targets within an otherwise identical imaging configuration (i.e. the dielectric and magnetic responses are separable during data collection via the application of a weak PMF). While the foundation of this differential measurement technique was proposed in [28], the important distinction for our reconstruction method lies in the use of inhomogeneous backgrounds in DGM-CSI to offer full quantitative inversion of both ε_r and μ_r.

To illustrate the procedure, suppose the existence of a target characterized by two complex relative permittivity and permeability profiles denoted by ε_1 and μ_1, and ε_2 and μ_2. To reflect the physics of applying a PMF, the target representing the scenario where the PMF is 'on' has μ_1 equal to some small residual constant above the permeability of free space [2] (for simplicity's sake, $\mu_1 = 1.0$ is assumed). When the PMF is 'off', the target has identical dielectric properties ($\varepsilon_2 = \varepsilon_1$) while μ_2 is now some inhomogeneous magnetic profile, typical of an MNP contrast enhancement. The following two-stage reconstruction is thus proposed:

1. Total fields E_1^{tot} are measured at all receivers for the target defined by the profiles ε_1 and μ_1. The incident field here, E_1^{inc}, is determined for the imaging system background medium ε_b and μ_b within the imaging domain, and its measured values at the receivers are used to covert total field measurements to scattered field data $E_1^{sct} = E_1^{tot} - E_1^{inc}$.

2. The DGM-CSI algorithm is applied to the scattered field data E_1^{sct} to recon-

struct the contrast functions $(\varepsilon_1 - \varepsilon_b)/\varepsilon_b$ and $(\mu_1 - \mu_b)/\mu_b$. As aforementioned, $\mu_1 = \mu_b$ can be assumed for simplicity, such that only ε_1 need be recovered.

3. Total fields E_2^{tot} are measured at all receivers for the target defined by the profiles ε_2 and μ_2. A new scattered field dataset is taken to be $E_2^{tot} - E_1^{tot}$. The profiles ε_1 and μ_1 recovered in step 2 are used as a numerical inhomogeneous background ε_N and μ_N for this reconstruction [67], and its corresponding "incident" fields within the imaging domain are calculated as required for evaluation of the CSI domain error cost functional.

4. DGM-CSI is now applied to the scattered field data $E_2^{tot} - E_1^{tot}$ to reconstruct $(\varepsilon_2 - \varepsilon_N)/\varepsilon_N$ and $(\mu_2 - \mu_N)/\mu_N$, from which ε_2 and μ_2 can be recovered. As any difference between E_2^{tot} and E_1^{tot} is assumed to be solely due to PMF-induced variations in magnetic permeability, the dielectric contrast is assumed to be zero, and at this stage the algorithm is constrained to recover only μ_2.

A.3.3 Synthetic breast model

Synthetic data was generated from a two-dimensional MRI-derived breast model supplied by the University of Wisconsin's public database (ID: 070604PA2) with tissue-dependent complex permittivity values calculated for a frequency of 1.0 GHz from fitted 4-pole Cole-Cole models [1]. A simple circular inclusion, 1 cm in diameter, was embedded in a region of fibroglandular tissue at $(x, y) = (-0.01, -0.012)$[m] and also given a frequency-appropriate permittivity for breast cancer. Additionally, this tumour was seeded with a weak magnetic permeability appropriate for a 10 mg/mL concentration of 10 nm-diameter magnetite MNPs at 1.0 GHz ($\mu_r = \mu_2 = 1.006 - 0.015i$) [96]. The complete model is depicted in Fig. A.1.

For this 2D transverse magnetic (TM) model, electric field data (E_z) was generated in a low-loss background of $\varepsilon_b = 23 - 1.13i$ and $\mu_b = 1.0$ with 24 transmitters and 48 receivers evenly distributed at a radius of 10 cm, through the use of a finite-element method (FEM) forward solver with a finely-discretized mesh independent from that used for the DGM-CSI inversion. Doubling the number of receivers per transmitter was found to be helpful in the quantitative recovery of the magnetic inclusion, which produces a very weak scattering signal. Three sets of data (*i.e.* the fields that would be measured in practice) were separately corrupted by additive Gaussian white noise at an SNR of 80dB: incident field E_1^{inc}, and total fields E_1^{tot} and E_2^{tot}. The outer skin boundary was the only prior information employed during inversions; it was used as the problem's imaging domain. The inner skin boundary was not provided as prior data to the algorithm.

A.4 Results and discussion

The imaging results of a 1.0 GHz two-stage DGM-CSI inversion of synthetic data are shown in Fig. A.2. This low reconstruction frequency illustrates the usefulness of the two-stage inversion technique for improving the cancer detection potential of contrast-enhanced MWI. The relatively poor spatial resolution achievable at 1.0 GHz has blurred the area of interest around the tumour's location in $\mathrm{Re}(\varepsilon_r)$ and yielded a poor recovery of $\mathrm{Im}(\varepsilon_r)$, limiting the diagnostic utility of the complex dielectric permittivity reconstruction by itself. However, the inversion of the magnetic permeability, despite some minor noise-related artifacts, has correctly localized the MNP inclusion. This is especially evident when μ_r is rescaled to remove values below 40% of the expected maximums for the real and imaginary parts (see bottom plots of Fig. A.2). The real part of μ_r is somewhat less accurate than the imaginary

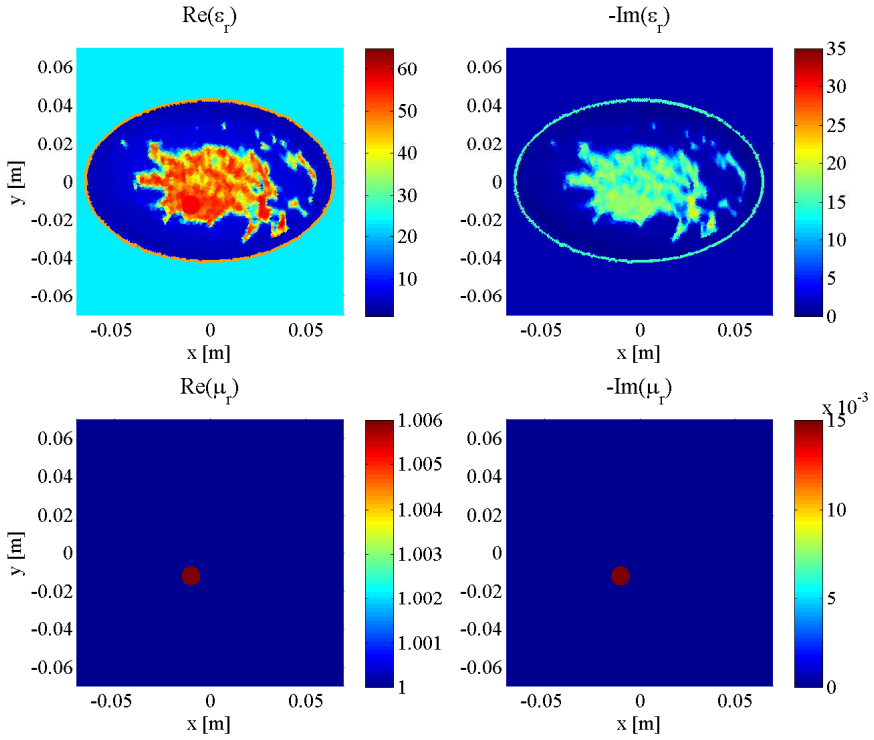

Figure A.1: Complex electromagnetic properties of University of Wisconsin 2D synthetic breast model at 1.0 GHz (ID: 070604PA2): ε_r (top) and μ_r (bottom).

component, as the "hot spot" has been subjected to an erroneous narrowing and a slight medial shift, likely due to noise distortion. Given its minute permeability value above that of free space ($\mathrm{Re}(\mu_r) = 1.006$), difficulties in its reliable reconstruction from noisy data are not surprising. Regardless, given the nebulous region of high permittivity around the "7 o'clock" position in $\mathrm{Re}(\varepsilon_r)$ where the tumour is located, in a hypothetical clinical scenario it is clear that a combination of both ε_r and μ_r would provide a more useful assessment of possible breast pathology than the reconstruction of dielectric permittivity alone.

A.5 Conclusion

A two-stage contrast-enhanced MWI reconstruction methodology for the recovery of complex electrical permittivity and magnetic permeability in strongly electrical and weakly magnetic biological targets has been successfully tested using the DGM-CSI algorithm on 2D synthetic data. Follow-up studies with a CSI formulation capable of full 3D quantitative inversion of ε_r and μ_r are ongoing, employing synthetic data acquired from 3D breast models and experimental data from the University of Manitoba Electromagnetic Imaging Lab's latest imaging system.

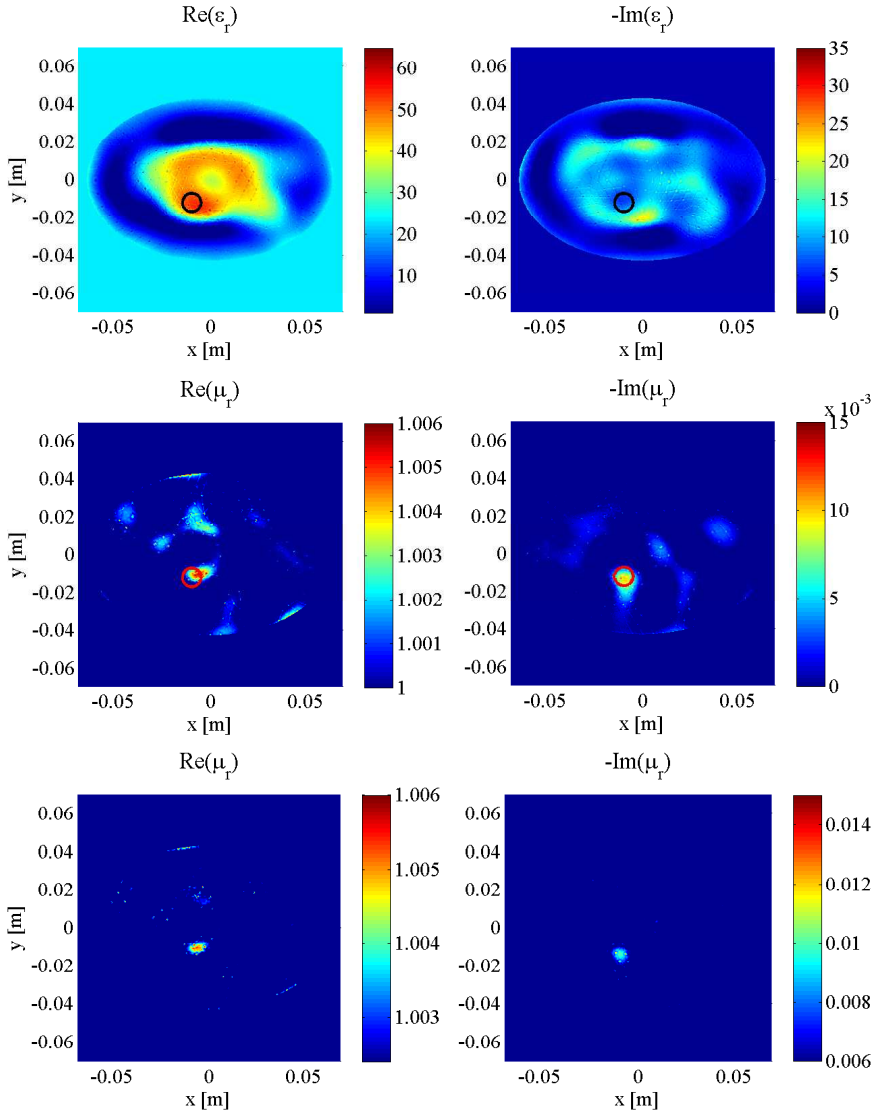

Figure A.2: DGM-CSI reconstructions of complex ε_r (top) and μ_r (middle) from synthetic data (SNR = 80dB) at 1.0 GHz, where the tumour's true location has been highlighted by black and red circles. The bottom plots display values above 40% of the expected maximum of μ_r.

B

Appendix*: Initial two-stage reconstruction of complex dielectric permittivity and magnetic permeability in synthetic 3D models using Discontinuous Galerkin Contrast Source Inversion

B.1 Abstract

As a logical advancement of the research undertaken on two-dimensional magnetic contrast-enhanced imaging outlined in Appendix A, this appendix briefly describes the three-dimensional implementation of the Contrast Source Inversion algorithm employing the discontinuous Galerkin method (DGM-CSI) which has been similarly modified to produce quantitative 3D images of both the dielectric permittivity and magnetic permeability of synthetic contrast-enhanced breast phantoms. The simple multilayer numerical phantom outlined here contains a breast tumour embedded with an accumulation of magnetic nanoparticles (MNP), again with simulated magnetic

*Partially reproduced content with permission from Cameron Kaye, Kevin Brown, Ian Jeffrey and Joe LoVetri, "Experimental 3D Microwave Imaging of Magnetic Targets using Discontinuous Galerkin Contrast Source Inversion and a Two-stage Reconstruction Technique," *2nd URSI Atlantic Radio Science Conference (URSI AT-RASC)*, Gran Canaria, Spain, June 2018.

properties appropriate for physiologically achievable concentrations. The previously described two-stage reconstruction technique is first applied in a best-case scenario where perfect prior information of the phantom's permittivity profile (including the breast tumour) allows its direct use as an inhomogeneous background for the second-stage reconstruction of the magnetic permeability. Our preliminary efforts in a second scenario, producing a first-stage inversion of the relative permittivity of the same 3D breast phantom as the inhomogeneous background for the second-stage reconstruction of the magnetic permeability, are also shown. Encouragingly, a simplified implementation of tissue-dependent mapping described in Chapter 2 on the first stage 3D reconstruction of the complex permittivity proved instrumental in producing an acceptable second-stage result.

B.2 Introduction

While microwave imaging (MWI) for biomedical applications continues to make steady progress as a prospective clinical modality, a promising research trajectory has recently emerged involving the use of contrast enhancement with magnetic nanoparticles (MNPs) [28, 106]. While reconstructed profiles of the complex relative permittivity ($\hat{\varepsilon}_r$) yield important anatomical information of biological targets, the addition of MNPs accumulating preferentially in metabolically-active tissue could allow the relative magnetic permeability ($\hat{\mu}_r$) to play an important role in the future cancer diagnostic capabilities of this technology. A fully parallelized 3D implementation of Contrast Source Inversion using the Discontinuous Galerkin Method (DGM-CSI), a fast and robust imaging algorithm supporting the use of inhomogeneous backgrounds with high-order expansions over coarse meshes, has been successfully used to reconstruct synthetic targets with liberally high values of magnetic permeability in the

past [110]. However, the algorithm has not hitherto been subjected to testing on realistic phantoms of MNP-laden breast tumours; progress to this end is demonstrated herein.

To accurately accomplish these reconstructions when contending with the inherently low-level magnetic signals from physiologically achievable MNP concentrations, a two-stage reconstruction procedure [37] is employed. Based on the observation that the strong dielectric signal response of underlying tissue can be elegantly separated from the MNPs magnetic response through the use of a weak external static polarizing magnetic field (PMF) [28], the complex relative permittivity can be independently reconstructed and used as an inhomogeneous background in DGM-CSI for the subsequent inversion of magnetic permeability. Herein we demonstrate the capabilities of the two-stage procedure to first reconstruct the complex permittivity profile, and subsequently the MNP-enhanced magnetic profile, of a synthetic phantom within a modelled semi-resonant breast imaging chamber capable of both electric and magnetic field measurements [3].

B.3 Methods

B.3.1 DGM-CSI algorithm

The breast images presented here, similar to Appendix A, have been reconstructed with a CSI algorithm that uses a high-order frequency-domain formulation of Maxwell's curl equations, employing the discontinuous Galerkin method (DGM-CSI) as a forward solver to support distinct high-order expansions for the fields, contrasts and contrast sources, but in a full 3D vector-field implementation. Further details on both 2D and 3D DGM-CSI can be found in [38, 57–59].

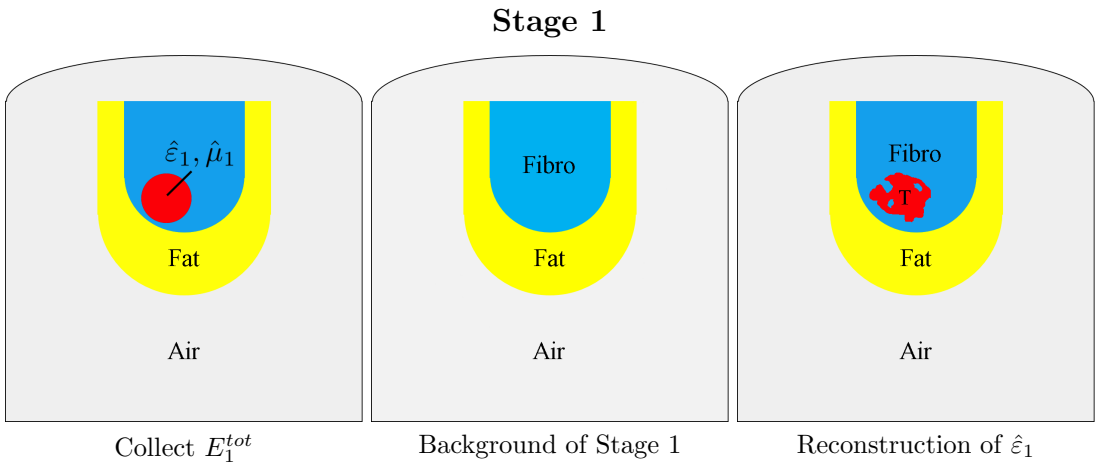

Figure B.1: First stage scenario depicted for a multilayer synthetic phantom in air containing fat (yellow), fibroglandular tissue (blue, "Fibro" = fibroglandular), and a tumour (red).

B.3.2 Two-stage inversion procedure

The fundamental concepts behind the two-stage reconstruction strategy have already been described in Appendix A, where the importance of using inhomogeneous backgrounds was emphasized. To further elaborate on this methodology, the procedure is again illustrated here, with slightly modified notation. We again suppose the existence of a target characterized by two complex relative permittivity and permeability profiles denoted by $\hat{\varepsilon}_1$ and $\hat{\mu}_1$, and $\hat{\varepsilon}_2$ and $\hat{\mu}_2$. To reflect the physics of applying a PMF, the target representing the scenario where the PMF is 'on' has $\hat{\mu}_1$ equal to some small residual constant above the permeability of free space [2] ($\hat{\mu}_1 = 1.0$ for simplicity). When the PMF is 'off', the target has identical dielectric properties ($\hat{\varepsilon}_2 = \hat{\varepsilon}_1$) while $\hat{\mu}_2$ is now some inhomogeneous magnetic distribution localized in the tumour, typical of an MNP contrast enhancement. The following two-stage reconstruction follows closely what was described in Appendix A, with slight modifications and figures added for clarity.

1. For the first stage (see Figure B.1), total fields E_1^{tot} are measured at all receivers

for the phantom defined by the profiles $\hat{\varepsilon}_1$ and $\hat{\mu}_1$. The incident field here, E_1^{inc}, is determined for the imaging system background medium $\hat{\varepsilon}_b$ and $\hat{\mu}_b$ within the imaging domain, and its measured values at the receivers are used to covert total field measurements to scattered field data $E_1^{sct} = E_1^{tot} - E_1^{inc}$. For the synthetic example depicted in Figure B.1, the background medium $\hat{\varepsilon}_b$ contains the fat and fibroglandular layers of the model such that the scattered field E_1^{sct} is due only to the tumour.

2. The DGM-CSI algorithm is applied to the scattered field data E_1^{sct} to reconstruct the contrast functions $(\hat{\varepsilon}_1 - \hat{\varepsilon}_b)/\hat{\varepsilon}_b$ and $(\hat{\mu}_1 - \hat{\mu}_b)/\hat{\mu}_b$. As aforementioned, $\hat{\mu}_1 = \hat{\mu}_b$ can be assumed for simplicity, such that only $\hat{\varepsilon}_1$ need be recovered.

3. For the second stage (see Figure B.2), total fields E_2^{tot} are measured at all receivers for the target defined by the profiles $\hat{\varepsilon}_2$ and $\hat{\mu}_2$. A new scattered field dataset is taken to be $E_2^{tot} - E_1^{tot}$. The profiles $\hat{\varepsilon}_1$ and $\hat{\mu}_1$ recovered in step 2 are used as an inhomogeneous numerical background $\hat{\varepsilon}_N$ and $\hat{\mu}_N$ for this reconstruction [67], and its corresponding "incident" fields within the imaging domain are calculated as required for evaluation of the CSI domain error cost functional.

4. DGM-CSI is now applied to the scattered field data $E_2^{tot} - E_1^{tot}$ to reconstruct $(\hat{\varepsilon}_2 - \hat{\varepsilon}_N)/\hat{\varepsilon}_N$ and $(\hat{\mu}_2 - \hat{\mu}_N)/\hat{\mu}_N$, from which $\hat{\varepsilon}_2$ and $\hat{\mu}_2$ can be recovered. As any difference between E_2^{tot} and E_1^{tot} is assumed to be solely due to PMF-induced variations in magnetic permeability, the dielectric contrast is assumed to be zero $(\hat{\varepsilon}_2 = \hat{\varepsilon}_1)$, and at this stage the algorithm is constrained to recover only $\hat{\mu}_2$.

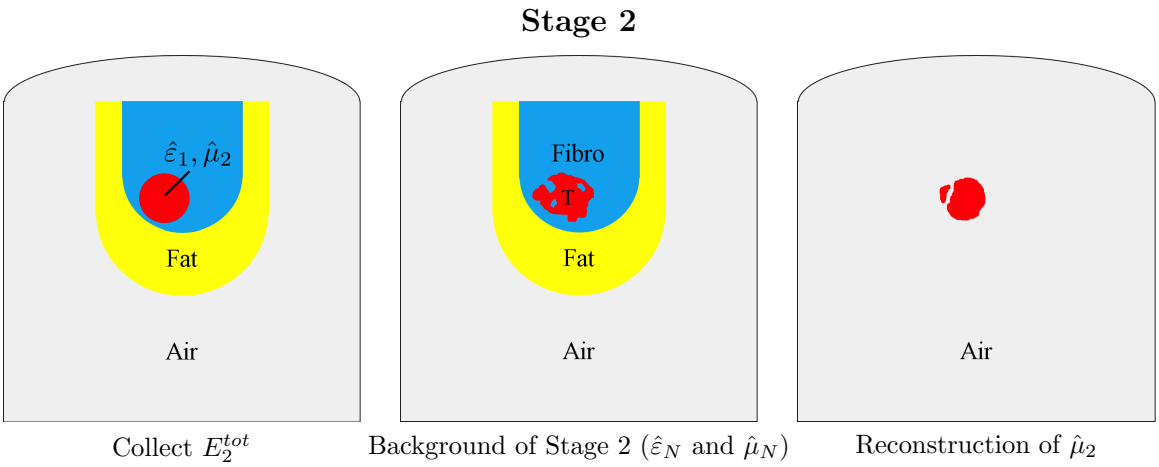

Figure B.2: Second stage scenario using reconstruction result from Figure B.1 as background. Note that since the dielectric contrast should be zero, $\hat{\varepsilon}_2 = \hat{\varepsilon}_1$ in the ideal case, and since the final inversion of $\hat{\mu}_2$ is isolated to magnetic permeability only, it is depicted on an empty background with detectable changes presumably occurring only within the tumour (red).

B.3.3 Synthetic breast model

Synthetic data were generated from a three-dimensional breast phantom enclosed within an air-filled PEC-faceted chamber based on that described in [3, 4], with a plexiglass lid ($\hat{\varepsilon}_{\text{lid}} = 3.0 - i0.001$), depicted in Figure B.3. The simplified breast consisted of a single fat layer as background ($\hat{\varepsilon}_b = 3.07 - i0.26$) containing a contrast-enhanced spherical tumour with complex dielectric and magnetic properties ($\hat{\varepsilon}_1 = \hat{\varepsilon}_2 = 14 - i11.5$ and $\hat{\mu}_2 = 1.01 - i0.02$) of radius $\lambda_b/6$ for an interrogation frequency of 1.4 GHz. Magnetic field data were generated (H_ϕ) using twenty-four transmitters with twenty-three receivers per transmitter, and corrupted by additive uniform noise at 5% of the maximum magnitude of the scattered field H^{sct} [3, 69, 84]. Fields and solutions were expanded using third order polynomials in DGM-CSI.

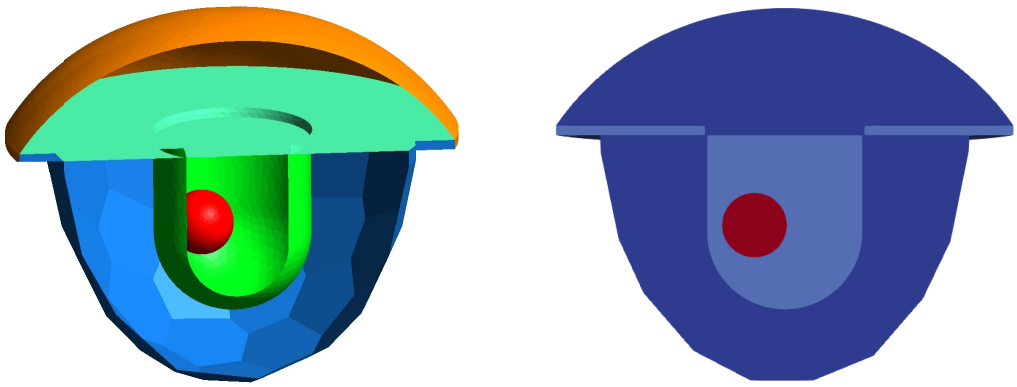

Chamber model Background ($\hat{\varepsilon}_b = 3.07 - j0.26$)

Figure B.3: Three-dimensional breast phantom in asymmetric PEC-faceted chamber [3, 4] (left), and corresponding cross-sectional view, with fat-layer background permittivity seen in light blue (right).

B.4 Results and discussion

Two imaging scenarios were studied; one involved no first-stage reconstruction of the background complex permittivity ($\hat{\varepsilon}_1$) and instead used perfect prior information of the breast fat layer and tumour as the inhomogeneous background for a single reconstruction of $\hat{\mu}_2$, representing an ideal case. The second scenario carried out the two-stage reconstruction methodology as described in Section B.3.2, using the breast fat layer as the background for the first stage reconstruction of $\hat{\varepsilon}_1$, which was then used as the inhomogeneous background $\hat{\varepsilon}_N$ for the second-stage reconstruction of $\hat{\mu}_2$. This numerical background was subject to modifications, however, in order to obtain an acceptable result for the second-stage inversion, as described below. The results provided here were presented in [38].

The imaging result of $\hat{\mu}_2$ using perfect prior knowledge of the breast fat and tumour permittivities, with Imag($\hat{\mu}_2$) depicted in Figure B.4 and Figure B.5, turned out predictably well, producing a cluster of elements with magnetic permeability approaching the expected value of roughly -0.02 in the imaginary part, with a crisp

spherical border neatly coinciding with the precise location of the breast tumour. Only minimal artifactual elements can be seen outside of the breast tumour's margins, near the fat layer boundary. This result confirms that an ideally reproduced complex permittivity background appropriately leads to an excellent inversion of the superimposed magnetic permeability profile in 3D synthetic models.

The initial attempt at the full two-stage reconstruction procedure, however, yielded a result for $\hat{\mu}_2$ so highly corrupted by artifact in the second stage (not shown) that a definitive confluent focus of strong permeability values representing the solitary tumour could not be identified. A simplified version of the tissue-dependent mapping technique, described in Chapter 2 for 2D models, was subsequently implemented and applied to the first-stage reconstruction of $\hat{\varepsilon}_1$, as follows:

1. The real and imaginary parts of the complex permittivity were reconstructed at 1.4 GHz, using the boundaries of the breast model fat layer as the imaging domain.

2. A point-by-point search through the reconstructed real part of each node or nodal basis coefficient in the 3D DGM-CSI mesh was performed to classify the type of breast tissue based on a simplified range of expected values of dielectric constant at that frequency:

    2.1. Nodes were first classified as "air" if their real and imaginary parts fell within a minuscule specified error tolerance of $\hat{\varepsilon}_{\text{air}} = 1.0 - i0.001$. Similarly, nodes were classified as "plexiglass" if their real and imaginary parts were within the same tolerance of $\hat{\varepsilon}_{\text{plex}} = 3.0 - i0.001$. These nodes typically would reside outside of the problem's imaging domain and would not contribute to the reconstructed permittivity unless in close proximity to

the fat layer boundary.

2.2. Nodes with reconstructed real parts $\mathrm{Re}(\hat{\varepsilon}_r) \leq 4.0$ not previously classified as "air" or "plexiglass" were classified as "fat".

2.3. Remaining nodes with reconstructed real parts $\mathrm{Re}(\hat{\varepsilon}_r) > 4.0$ not previously classified as "air" or "plexiglass" were classified as "tumour".

3. A search through each mesh element was then performed to categorize them into the same groups based on how the majority or plurality of its nodes were classified (*i.e.* if most nodes within the mesh element were classified as "fat", then that element would be classified as "fat", and similarly for "tumour", "air", etc.). The number of nodes per mesh element depends upon the order of polynomial expansion employed for the DGM-CSI reconstruction (20 for 3$^{\mathrm{rd}}$ order).

4. Based on the mesh elements' final classification, the complex permittivity of *all* nodes within that element would be discarded and replaced with the following:

4.1. The complex permittivity of nodes within mesh elements classified as "air" would become $\hat{\varepsilon}_{\mathrm{air}} = 1.0 - i0.001$.

4.2. The complex permittivity of nodes within mesh elements classified as "plexiglass" would become $\hat{\varepsilon}_{\mathrm{plex}} = 3.0 - i0.001$.

4.3. The complex permittivity of nodes within mesh elements classified as "fat" would become $\hat{\varepsilon}_{\mathrm{fat}} = 3.07 - i0.26$.

4.4. For mesh elements classified as "tumour", the average of the real part of the permittivity of nodes within that element would be calculated ($\bar{\varepsilon}_{\mathrm{avg}} = \{Re(\hat{\varepsilon}_r)\}_{\mathrm{avg}}$), and every node's complex permittivity replaced with an empirically determined formula : $\hat{\varepsilon}_{\mathrm{tumour}} = (\bar{\varepsilon}_{\mathrm{avg}} + 6.0) - i(\bar{\varepsilon}_{\mathrm{avg}} + 3.5)$. (This

formula was a purely *ad hoc* solution and its values were determined by trial and error.)

5. This newly generated complex permittivity profile, which – similar to the 2D case outlined in Chapter 2 – maintains the structural similarities between the real and imaginary parts of the solution, is then used as the inhomogeneous numerical background for the second-stage inversion of the complex magnetic permeability ($\hat{\mu}_r$).

The two-stage imaging results, using the reconstructed complex permittivity modified by the aforementioned simplified tissue-dependent mapping technique before being employed as the numerical background for the second-stage inversion of magnetic permeability, are shown in Figure B.6 and Figure B.7. Only Imag($\hat{\mu}_2$) is shown, and the visible elements have been subjected to a 85% threshold of its expected value (-0.02) for display purposes. There is a focal confluence of higher magnitude permeability elements within the margins of the expected location of the breast tumour, but this irregular area does not conform smoothly to the spherical boundary of the modelled inclusion, and the results are affected by more scattered artifact compared to those of the "perfect prior" scenario of Figure B.4 and Figure B.5.

Nonetheless, given that these results were a marked improvement over attempts that used an inhomogeneous background of the unmodified reconstruction of the complex permittivity, it is clear that the tissue-dependent mapping technique developed and tested on 2D reconstructions in Chapter 2 can impart a beneficial effect on two-stage 3D DGM-CSI reconstructions, as well. In this case, the implementation of the mapping algorithm for [38] was grossly simplified, however, and elements classified as "tumour" were assigned complex permittivity values augmented by arbitrary constants chosen largely through empirical observation of reconstruction results. Despite

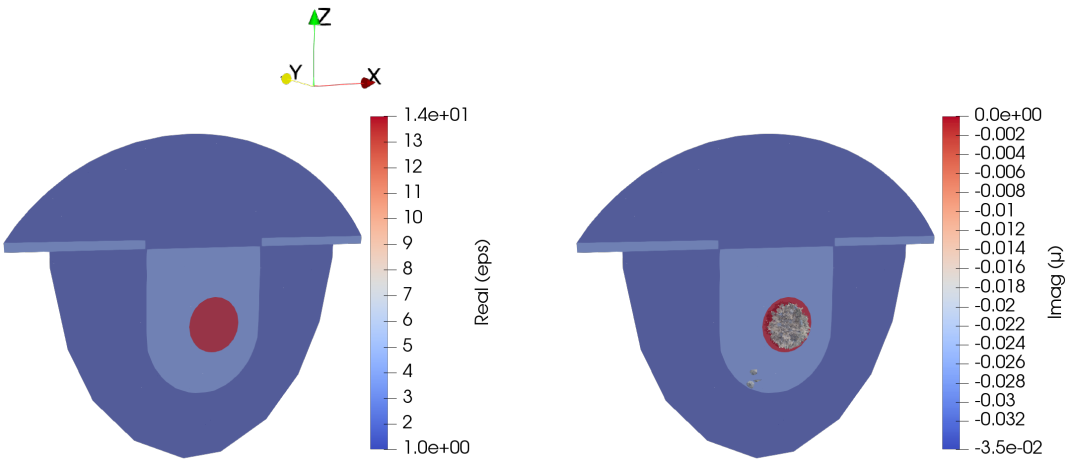

Stage 1: $\hat{\varepsilon}_r$ (perfect prior) Stage 2: DGM-CSI Imag($\hat{\mu}_r$)

Figure B.4: Imaging results of 3D DGM-CSI reconstruction technique using perfect prior knowledge of the scenario's complex permittivity (left) as an inhomogeneous background to produce an inversion of $\hat{\mu}_r$ (right).

the limited success demonstrated by this *ad hoc* technique, addition of such constant values to the complex permittivity introduces sharp discontinuities in the modified permittivity profile that are markedly inconsistent with the physics of DGM-CSI's reconstruction, and undoubtedly contributed to artifactual errors in the second-stage inversion of $\hat{\mu}_r$. Future use of a more sophisticated tissue-dependent mapping algorithm similar to that outlined in Chapter 2 is well warranted, and may further improve these two-stage 3D reconstructions.

B.5 Conclusion

The two-stage contrast-enhanced MWI reconstruction methodology for the recovery of complex electrical permittivity and magnetic permeability in strongly electrical and weakly magnetic biological targets previously developed and tested using the DGM-CSI algorithm on 2D synthetic data has been demonstrated in this Appendix in

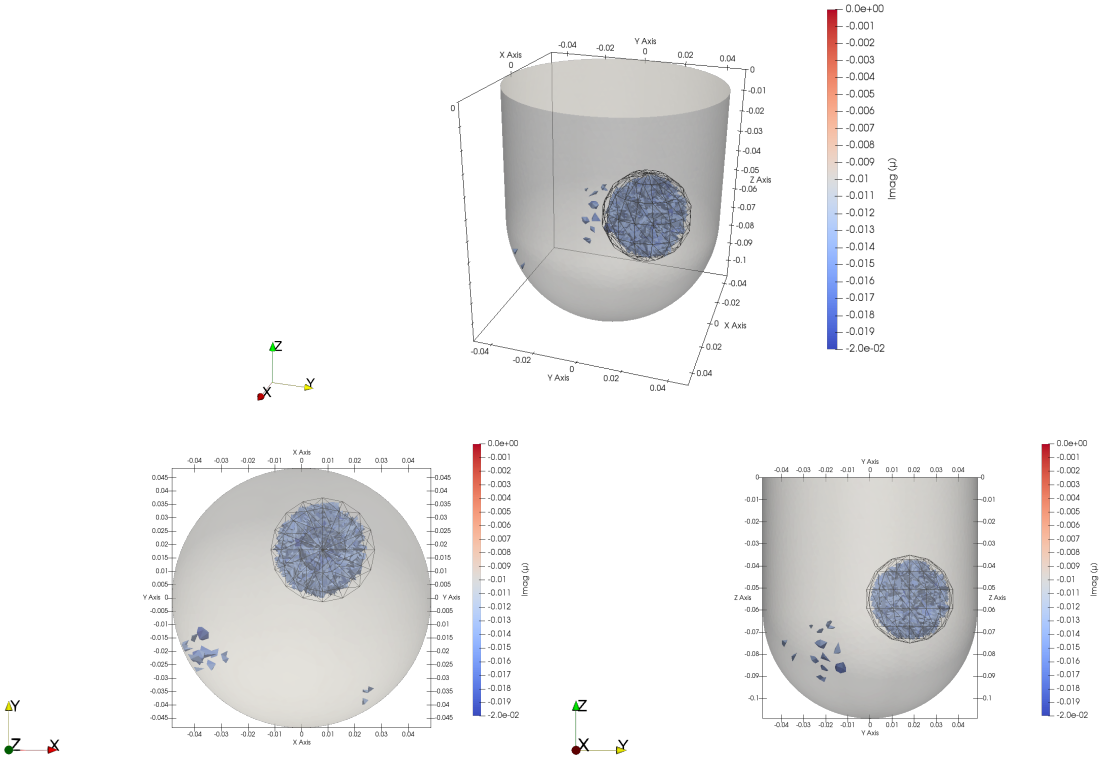

Figure B.5: Multiple views of 3D DGM-CSI inversion of Imag($\hat{\mu}_2$), with perfect prior complex permittivity background.

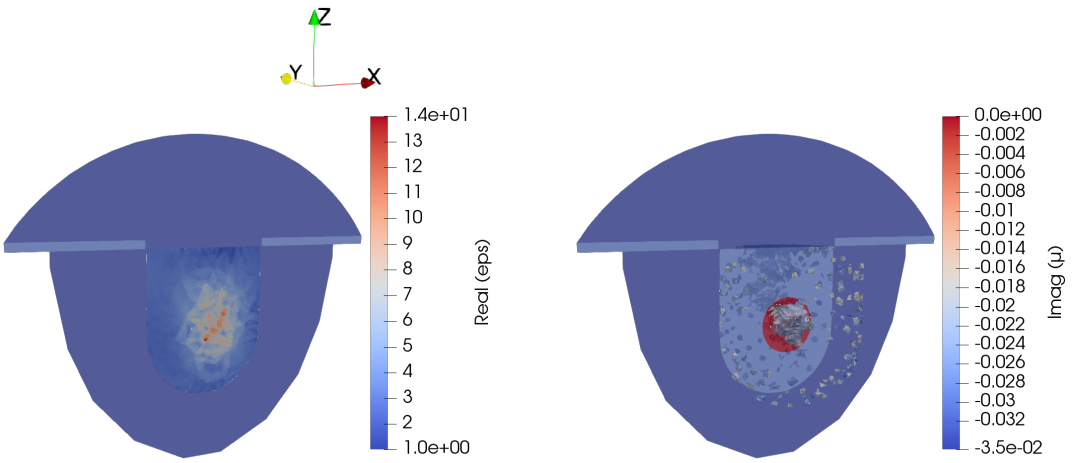

DGM-CSI Real($\hat{\varepsilon}_r$) (1^{st} stage) DGM-CSI Imag($\hat{\mu}_r$)

Figure B.6: Imaging results of two-stage 3D DGM-CSI reconstruction technique, with the scenario's complex permittivity inversion (left) used as an inhomogeneous background to produce an inversion of $\hat{\mu}_r$ (right). Imag($\hat{\varepsilon}_r$) was generated through a simple element-by-element mapping of Real($\hat{\varepsilon}_r$) (not shown). Imag($\hat{\mu}_r$) was subjected to a threshold of 85% of expected value for display purposes; Real($\hat{\mu}_r$) not shown.

a limited capacity for 3D synthetic data, as well. The scenario employing perfect prior knowledge of the simple breast model's complex permittivity as an inhomogeneous background produced the best results for the subsequent inversion of magnetic permeability, as expected. Use of the unaltered first-stage DGM-CSI complex permittivity reconstruction as the numerical background in a second scenario did not produce a viable second-stage inversion of $\hat{\mu}_r$, but these results were significantly improved when the reconstructed background permittivity was modified by a very simple *ad hoc* implementation of the tissue-dependent mapping algorithm previously applied on 2D DGM-CSI inversions. A more sophisticated implementation of this technique is in development and further testing on more complex 3D synthetic models is ongoing. This preliminary encouraging result nonetheless reinforces the motivation behind the use of the tissue-dependent mapping technique introduced in Chapter 2 as part of

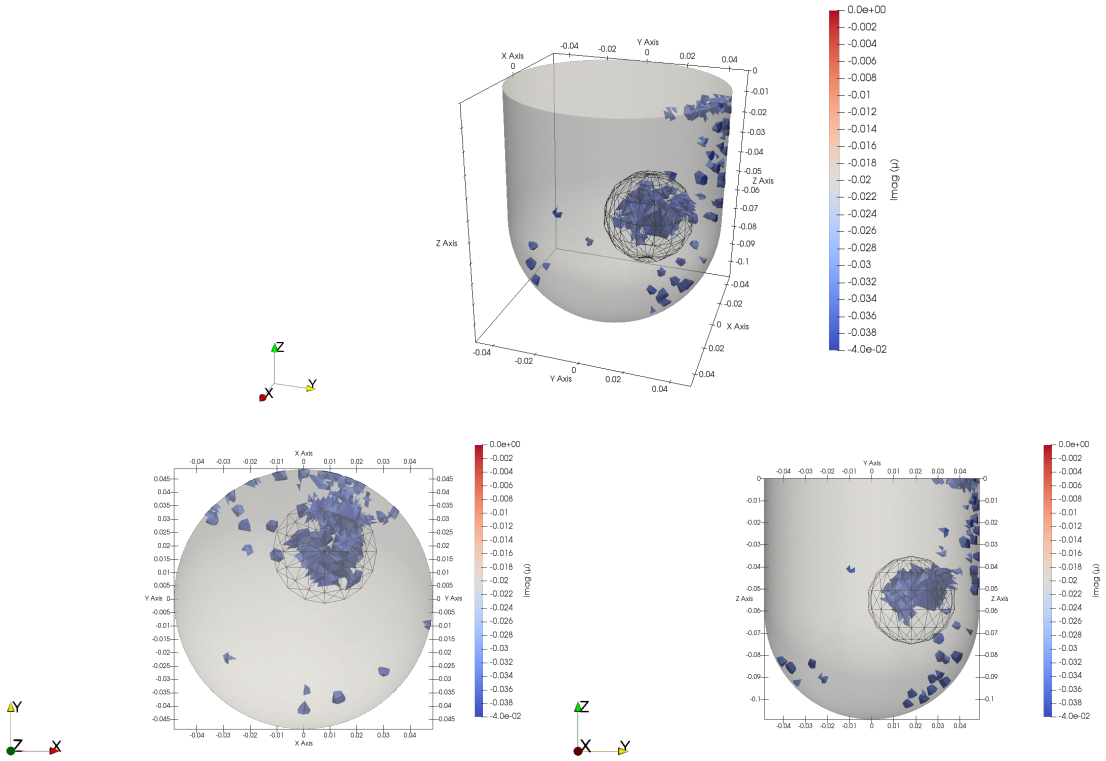

Figure B.7: Multiple views of 3D DGM-CSI inversion of Imag($\hat{\mu}_2$), using a reconstructed complex permittivity background subjected to a simple mapping technique.

the multifaceted approach to the enhancement of microwave images outlined in this thesis, particularly in the context of future experiments in 3D FRI.

References

[1] M. Lazebnik, D. Popovic, L. McCartney, C. B. Watkins, M. J. Lindstrom, J. Harter, S. Sewall, T. Ogilvie, A. Magliocco, T. M. Breslin, W. Temple, D. Mew, J. H. Booske, M. Okoniewski, and S. C. Hagness, "A large-scale study of the ultrawideband microwave dielectric properties of normal, benign and malignant breast tissues obtained from cancer surgeries." *Physics in medicine and biology*, vol. 52, no. 20, pp. 6093–6115, Oct. 2007.

[2] G. Bellizzi and O. M. Bucci, "A Novel Measurement Technique for the Broadband Characterization of Diluted Water Ferrofluids for Biomedical Applications," *IEEE Transactions on Magnetics*, vol. 49, no. 6, pp. 2903–2912, Jun. 2013.

[3] K. Nemez, A. Baran, M. Asefi, and J. LoVetri, "Modeling Error and Calibration Techniques for a Faceted Metallic Chamber for Magnetic Field Microwave Imaging," *IEEE Transactions on Microwave Theory and Techniques*, vol. 65, no. 11, pp. 4347–4356, Nov. 2017.

[4] K. Nemez, M. Asefi, A. Baran, and J. LoVetri, "A faceted magnetic field probe resonant chamber for 3D breast MWI: A synthetic study," in *2016 17th International Symposium on Antenna Technology and Applied Electromagnetics (ANTEM)*, Montreal, QC, Canada, Jul. 2016, pp. 322–324.

[5] J. H. Jacobi, L. E. Larsen, and C. T. Hast, "Water-Immersed Microwave Antennas and Their Application to Microwave Interrogation of Biological Targets," *IEEE Transactions on Microwave Theory and Techniques*, vol. 27, no. 1, pp. 70–78, Jan. 1979.

[6] P. Mojabi and J. LoVetri, "Enhancement of the Krylov Subspace Regularization for Microwave Biomedical Imaging," *IEEE Transactions on Medical Imaging*, vol. 28, no. 12, pp. 2015–2019, Dec. 2009.

[7] T. Rubaek, P. M. Meaney, P. Meincke, and K. D. Paulsen, "Nonlinear Microwave Imaging for Breast-Cancer Screening Using GaussNewton's Method and the CGLS Inversion Algorithm," *IEEE Transactions on Antennas and Propagation*, vol. 55, no. 8, pp. 2320–2331, Aug. 2007.

[8] Zhong Qing Zhang, Qing Huo Liu, Chunjiang Xiao, E. Ward, G. Ybarra, and W. T. Joines, "Microwave breast imaging: 3-D forward scattering simulation," *IEEE Transactions on Biomedical Engineering*, vol. 50, no. 10, pp. 1180–1189, Oct. 2003.

[9] Zhong Qing Zhang and Qing Huo Liu, "Three-dimensional nonlinear image reconstruction for microwave biomedical imaging," *IEEE Transactions on Biomedical Engineering*, vol. 51, no. 3, pp. 544–548, Mar. 2004.

[10] T. M. Grzegorczyk, P. M. Meaney, P. A. Kaufman, R. M. diFlorio-Alexander, and K. D. Paulsen, "Fast 3-D Tomographic Microwave Imaging for Breast Cancer Detection," *IEEE Transactions on Medical Imaging*, vol. 31, no. 8, pp. 1584–1592, Aug. 2012.

[11] N. K. Nikolova, "Microwave Imaging for Breast Cancer," *IEEE Microwave Magazine*, vol. 12, no. 7, pp. 78–94, Dec. 2011.

[12] D. Tajik, F. Foroutan, D. S. Shumakov, A. D. Pitcher, and N. K. Nikolova, "Real-Time Microwave Imaging of a Compressed Breast Phantom With Planar Scanning," *IEEE Journal of Electromagnetics, RF and Microwaves in Medicine and Biology*, vol. 2, no. 3, pp. 154–162, Sep. 2018.

[13] E. Porter, E. Kirshin, A. Santorelli, M. Coates, and M. Popovi, "Time-Domain Multistatic Radar System for Microwave Breast Screening," *IEEE Antennas and Wireless Propagation Letters*, vol. 12, pp. 229–232, 2013.

[14] E. Porter, M. Coates, and M. Popovi, "An Early Clinical Study of Time-Domain Microwave Radar for Breast Health Monitoring," *IEEE Transactions on Biomedical Engineering*, vol. 63, no. 3, pp. 530–539, Mar. 2016.

[15] E. C. Fear, S. C. Hagness, P. M. Meaney, M. Okoniewski, and M. A. Stuchly, "Enhancing breast tumor detection with near-field imaging," *IEEE Microwave Magazine*, vol. 3, no. 1, pp. 48–56, Mar. 2002.

[16] A. Diaz-Bolado and J. Laurin, "Experimental Validation of the Effect of Compression on Simplified Phantoms in Microwave Tomography Applied to Breast Cancer Detection," *IEEE Antennas and Wireless Propagation Letters*, vol. 11, pp. 1602–1605, 2012.

[17] P. Mojabi, N. Firoozy, N. Bayat, T. Brown, C. Narendra, P. Mojabi, C. Niu, T. Tiede, T. Neusitzer, X. Li, I. Jeffrey, J. LoVetri, and D. Barber, "Electromagnetic inversion for biomedical imaging, antenna characterization, and sea ice remote sensing applications," in *2016 URSI Asia-Pacific Radio Science Conference (URSI AP-RASC)*, Aug. 2016, pp. 586–589.

[18] P. M. Meaney, Qianqian Fang, C. A. Kogel, S. P. Poplack, P. A. Kaufman, and K. D. Paulsen, "Microwave imaging for neoadjuvant chemotherapy monitoring," in *2006 First European Conference on Antennas and Propagation*, Nov. 2006, pp. 1–4.

[19] T. F. Zanoon, M. S. Hathal, and M. Z. Abdullah, "Microwave imaging at resolution and super-resolution with ultra-wide band sensors," in *2012 IEEE International Conference on Imaging Systems and Techniques Proceedings*, Jul. 2012, pp. 538–543.

[20] C. Gilmore, P. Mojabi, A. Zakaria, S. Pistorius, and J. LoVetri, "On Super-Resolution With an Experimental Microwave Tomography System," *IEEE Antennas and Wireless Propagation Letters*, vol. 9, pp. 393–396, 2010.

[21] M. Lazebnik, L. McCartney, D. Popovic, C. B. Watkins, M. J. Lindstrom, J. Harter, S. Sewall, A. Magliocco, J. H. Booske, M. Okoniewski, and S. C. Hagness, "A large-scale study of the ultrawideband microwave dielectric properties of normal breast tissue obtained from reduction surgeries." *Physics in medicine and biology*, vol. 52, no. 10, pp. 2637–2656, May 2007.

[22] A. Trentham-Dietz, K. Kerlikowske, N. K. Stout, D. L. Miglioretti, C. B. Schechter, M. A. Ergun, J. J. van den Broek, O. Alagoz, B. L. Sprague, N. T. van Ravesteyn, A. M. Near, R. E. Gangnon, J. M. Hampton, Y. Chandler, H. J. de Koning, J. S. Mandelblatt, and A. N. A. Tosteson, "Tailoring Breast Cancer Screening Intervals by Breast Density and Risk for Women Aged 50 Years or Older: Collaborative Modeling of Screening Outcomes." *Annals of internal medicine*, vol. 165, no. 10, pp. 700–712, Nov. 2016.

[23] C. D'Orsi, E. Sickles, E. Mendelson, and E. Morris, *ACR BI-RADS Atlas, Breast Imaging Reporting and Data System*, 5th ed. Reston, VA: American College of Radiology, 2013.

[24] A. E. Burgess, "Visual Perception Studies and Observer Models in Medical Imaging," *Seminars in Nuclear Medicine*, vol. 41, no. 6, pp. 419 – 436, 2011. [Online]. Available: http://www.sciencedirect.com/science/article/pii/S0001299811000894

[25] A. E. Burgess, F. L. Jacobson, and P. F. Judy, "Human observer detection experiments with mammograms and power-law noise." *Medical physics*, vol. 28, no. 4, pp. 419–437, Apr. 2001.

[26] A. Mashal, J. H. Booske, and S. C. Hagness, "Toward contrast-enhanced microwave-induced thermoacoustic imaging of breast cancer: an experimental study of the effects of microbubbles on simple thermoacoustic targets." *Physics in medicine and biology*, vol. 54, no. 3, pp. 641–650, Feb. 2009.

[27] A. Mashal, B. Sitharaman, X. Li, P. K. Avti, A. V. Sahakian, J. H. Booske, and S. C. Hagness, "Toward Carbon-Nanotube-Based Theranostic Agents for Microwave Detection and Treatment of Breast Cancer: Enhanced Dielectric and Heating Response of Tissue-Mimicking Materials," *IEEE Transactions on Biomedical Engineering*, vol. 57, no. 8, pp. 1831–1834, Aug. 2010.

[28] G. Bellizzi, O. M. Bucci, and I. Catapano, "Microwave Cancer Imaging Exploiting Magnetic Nanoparticles as Contrast Agent," *IEEE Transactions on Biomedical Engineering*, vol. 58, no. 9, pp. 2528–2536, Sep. 2011.

[29] S. Semenov, N. Pham, and S. Egot-Lemaire, "Ferroelectric Nanoparticles for Contrast Enhancement Microwave Tomography: Feasibility Assessment for Detection of Lung Cancer," in *World Congress on Medical Physics and Biomedical Engineering, September 7 - 12, 2009, Munich, Germany*, O. Dssel and W. C. Schlegel, Eds. Berlin, Heidelberg: Springer Berlin Heidelberg, 2010, pp. 311–313.

[30] K. T. Lai, S. Semenov, A. M. Piras, F. Chiellini, C. Ravagli, and G. Baldi, "Optical and dielectric characterisations of magnetic nanoparticles in suspension," in *2011 41st European Microwave Conference*, Oct. 2011, pp. 953–955.

[31] K. Lai, B. Nair, and S. Semenov, "Optical and microwave studies of ferroelectric nanoparticles for application in biomedical imaging," *Microwave and Optical Technology Letters*, vol. 54, 2012.

[32] O. M. Bucci, G. Bellizzi, I. Catapano, L. Crocco, and R. Scapaticci, "MNP Enhanced Microwave Breast Cancer Imaging: Measurement Constraints and Achievable Performances," *IEEE Antennas and Wireless Propagation Letters*, vol. 11, pp. 1630–1633, 2012.

[33] R. Scapaticci, G. Bellizzi, I. Catapano, L. Crocco, and O. M. Bucci, "An Effective Procedure for MNP-Enhanced Breast Cancer Microwave Imaging," *IEEE Transactions on Biomedical Engineering*, vol. 61, no. 4, pp. 1071–1079, Apr. 2014.

[34] H. B. Na, I. C. Song, and T. Hyeon, "Inorganic Nanoparticles for MRI Contrast Agents," *Advanced Materials*, vol. 21, no. 21, pp. 2133–2148, 2009. [Online]. Available: https://onlinelibrary.wiley.com/doi/abs/10.1002/adma.200802366

[35] L. Josephson, C. H. Tung, A. Moore, and R. Weissleder, "High-efficiency intracellular magnetic labeling with novel superparamagnetic-Tat peptide conjugates." *Bioconjugate chemistry*, vol. 10, no. 2, pp. 186–191, Apr. 1999.

[36] Y. Zhang, N. Kohler, and M. Zhang, "Surface modification of superparamagnetic magnetite nanoparticles and their intracellular uptake." *Biomaterials*, vol. 23, no. 7, pp. 1553–1561, Apr. 2002.

[37] C. Kaye, I. Jeffrey, and J. LoVetri, "Two-stage reconstruction of complex dielectric permittivity and magnetic permeability for biomedical microwave imaging employing magnetic contrast agents," in *Proceedings of the 4th Advanced Electromagnetics Symposium (AES)*, Malaga, Spain, Jul. 2016, pp. 40–42.

[38] C. Kaye, K. Brown, M. Asefi, N. Geddert, I. Jeffrey, and J. LoVetri, "Experimental 3D Microwave Imaging of Magnetic Targets using Discontinuous Galerkin Contrast Source Inversion and a Two-Stage Reconstruction Technique," in *Proceedings of the 2nd URSI Atlantic Radio Science Conference (URSI AT-RASC)*, Gran Canaria, Spain, Jun. 2018.

[39] C. Kaye, I. Jeffrey, and J. LoVetri, "Enhancement of multi-frequency microwave breast images using a tissue-dependent mapping technique with discontinuous Galerkin contrast source inversion," in *Proceedings of the 4th Advanced Electromagnetics Symposium (AES)*, Malaga, Spain, Jul. 2016, pp. 37–39.

[40] C. Kaye, I. Jeffrey, and J. LoVetri, "Improvement of Multi-Frequency Microwave Breast Imaging through Frequency Cycling and Tissue-Dependent Mapping," *IEEE Transactions on Antennas and Propagation*, vol. 67, no. 11, pp. 7087–7096, Nov. 2019.

[41] C. Kaye, I. Jeffrey, and J. LoVetri, "Novel Stopping Criteria for Optimization-Based Microwave Breast Imaging Algorithms," *Journal of Imaging*, vol. 5, no. 5, p. 55, May 2019, publisher: MDPI AG. [Online]. Available: https://doi.org/10.3390%2Fjimaging5050055

[42] C. Kaye, C. Gilmore, and J. LoVetri, "Enhanced Detection of Magnetic Nanoparticles using a Novel Microwave Ferromagnetic Resonance Imaging System," *IEEE Transactions on Biomedical Engineering*, Aug. 2020, accepted for publication.

[43] P. M. Meaney, P. A. Kaufman, L. S. Muffly, M. Click, S. P. Poplack, W. A. Wells, G. N. Schwartz, R. M. di Florio-Alexander, T. D. Tosteson, Z. Li, S. D. Geimer, M. W. Fanning, T. Zhou, N. R. Epstein, and K. D. Paulsen, "Microwave imaging for neoadjuvant chemotherapy monitoring: initial clinical experience." *Breast cancer research : BCR*, vol. 15, no. 2, p. R35, Apr. 2013.

[44] H. G. Welch, P. C. Prorok, A. J. O'Malley, and B. S. Kramer, "Breast-Cancer Tumor Size, Overdiagnosis, and Mammography Screening Effectiveness." *The New England journal of medicine*, vol. 375, no. 15, pp. 1438–1447, Oct. 2016.

[45] A. Baran, D. Kurrant, A. Zakaria, E. Fear, and J. LoVetri, "Breast Imaging Using Microwave Tomography with Radar-Based Tissue-Regions Estimation," *Progress In Electromagnetics Research*, vol. 149, pp. 161–171, Jan. 2014.

[46] J. LoVetri, E. Fear, I. Jeffrey, M. Omer, P. Mojabi, D. Kurrant, and N. Abdollahi, "A multimodal ultrasound-microwave quantitative imaging technique for breast cancer," in *12th European Conference on Antennas and Propagation (EuCAP 2018)*, Apr. 2018, pp. 1–2.

[47] J. D. Shea, P. Kosmas, B. D. V. Veen, and S. C. Hagness, "Contrast-enhanced microwave imaging of breast tumors: a computational study using 3D realistic numerical phantoms," *Inverse Problems*, vol. 26, no. 7, p. 074009, Jun. 2010. [Online]. Available: https://doi.org/10.1088%2F0266-5611%2F26%2F7%2F074009

[48] A. Zakaria, I. Jeffrey, and J. LoVetri, "Full-Vectorial Parallel Finite-Element Contrast Source Inversion Method," *Progress In Electromagnetics Research*, vol. 142, pp. 463–483, Jan. 2013.

[49] R. F. Bloemenkamp, A. Abubakar, and P. M. v. d. Berg, "Inversion of experimental multi-frequency data using the contrast source inversion method," *Inverse Problems*, vol. 17, no. 6, pp. 1611–1622, Nov. 2001. [Online]. Available: http://dx.doi.org/10.1088/0266-5611/17/6/305

[50] O. M. Bucci, L. Crocco, T. Isernia, and V. Pascazio, "Inverse scattering problems with multifrequency data: reconstruction capabilities and solution strategies," *IEEE Transactions on Geoscience and Remote Sensing*, vol. 38, no. 4, pp. 1749–1756, Jul. 2000.

[51] R. Obermeier and J. A. Martinez-Lorenzo, "Compressive sensing unmixing algorithm for breast cancer detection," *IET Microwaves, Antennas & Propagation*, vol. 12, no. 4, pp. 533–541, 2018.

[52] W. C. Chew and J. H. Lin, "A frequency-hopping approach for microwave imaging of large inhomogeneous bodies," *IEEE Microwave and Guided Wave Letters*, vol. 5, no. 12, pp. 439–441, Dec. 1995.

[53] R. Ferraye, J. -Y. Dauvignac, and C. Pichot, "An inverse scattering method based on contour deformations by means of a level set method using frequency hopping technique," *IEEE Transactions on Antennas and Propagation*, vol. 51, no. 5, pp. 1100–1113, May 2003.

[54] Z. Miao and P. Kosmas, "Multiple-Frequency DBIM-TwIST Algorithm for Microwave Breast Imaging," *IEEE Transactions on Antennas and Propagation*, vol. 65, no. 5, pp. 2507–2516, May 2017.

[55] R. Scapaticci, P. Kosmas, and L. Crocco, "Wavelet-Based Regularization for Robust Microwave Imaging in Medical Applications," *IEEE Transactions on Biomedical Engineering*, vol. 62, no. 4, pp. 1195–1202, Apr. 2015.

[56] F. Gao, B. D. Van Veen, and S. C. Hagness, "Sensitivity of the Distorted Born Iterative Method to the Initial Guess in Microwave Breast Imaging," *IEEE Transactions on Antennas and Propagation*, vol. 63, no. 8, pp. 3540–3547, Aug. 2015.

[57] I. Jeffrey, A. Zakaria, and J. LoVetri, "Microwave imaging by mixed-order discontinuous Galerkin contrast source inversion," in *2014 XXXIth URSI General Assembly and Scientific Symposium (URSI GASS)*, Aug. 2014, pp. 1–4.

[58] I. Jeffrey, N. Geddert, K. Brown, and J. LoVetri, "The time-harmonic Discontinuous Galerkin Method as a robust forward solver for microwave imaging applications," *Progress In Electromagnetics Research*, vol. 154, pp. 1–21, Jan. 2015.

[59] K. G. Brown, N. Geddert, M. Asefi, J. LoVetri, and I. Jeffrey, "Hybridizable Discontinuous Galerkin Method Contrast Source Inversion of 2-D and 3-D Dielectric and Magnetic Targets," *IEEE Transactions on Microwave Theory and Techniques*, vol. 67, no. 5, pp. 1766–1777, May 2019.

[60] P. M. Meaney, N. K. Yagnamurthy, and K. D. Paulsen, "Pre-scaled two-parameter GaussNewton image reconstruction to reduce property recovery imbalance," *Physics in Medicine and Biology*, vol. 47, no. 7, pp. 1101–1119, Mar. 2002. [Online]. Available: http://dx.doi.org/10.1088/0031-9155/47/7/308

[61] P. Mojabi and J. LoVetri, "Evaluation of Balanced Ultrasound Breast Imaging Under Three Density Profile Assumptions," *IEEE Transactions on Computational Imaging*, vol. 3, no. 4, pp. 864–875, Dec. 2017.

[62] A. Zakaria, "The Finite-Element Contrast Source Inversion Method for Microwave Imaging Applications," Ph.D. thesis, University of Manitoba, Winnipeg, MB, Canada, 2012.

[63] P. Mojabi and J. LoVetri, "A Prescaled Multiplicative Regularized Gauss-Newton Inversion," *IEEE Transactions on Antennas and Propagation*, vol. 59, no. 8, pp. 2954–2963, Aug. 2011.

[64] S. Gabriel, R. W. Lau, and C. Gabriel, "The dielectric properties of biological tissues: III. Parametric models for the dielectric spectrum of tissues," *Physics in Medicine and Biology*, vol. 41, no. 11, pp. 2271–2293, Nov. 1996. [Online]. Available: http://dx.doi.org/10.1088/0031-9155/41/11/003

[65] J. D. Shea, P. Kosmas, S. C. Hagness, and B. D. Van Veen, "Three-dimensional microwave imaging of realistic numerical breast phantoms via a multiple-frequency inverse scattering technique." *Medical physics*, vol. 37, no. 8, pp. 4210–4226, Aug. 2010.

[66] M. Ambrosanio, P. Kosmas, and V. Pascazio, "A Multithreshold Iterative DBIM-Based Algorithm for the Imaging of Heterogeneous Breast Tissues," *IEEE Transactions on Biomedical Engineering*, vol. 66, no. 2, pp. 509–520, Feb. 2019.

[67] A. Zakaria, C. Gilmore, and J. LoVetri, "Finite-element contrast source inversion method for microwave imaging," *Inverse Problems*, vol. 26, no. 11, p. 115010, Sep. 2010. [Online]. Available: https://doi.org/10.1088%2F0266-5611%2F26%2F11%2F115010

[68] D. Kurrant and E. Fear, "Regional estimation of the dielectric properties of inhomogeneous objects using near-field reflection data," *Inverse Problems*, vol. 28, no. 7, p. 075001, Jun. 2012. [Online]. Available: http://dx.doi.org/10.1088/0266-5611/28/7/075001

[69] M. Asefi, G. Faucher, and J. LoVetri, "Surface-Current Measurements as Data for Electromagnetic Imaging Within Metallic Enclosures," *IEEE Transactions on Microwave Theory and Techniques*, vol. 64, no. 11, pp. 4039–4047, Nov. 2016.

[70] M. Asefi, A. Zakaria, and J. LoVetri, "Microwave Imaging Using Normal Electric-Field Components Inside Metallic Resonant Chambers," *IEEE Transactions on Microwave Theory and Techniques*, vol. 65, no. 3, pp. 923–933, Mar. 2017.

[71] W.-M. Boerner, H. Brand, L. A. Cram, D. T. Gjessing, A. K. Jordan, W. Keydel, G. Schwierz, and M. Vogel, Eds., *Inverse Methods in Electromagnetic Imaging*. Dordrecht, The Netherlands: D. Reidel Publishing, 1985.

[72] J. H. Jacobi and L. E. Larsen, Eds., *Medical Applications of Microwave Imaging*. New York, NY, USA: IEEE Press, 1986.

[73] P. Kosmas and L. Crocco, "Introduction to Special Issue on Electromagnetic Technologies for Medical Diagnostics: Fundamental Issues, Clinical Applications and Perspectives," *Diagnostics*, vol. 9, no. 1, 2019.

[74] J. M. Sill and E. C. Fear, "Tissue Sensing Adaptive Radar for Breast Cancer DetectionExperimental Investigation of Simple Tumor Models," *IEEE Transactions on Microwave Theory and Techniques*, vol. 53, no. 11, pp. 3312–3319, Nov. 2005.

[75] F. Delbary, M. Brignone, G. Bozza, R. Aramini, and M. Piana, "A Visualization Method for Breast Cancer Detection Using Microwaves," *SIAM Journal on Applied Mathematics*, vol. 70, no. 7, pp. 2509–2533, Jan. 2010. [Online]. Available: https://doi.org/10.1137/090774720

[76] F. Cakoni, D. Colton, and P. Monk, "Qualitative Methods in Inverse Electromagnetic Scattering Theory: Inverse Scattering for Anisotropic Media." *IEEE Antennas and Propagation Magazine*, vol. 59, no. 5, pp. 24–33, Oct. 2017.

[77] D. Colton and R. Kress, *Inverse acoustic and electromagnetic scattering theory*. Berlin, Germany: Springer Science & Business Media, 2012, vol. 93.

[78] H. W. Engl, M. Hanke, and A. Neubauer, *Regularization of Inverse Problems*. Dordrecht, Netherlands: Kluwer Academic Publishers, 1996.

[79] P. M. v. d. Berg and R. E. Kleinman, "A contrast source inversion method," *Inverse Problems*, vol. 13, no. 6, pp. 1607–1620, Dec. 1997. [Online]. Available: http://dx.doi.org/10.1088/0266-5611/13/6/013

[80] A. Abubakar, P. M. van den Berg, and J. J. Mallorqui, "Imaging of biomedical data using a multiplicative regularized contrast source inversion method," *IEEE Transactions on Microwave Theory and Techniques*, vol. 50, no. 7, pp. 1761–1771, Jul. 2002.

[81] D. Kurrant, A. Baran, J. LoVetri, and E. Fear, "Integrating prior information into microwave tomography Part 1: Impact of detail on image quality." *Medical physics*, vol. 44, no. 12, pp. 6461–6481, Dec. 2017.

[82] D. Kurrant, E. Fear, A. Baran, and J. LoVetri, "Integrating prior information into microwave tomography part 2: Impact of errors in prior information on microwave tomography image quality." *Medical physics*, vol. 44, no. 12, pp. 6482–6503, Dec. 2017.

[83] N. Abdollahi, D. Kurrant, P. Mojabi, M. Omer, E. Fear, and J. LoVetri, "Incorporation of Ultrasonic Prior Information for Improving Quantitative Microwave Imaging of Breast," *IEEE Journal on Multiscale and Multiphysics Computational Techniques*, vol. 4, pp. 98–110, 2019.

[84] M. Asefi, A. Baran, and J. LoVetri, "An Experimental Phantom Study for Air-Based Quasi-Resonant Microwave Breast Imaging," *IEEE Transactions on Microwave Theory and Techniques*, vol. 67, no. 9, pp. 3946–3954, Sep. 2019.

[85] P. M. v. d. Berg, A. L. v. Broekhoven, and A. Abubakar, "Extended contrast source inversion," *Inverse Problems*, vol. 15, no. 5, pp. 1325–1344, Oct. 1999. [Online]. Available: http://dx.doi.org/10.1088/0266-5611/15/5/315

[86] A. Abubakar, P. M. v. d. Berg, and T. M. Habashy, "Application of the multiplicative regularized contrast source inversion method on TM- and TE-polarized experimental Fresnel data," *Inverse Problems*, vol. 21, no. 6, pp. S5–S13, Nov. 2005. [Online]. Available: http://dx.doi.org/10.1088/0266-5611/21/6/S02

[87] C. Kaye, "Development and Calibration of Microwave Tomography Imaging Systems for Biomedical Applications Using Computational Electromagnetics," Master's thesis, University of Manitoba, Winnipeg, MB, Canada, 2009.

[88] F. J. Massey, "The Kolmogorov-Smirnov Test for Goodness of Fit," *Journal of the American Statistical Association*, vol. 46, no. 253, pp. 68–78, 1951. [Online]. Available: www.jstor.org/stable/2280095

[89] L. H. Miller, "Table of Percentage Points of Kolmogorov Statistics," *Journal of the American Statistical Association*, vol. 51, no. 273, pp. 111–121, 1956. [Online]. Available: www.jstor.org/stable/2280807

[90] G. Marsaglia, W. W. Tsang, and J. Wang, "Evaluating Kolmogorov's Distribution," *Journal of Statistical Software, Articles*, vol. 8, no. 18, pp. 1–4, 2003. [Online]. Available: https://www.jstatsoft.org/v008/i18

[91] MathWorks, "Two-Sample Kolmogorov-Smirnov Test (R2018a)." [Online]. Available: www.mathworks.com/help/stats/kstest2.html

[92] A. Abubakar and P. M. van den Berg, "Iterative forward and inverse algorithms based on domain integral equations for three-dimensional electric and magnetic objects," *Journal of Computational Physics*, vol. 195, no. 1, pp. 236–262, Mar. 2004. [Online]. Available: http://www.sciencedirect.com/science/article/pii/S002199910300531X

[93] G. Bellizzi and O. M. Bucci, "Blind Focusing of Electromagnetic Fields in Hyperthermia Exploiting Target Contrast Variations," *IEEE Transactions on Biomedical Engineering*, vol. 62, no. 1, pp. 208–217, Jan. 2015.

[94] G. Bellizzi, O. M. Bucci, and G. Chirico, "Criterion for the optimal choice of the treatment conditions in magnetic nanoparticle hyperthermia: Assessment in 3D realistic numerical head model," in *2015 9th European Conference on Antennas and Propagation (EuCAP)*, Apr. 2015, pp. 1–4.

[95] O. M. Bucci, G. Bellizzi, S. Costanzo, L. Crocco, G. Di Massa, and R. Scapaticci, "Assessing Detection Limits in Magnetic Nanoparticle Enhanced Microwave Imaging," *IEEE Access*, vol. 6, pp. 43 192–43 202, 2018.

[96] G. Bellizzi, O. M. Bucci, I. Catapano, L. Crocco, and R. Scapaticci, "Magnetic nanoparticles enhanced microwave imaging: A feasibility assessment," in *2012 6th European Conference on Antennas and Propagation (EUCAP)*, Mar. 2012, pp. 177–180.

[97] J. H. E. Griffiths, "Anomalous High-frequency Resistance of Ferromagnetic Metals," *Nature*, vol. 158, no. 4019, pp. 670–671, Nov. 1946. [Online]. Available: https://doi.org/10.1038/158670a0

[98] C. Kittel, "On the Theory of Ferromagnetic Resonance Absorption," *Physical Review*, vol. 73, no. 2, pp. 155–161, Jan. 1948. [Online]. Available: https://link.aps.org/doi/10.1103/PhysRev.73.155

[99] H. Suhl, "Ferromagnetic Resonance in Nickel Ferrite Between One and Two Kilomegacycles," *Physical Review*, vol. 97, no. 2, pp. 555–557, Jan. 1955. [Online]. Available: https://link.aps.org/doi/10.1103/PhysRev.97.555.2

[100] P. Fannin, "Characterisation of magnetic fluids," *Proceedings of the VI Latin American Workshop on Magnetism, Magnetic Materials and their Applications*, vol. 369, no. 1, pp. 43–51, Apr. 2004. [Online]. Available: http://www.sciencedirect.com/science/article/pii/S0925838803009666

[101] P. Fannin, "Use of ferromagnetic resonance measurements in magnetic fluids," *Diffusion and Relaxation in Disordered Fractal Systems. Proceedings from the meeting on Diffusion and Relaxation in Disordered Fractal Systems*, vol. 114, no. 1, pp. 79–87, Sep. 2004. [Online]. Available: http://www.sciencedirect.com/science/article/pii/S0167732204000224

[102] L. D. Landau and E. Lifshitz, "On the theory of the dispersion of magnetic permeability in ferromagnetic bodies," *Phys. Z. Sowjet.*, vol. 8, pp. 153–169, 1935. [Online]. Available: http://cds.cern.ch/record/437299

[103] P. C. Fannin, B. K. P. Scaife, A. T. Giannitsis, and S. W. Charles, "Determination of the radius of nano-particles in a magnetic fluid by means of a constant frequency measurement technique," *Journal of Physics D: Applied Physics*, vol. 35, no. 12, pp. 1305–1310, Jun. 2002. [Online]. Available: http://dx.doi.org/10.1088/0022-3727/35/12/304

[104] A. M. Nicolson and G. F. Ross, "Measurement of the Intrinsic Properties of Materials by Time-Domain Techniques," *IEEE Transactions on Instrumentation and Measurement*, vol. 19, no. 4, pp. 377–382, Nov. 1970.

[105] S. Wilhelm, A. J. Tavares, Q. Dai, S. Ohta, J. Audet, H. F. Dvorak, and W. C. W. Chan, "Analysis of nanoparticle delivery to tumours," *Nature Reviews Materials*, vol. 1, no. 5, p. 16014, Apr. 2016. [Online]. Available: https://doi.org/10.1038/natrevmats.2016.14

[106] O. M. Bucci, G. Bellizzi, A. Borgia, S. Costanzo, L. Crocco, G. Di Massa, and R. Scapaticci, "Experimental Framework for Magnetic Nanoparticles Enhanced Breast Cancer Microwave Imaging," *IEEE Access*, vol. 5, pp. 16 332–16 340, 2017.

[107] R. F. Harrington, *Time-Harmonic Electromagnetic Fields*. New York, NY, USA: IEEE Press, 2001.

[108] C. Gilmore, P. Mojabi, A. Zakaria, M. Ostadrahimi, C. Kaye, S. Noghanian, L. Shafai, S. Pistorius, and J. LoVetri, "A Wideband Microwave Tomography System With a Novel Frequency Selection Procedure," *IEEE Transactions on Biomedical Engineering*, vol. 57, no. 4, pp. 894–904, Apr. 2010.

[109] O. M. Bucci, G. Bellizzi, S. Costanzo, L. Crocco, G. D. Massa, and R. Scapaticci, "Preliminary Assessment of the Origin of Spurious Magnetic Effects in Magnetic Nanoparticle Enhanced Microwave Imaging," in *2019 13th European Conference on Antennas and Propagation (EuCAP)*, Apr. 2019, pp. 1–3.

[110] K. Brown, N. Geddert, G. Faucher, A. Baran, M. Asefi, K. Nemez, J. LoVetri, and I. Jeffrey, "3D Microwave Imaging using the Time-Harmonic Discontinuous Galerkin Method - Contrast Source Inversion," in *2017 IEEE AP-S Symposium on Antennas and Propagation and USNC-URSI Radio Science Meeting*, San Diego, California, USA, Jul. 2017.